AN IMPLICIT FINITE DIFFERENCE PROCEDURE FOR THE LAMINAR, SUPERSONIC BASE FLOW

A THESIS

Presented to

The Faculty of the Division of Graduate

Studies and Research

By

Robert Landon Roach

In Partial Fulfillment

of the Requirements for the Degree

Doctor of Philosophy

in the School of Aerospace Engineering

Georgia Institute of Technology

December 1977

AN IMPLICIT FINITE DIFFERENCE PROCEDURE FOR THE

LAMINAR, SUPERSONIC BASE FLOW

Approved:

Dr. Louis H. Bangert, Chairman

Dr. Warren C. Strahle

Dr. James Wu

ACKNOWLEDGMENTS

It gives me great pleasure to express my deep gratitude to Dr. Louis H. Bangert for his suggestion of the thesis topic, his thoughtful guidance throughout the course of the investigation, and his constant willingness to discuss all manner of topics, even those having to do with this problem. Many thanks too to his ever thoughtful family for their moral support and prayers.

I wish to thank Dr. Strahle and Dr. Wu for their careful review and useful suggestions and the other members of the committee. Dr. Sam Martin and Dr. Stephen Demko, for their patient examination of the thesis.

I wish to thank my fellow graduate students for providing friendship and hours of enlightening discussions, especially Frank, Pad, Kottapalli, Amir, and Sankar.

My appreciation goes to Peggy Weldon for an excellent and competent job done typing the thesis.

I also wish to express a deep gratitude to the people of St. Patrick's Episcopal Church for their prayerful concern, fellowship, and love, especially the Reverend Gray Temple for all his loving instruction, and my parents for their constant encouragement throughout my life.

My deepest and sincerest love goes to my wife, Gloria, whose unwavering faith in me is a continual inspiration.

Finally, I give humble thanks to almighty God, Who ultimately gives meaning to all things, including our puny efforts to approximate His perfection.

TABLE OF CONTENTS

TABLE OF CONTENTS (Continued)

LIST OF TABLES

LIST OF FIGURES

LIST OF FIGURES (Continued)

LIST OF SYMBOLS

$\overline{\overline{a}}_i$	coeff. matrix for ϕ^*_{i+1j} for i^{th} grid point in j^{th} row
$\overline{\overline{b}}_i$	coeff. matrix for ϕ^*_{ij} for i^{th} grid point in j^{th} row
$\overline{\overline{c}}_i$	coeff. matrix for $\phi^*_{i-1,j}$ for i^{th} grid point in j^{th} row
c_p	specific heat at constant pressure
c_v	specific heat at constant volume
$\overline{d}_i$	column vector of terms for RHS of x-sweep equations
e	mean interval energy per unit mass, made nondimensional by e_1
H	base half height
k	coefficient of heat conductivity
K	$\gamma(\gamma-1)\mu_1^2$
L	lower triangular matrix
M_1	Mach number, $u_1/[\gamma(\gamma-1)e_1]^{1/2}$
p	mean static pressure, made nondimensional by p_1
Pr	Prandtl number, $\mu_1 c_p/k_1$
q_i	heat flux vector, $-\partial e/\partial x_i$
Re	Reynolds number, $\rho_1 u_1 H/\ _1$
S_{ij}	see Appendix A
t	time, made nondimensional by H/u_1
T	total elapsed nondimensional time, i.e (Number of time steps, x(Δt)
u,v	mean velocity and x- and y-direction, respectively, made nondimensional by u_1
U	upper triangular matrix

x,y,z	Cartesian coordinates, made nondimensional by H
x+,x-	right and left edges, respectively, of cell containing grid point ij
y+,y-	upper and lower edges, respectively, of cell containing grid point ij

Greek Symbols

$\overline{\overline{\alpha}}_j$	coeff matrix for ϕ^{**}_{ij+1} for j^{th} grid point in i^{th} column
$\overline{\overline{\beta}}_j$	coeff matrix for ϕ^{**}_{ij} for j^{th} grid point in i^{th} column
$\overline{\overline{\gamma}}_j$	coeff matrix for ϕ^{**}_{ij-1} for j^{th} grid point in i^{th} column
γ	ratio of specific heats
Δt	computational time step, made nondimensional by H/u_1
$\Delta x, \Delta y$	dimensions of cell containing point ij, made nondimensional by H
δx	$(\delta x\phi)_{ij} = \frac{1}{\Delta x}(\phi_{x+} - \phi_{x-})$
δy	$(\delta y\phi)_{ij} = \frac{1}{\Delta y}(\phi_{y+} - \phi_{y-})$
$\overline{\eta}_j$	RHS column vector containing n^{th} time level terms
ϕ	any dependent variable
θ	local flow angle, arctan (v/u)
μ	molecular viscosity, nondimensionalized by μ_1
μ_M	local flow Mach angle, arcsin $(1/M_1)$
ν	kinematic viscosity, nondimensionalized by μ_1/ρ_1
$\overline{\xi}_j$	RHS column vector containing * time level quantities
ρ	mean density, nondimensionalized by ρ_1
τ_{ij}	component of stress tensor

Subscripts

1	denotes free stream conditions
ij	coordinate location, i^{th} column, j^{th} row

Superscripts

n	known time level
n+1	unknown time level
=	denotes a two-dimensional matrix
-	denotes a column or one-dimensional matrix
*	intermediate time level after x-sweep
**	time level after y-sweep, taken to be the same as (n+1)

SUMMARY

The development of a tool for solving the near field of a scramjet fuel injector was attacked by first developing a numerical technique for solving the laminar, supersonic near wake flow. It was considered important to develop a procedure that had a potential for reduced computation time compared with explicit methods. The implicit numerical procedure of Briley and McDonald was extended to mixed subsonic/supersonic flow with shocks, expansions, and regions of reverse flow. Briley and McDonald had previously applied the procedure to subsonic, constant area duct flow with no recirculation. In the present case, numerical results have been obtained for the laminar, supersonic near wake behind a rectangular base.

The numerical method applies a time linearization based on a Taylor series expansion about the known time level, and the Douglas-Gunn alternating Direction Implicit (ADI) procedure to the Navier-Stokes equations. Briley and McDonald obtained the finite difference equations by using standard three-point central differencing. This generated a series of block tridiagonal systems which can be quickly solved by a standard elimination technique. The same approach was followed here, except that all of the differential equations were written in the conservation form (Briley and McDonald used the non-conservation form of the energy equation) and the finite difference equations were derived by the cell integration technique. The cell integration technique considers

the conservation equations as integral laws over a control volume (cell) around a grid point and also leads to central differencing for the interior grid points.

The chief advantage in using the cell integration technique is the conceptual aid afforded in applying the boundary conditions. Allen and Cheng used this technique, and their work served as a guide in selecting one-sided difference forms for the nonzero boundary terms. Because the present method is implicit, however, several new forms were required for stable and accurate solutions. It was found, for example, that second-order forms for the pressure and $\partial v/\partial y$ on the centerline are needed to prevent y-direction wiggles in the steady state solution. Also, a new implicit, linear extrapolation scheme using the finite difference equations was developed for the outflow boundary. This was required to eliminate wiggles in the x-direction in the steady-state solution. All the explicit extrapolation schemes at the outflow caused the solution to diverge for $\Delta t > \Delta t_{CFL}$. Zero-gradient forms at the outflow boundary, whether explicit or implicit, caused x-direction wiggles in the steady state solution.

Three-dimensional contour plots proved to be an important diagnostic tool. It was not discovered that the x-direction wiggles were caused by the treatment of the outflow boundary conditions until the 3-D plots clearly revealed that as the recompression wave crossed the downstream boundary, the wiggles formed and propagated upstream to the back wall and inflow regions. Up to then, the suspected causes were improper treatment of the back wall boundary conditions, or that the cell Reynolds numbers were greater than two there. The use of upwind

differencing, artificial viscosity, or a much smaller Δx were considered to be undesirable remedies.

The results for the contour plots showed qualitative agreement with Allen and Cheng and Kronzon, et al., and close quantitative agreement where comparisons were possible. The centerline pressure plot showed very close quantitative agreement with Allen and Cheng. As a further check on accuracy, overall mass balances were computed at each time step. In the (nearly) steady state conditions, net mass inflow rate differed from net mass outflow rate by about 1.8% or less.

No artificial viscosity was used in obtaining these solutions. It is interesting that Briley and McDonald required an additional explicit artificial viscosity in their subsonic duct flow solutions. The reasons for this difference in behavior are not known. It may be speculated, however, that the difference arises from the present use of the conservative form of the conservation equations, the cell integration technique for generating finite-difference equations, and the corresponding careful treatment of the boundary conditions.

A time step limitation was expected, although the method is implicit, because the equations were linearized with respect to time. For one set of initial conditions, this limitation was found to be around 32 Δt_{CFL}. The present method had a computation time per time step per grid point of approximately five times longer than Allen's explicit method, but could take time steps over 30 times larger. This represents a six-fold decrease in computation time. In addition, the ability to change (increase) the size of the time step during computation to reduce

computation time was demonstrated. This suggests that a time step strategy might be successful wherein smaller Δt's were used at the beginning, followed by increasing Δt as the steady state is approached. This would be appropriate when the assumed initial conditions were very far from the steady-state solution. Thus the method appears to offer significant time savings.

The effect of initial conditions on the steady-state solution was examined. To do this, a range of initial horizontal velocities were applied in the region below the expansion corner. All the other initial conditions were the same: a boundary layer on the upper wall upstream of the expansion corner and freestream conditions elsewhere. It was shown that $u = 0$ led to divergence for $\Delta t = 16\Delta t_{CFL}$. Increasingly rapid rates of convergence were realized as u was increased from 10% to 100% of the freestream value. The results for all the converged cases indicated that the final solution was insensitive to the initial conditions, but that the time to convergence was highly dependent on initial conditions. Also, convergence was shown to occur for a significant range of initial backwall u.

Accuracy of the coarse mesh results was shown by comparisons with the fine mesh solution. Both solutions were in close agreement. Small, irregular disturbances in the inflow region and in the shock occurred for the coarse mesh solution. These can be attributed to the lack of resolution in the coarse mesh in the inflow boundary layer and in the shock at the outflow, as they disappeared in the fine mesh solution.

These numerical results served to demonstrate that this numerical method produced stable, convergent, and accurate solutions when applied to this complex flow problem. To the author's knowledge, no other implicit scheme has been successfully applied to the multidimensional nonlinear Navier-Stokes equations for the supersonic base flow problem.

CHAPTER I

INTRODUCTION

Recent interest in hypersonic flight has motivated an increasing number of investigations into advanced airbreathing propulsion devices, including supersonic-combustion ramjets (or scramjets). Many studies have been related to an airbreathing launch vehicle for NASA's space shuttles, but found that the technological state-of-the-art of the propulsion system was not sufficiently developed.[1-3] More recently attention has been given to developing a scramjet engine for a hypersonic research vehicle.[4] A principle requirement of the scramjet is the specification of the flow field downstream of the fuel injector. Knowledge of the combustion flow field and heat release distributions, for example, would allow for the design of engines requiring a fraction of the fuel heat sink capacity for cooling. This would allow the airframe designer more flexibility. Additionally, there is the need for complete combustion in as short a distance as possible, so that long combustors will not be required. Hence the need for rapid mixing of the fuel and air streams makes the near field of the injector a region of great interest.

The injector flow field is quite complex, which greatly hinders analysis (see Figure 1). Shocks, high transverse pressure gradients, and region of reverse flow make the near field similar to a base flow, but with the added complications of fuel injection and subsequent mixing and combustion. All of the flow features strongly influence the turbulent mixing and combustion.[5-9] Hence an accurate analytical procedure

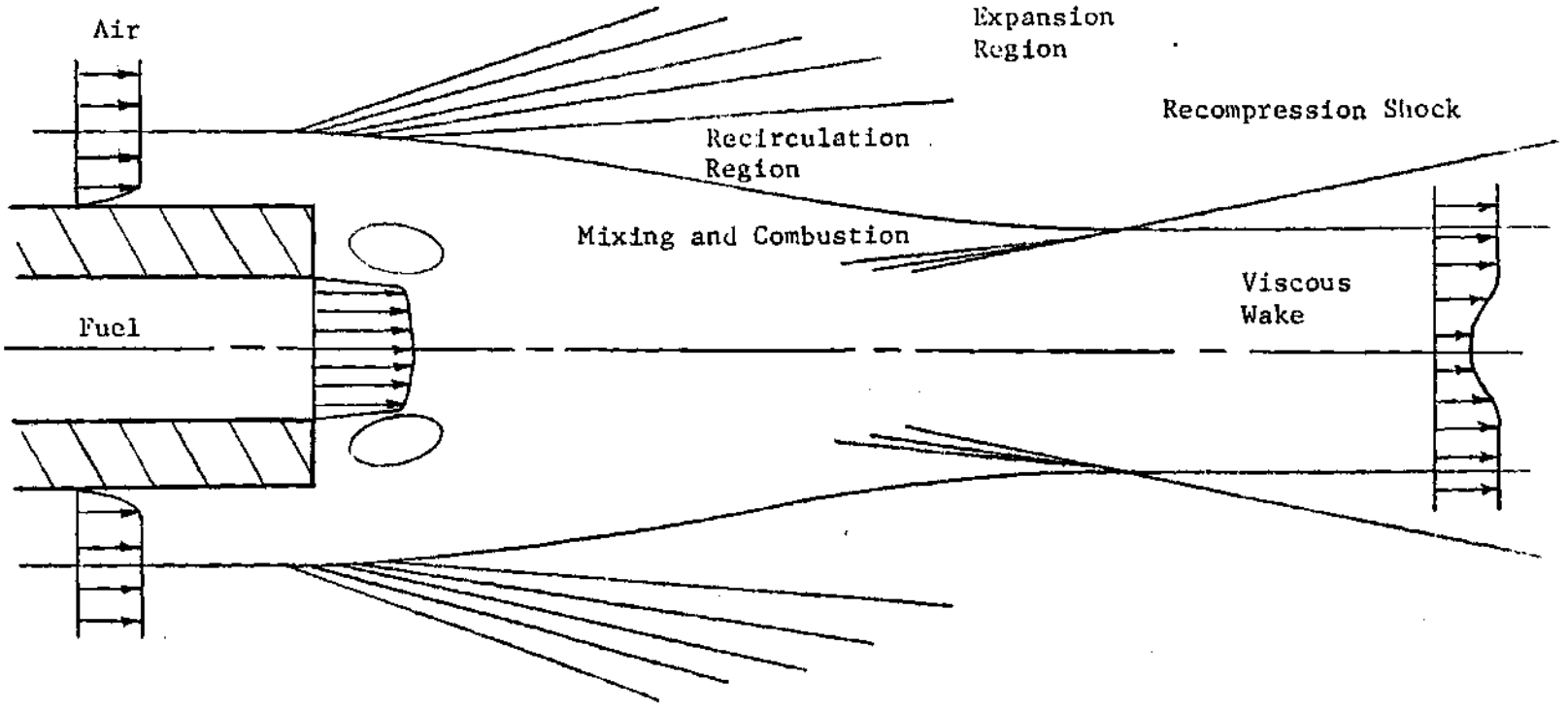

Figure 1. General Fuel Injector Flow Field.

which describes the fuel injector near field must include all these features. Previous studies[10-15] examined the mixing and combustion of compressible turbulent streams but neglected, and indeed could not compute, the important effects of shocks, recirculation, and regions of high transverse pressure gradients.

The present analysis seeks to include these effects, but neglects the turbulence and combustion for two reasons. Uncertainties in the turbulence and combustion models limit the validity of analysis. Even relatively advanced turbulence models, such as those where velocity and length scales are computed from differential equations,[16-19] may have difficulty in describing details of this flow. Thus, it would be difficult to establish whether inaccuracies in a new numerical procedure were due to the models or to the method itself. Second, experience has shown the differential equations of turbulence to be troublesome numerically, which greatly hinders even the development of a new method.[20] It is therefore prudent to prove a new method first by solving a similar problem where the flow is well-characterized by the governing equations. Here, the laminar, supersonic base flow problem (Figure 2) was solved. The flow is specified by the Navier-Stokes equations along with the conservation equations of mass and energy and the equation of state.

Many previous base flow studies used an integral technique to determine a base pressure or a base drag, but few other details of the flow. Mueller,[21] for example, used the Chapman-Korst method to determine a single turbulent base pressure for supersonic axisymmetric flow, which was assumed to be constant across the base. Mueller pointed out that

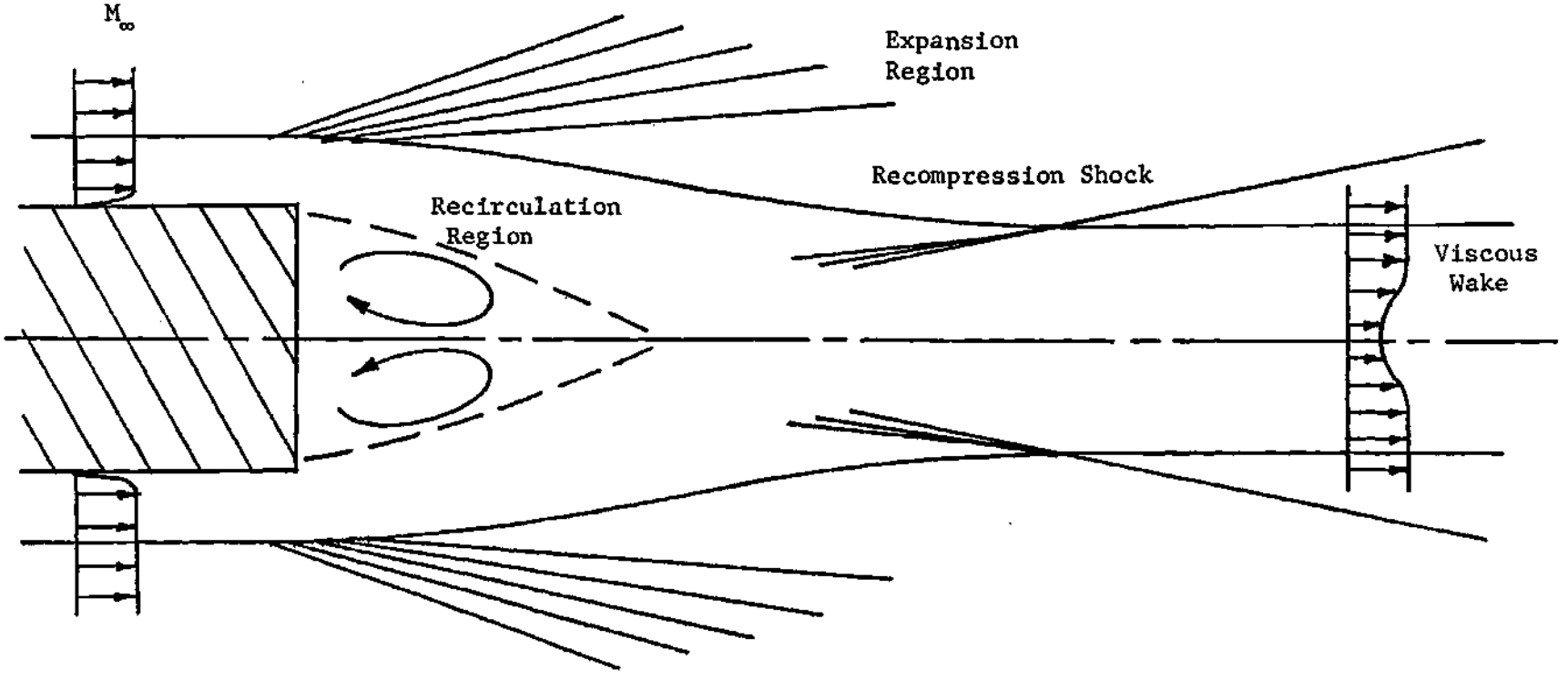

Figure 2. No Injection Flow Field (Base Flow)

the solutions obtained were asymptotic and valid only for high Reynolds numbers, and that the important effects of the initial boundary layer were neglected. Alber and Lees,[22] used the Crocco-Lees integral procedure for supersonic turbulent base flows. They showed that the initial boundary layer can dominate the viscous interaction near the base when its height is of the order of the base height. They also computed a constant pressure up to the rear stagnation point, the distance to the rear stagnation point, the centerline pressure distribution downstream of this point, and the correct trend of increasing average base pressure for increasing initial boundary layer thickness. Both integral theories rely heavily on the flow being well-characterized beforehand by another method or by experimental data. Neither have been shown to compute details within the recirculation region, variation of pressure within the recirculation region and along the base, and shocks. Extension of an integral technique to include these features and subsequent extension to the case of a fuel injector appears to be unpromising at best. Even extension of the Crocco-Lees method, for example, to axisymmetric flow has been accomplished only with great difficulty by Mehta.[23]

Finite difference procedures appear to be more promising for computing the base flow field. So far as the author knows, the only finite difference techniques applied to the full conservation equations for the supersonic base flow problem were the explicit methods of Allen and Cheng[24] and of Roache and Mueller.[25] For the latter case, however, relatively little information about the solution was provided. The Allen and Cheng method computed the steady state solution by solving the unsteady equations for asymptotically large time. However, much

computation time was required because the method, as all explicit methods, is subject to one or more stability restrictions on the time step size relative to the spatial grid size. These stability criteria are the well known Courant-Friedrichs-Lewy (CFL) condition (in one dimension, $\Delta t_{CFL} \leq \Delta x/((|u| + c))$ and, in some methods, a viscous stability limit ($\Delta t \leq \Delta x^2/2\nu$). Since the maximum time step size is related to the spatial grid size, when accuracy is desired and a fine mesh is used, the computation time correspondingly increases.

Implicit methods, on the other hand, tend to be stable for much larger time steps. Hence they offer the prospect of faster solution than explicit methods, provided the computation time per time step is comparable to that of explicit methods. When applied to one-dimensional equations using central differencing, an implicit method usually gives a linear system with a tridiagonal coefficient matrix which is easily and quickly solved. Multidimensional problems, however, give more complicated coefficient matrices which are time consuming to solve. Further the equations need to be suitably linearized before application of the implicit technique. Briley and McDonald[26] have proposed a procedure which linearizes the unsteady equations in time by Taylor series expansion about the known time level. It preserves the efficiency of one-dimensional systems by applying an Alternating-Direction-Implicit (ADI) procedure, in which the equations are considered implicit in one direction at a time. The particular ADI scheme used here is that of Douglas & Gunn.[27]

This method is tentative because Briley and McDonald only applied the method to a subsonic duct flow with no recirculation. This is very different from the supersonic base flow problem, and the ability to

compute shocks and recirculation, for example, needs to be proven. In addition, Briley and McDonald never established the accuracy of the method by comparing with experimental data or an exact solution. At most they have only shown qualitative agreement with approximate (i.e., one-dimensional exact) analyses. Nevertheless, the method appears to be promising in not being subject to stability limits on the time step size and in retaining the computational speed of one-dimensional implicit systems.

In this thesis, the Briley and McDonald[26] procedure was applied to the governing equations, and the cell integration technique was applied to derive the finite difference equations. In brief, the governing equations were linearized in time by a Taylor series expansion about the known (or n^{th}) time level. The finite difference equations were derived by applying the cell integration technique, which leads to central differencing for the interior grid points. Application of the ADI procedure leads to sequences of one-dimensional implicit systems having block tridiagonal coefficient matrices. Each of these systems (one sequence of systems for each coordinate direction) is solved by the standard block elimination technique as outlined in Isaacson and Keller.[28] No iteration is required to compute the solution for a given time step.

The method was checked against the previous laminar, supersonic base flow calculations of Allen and Cheng[24] and Kronzon, et al.[29] This allowed a check of the capability of this implicit method to compute a flow with shocks, reverse flow, high transverse pressure gradients, and a wide variety of boundary conditions. It also allowed a check on the

ability of the method to compute a solution in less time than by an explicit method.

CHAPTER II

GOVERNING EQUATIONS

The governing equations are the conservation equations for mass, x-momentum, y-momentum, and energy, and the equation of state for the two dimensional flow of a perfect gas with constant specific heats. The differential equations are written in the conservation form. As Roache[30] shows (p. 28), when the conservation form is used, then the finite difference equations preserve the integral Gauss divergence property of the continuum equation. His example illustrates the algebraic balance of flux quantities and accumulation rates in a small control volume. This has an intuitive appeal. In addition, Roache points out that the Rankine-Hugoniot relations were derived from the conservation form and hence the jump conditions across a shock are automatically satisfied. No special treatment is given for the formation of shocks if they develop. This is called "shock-capturing" or "shock-smearing." (In the Russian literature this is called a "through" method. See Roache[30] p. 227).

The dimensional equations are:

$$\frac{\partial \rho}{\partial t} = - \frac{\partial}{\partial x} (\rho u) - \frac{\partial}{\partial y} (\rho v) \tag{2-1}$$

$$\frac{\partial (\rho u)}{\partial t} = - \frac{\partial}{\partial x} [\rho u^2 + p - \tau_{xx}] - \frac{\partial}{\partial y} [\rho uv - \tau_{xy}] \tag{2-2}$$

$$\frac{\partial(\rho v)}{\partial t} = -\frac{\partial}{\partial x}\left[\rho uv - \tau_{xy}\right] - \frac{\partial}{\partial y}\left[\rho v^2 + p - \tau_{yy}\right] \tag{2-3}$$

$$\frac{\partial}{\partial t}\left[\rho e + \frac{\rho}{2}(u^2+v^2)\right] = -\frac{\partial}{\partial x}\left[\rho u\left(e + \frac{p}{\rho} + \frac{(u^2+v^2)}{2}\right) - q_x\right] - \frac{\partial}{\partial y}\left[\rho v\left(e + \frac{p}{\rho} + \frac{(u^2+v^2)}{2}\right) - q_y\right] + \frac{\partial}{\partial x}(u\tau_{xx} + v\tau_{xy}) + \frac{\partial}{\partial y}(u\tau_{xy} + v\tau_{yy}) - \left[\tau_{xx}\frac{\partial u}{\partial x} + \tau_{xy}\left(\frac{\partial u}{\partial y} + \frac{\partial v}{\partial x}\right) + \tau_{yy}\frac{\partial v}{\partial y}\right] \tag{2-4}$$

$$p = (\gamma - 1)\, e \tag{2-5}$$

where:

$$\tau_{xx} = \mu\left(\frac{4}{3}\frac{\partial u}{\partial x} - \frac{2}{3}\frac{\partial v}{\partial y}\right) \tag{2-6}$$

$$\tau_{xy} = \mu\left(\frac{\partial u}{\partial y} + \frac{\partial v}{\partial x}\right) \tag{2-7}$$

$$\tau_{yy} = \mu\left(\frac{4}{3}\frac{\partial v}{\partial y} - \frac{2}{3}\frac{\partial u}{\partial x}\right) \tag{2-8}$$

$$q_x = -\frac{\gamma k}{c_p}\frac{\partial e}{\partial x} \tag{2-9}$$

$$q_y = -\frac{\gamma k}{c_p}\frac{\partial e}{\partial y} \tag{2-10}$$

Here c_p, γ, k, and μ are assumed to be constant. (The case of temperature variation of these quantities is a straightforward extension if done explicitly.) Bulk viscosity was assumed to be zero.

Great utility is afforded by nondimensionalizing the equations. Then, different flow conditions can be characterized easily by a small set of nondimensional parameters rather than having to change all the dimensional parameters. The following convention was used:

$$\bar{x} = \frac{x}{H} \qquad \bar{y} = \frac{y}{H} \qquad \bar{t} = \frac{u_1}{H}$$

$$\bar{\rho} = \frac{\rho}{\rho_1} \quad \bar{u} = \frac{u}{u_1} \quad \bar{v} = \frac{v}{u_1} \quad \bar{e} = \frac{e}{e_1}$$

$$\bar{p} = \frac{p}{p_1} \quad \bar{\mu} = \frac{\mu}{\mu_1} = 1 \quad \bar{k} = \frac{k}{k_1} = 1$$

where H = base half height and subscript 1 denotes freestream quantities.

Substituting these quantities into the conservation equations, eliminating pressure with the state equation, and dropping the overbars equations (2-1) through (2-4) become

$$\frac{\partial}{\partial t} = -\frac{\partial}{\partial x}(\rho u) - \frac{\partial}{\partial y}(\rho v) \tag{2-11}$$

$$\frac{\partial \rho u}{\partial t} = -\frac{\partial}{\partial x}\left[\rho u^2 + \left(\frac{1}{\gamma M_1^2}\right)\rho e - \frac{1}{Re}\left(\frac{4}{3}\frac{\partial u}{\partial x} - \frac{2}{3}\frac{\partial v}{\partial y}\right)\right] - \frac{\partial}{\partial y}\left(\rho uv - \frac{1}{Re}\left(\frac{\partial u}{\partial y} + \frac{\partial v}{\partial x}\right)\right] \tag{2-12}$$

$$\frac{\partial \rho v}{\partial t} = -\frac{\partial}{\partial x}\left[\rho uv - \frac{1}{Re}\left(\frac{\partial u}{\partial y} + \frac{\partial v}{\partial x}\right)\right] - \frac{\partial}{\partial y}\left[\rho v^2 + \left(\frac{1}{\gamma M_1^2}\right)\rho e - \frac{1}{Re}\left(\frac{4}{3}\frac{\partial v}{\partial y} - \frac{2}{3}\frac{\partial u}{\partial x}\right)\right] \tag{2-13}$$

$$\frac{\partial}{\partial t}\left[\rho e + \frac{\rho K}{2}(u^2 + v^2)\right] = -\frac{\partial}{\partial x}\left[\rho u\left(\gamma e + \frac{K}{2}(u^2 + v^2)\right) + \gamma q_x\right]$$

$$-\frac{\partial}{\partial y}\left[\rho v\left(\gamma e + \frac{K}{2}(u^2 + v^2)\right) + \gamma q_y\right] + K\left\{\left[\frac{\partial}{\partial x}(u\tau_{xx} + v\tau_{xy})\right.\right.$$

$$\left.\left. + \frac{\partial}{\partial y}(u\tau_{xy} + v\tau_{yy})\right] - \left[\tau_{xx}\frac{\partial u}{\partial x} + \tau_{xy}\left(\frac{\partial u}{\partial y} + \frac{\partial v}{\partial x}\right) + \tau_{yy}\frac{\partial v}{\partial y}\right]\right\} \tag{2-14}$$

where:

$$\tau_{xx} = \frac{1}{Re}\left(\frac{4}{3}\frac{\partial u}{\partial x} - \frac{2}{3}\frac{\partial v}{\partial y}\right) \tag{2-15}$$

$$\tau_{xy} = \frac{1}{Re}\left(\frac{\partial u}{\partial y} + \frac{\partial v}{\partial x}\right) \tag{2-16}$$

$$\tau_{yy} = \frac{1}{Re}\left(\frac{4}{3}\frac{\partial v}{\partial y} - \frac{2}{3}\frac{\partial u}{\partial x}\right) \tag{2-17}$$

$$q_x = -\frac{1}{RePr}\frac{\partial e}{\partial x} \tag{2-18}$$

$$q_y = -\frac{1}{RePr}\frac{\partial e}{\partial y} \tag{2-19}$$

$$K = \gamma(\gamma-1)M_1^2 \qquad M_1^2 = \frac{u_1^2}{\gamma(\gamma-1)e_1}$$

$$Re = \frac{\rho_1 u_1 H}{\mu_1} \qquad Pr = \frac{\mu_1 c_p}{k_1}$$

These are the equations solved in the program along with boundary conditions which are derived for the geometry illustrated in Figure 2. The finite difference grid for the flow field is shown in Figure 3. Note that only half of the flow field is computed (the upper half) since the flow is assumed symmetric about the central plane (DE). The flow is two-dimensional, planar over the rectangular corner BCD. The incoming flow is supersonic with a boundary layer on the upper wall. Details of the boundary and initial conditions are given in Chapter 5.

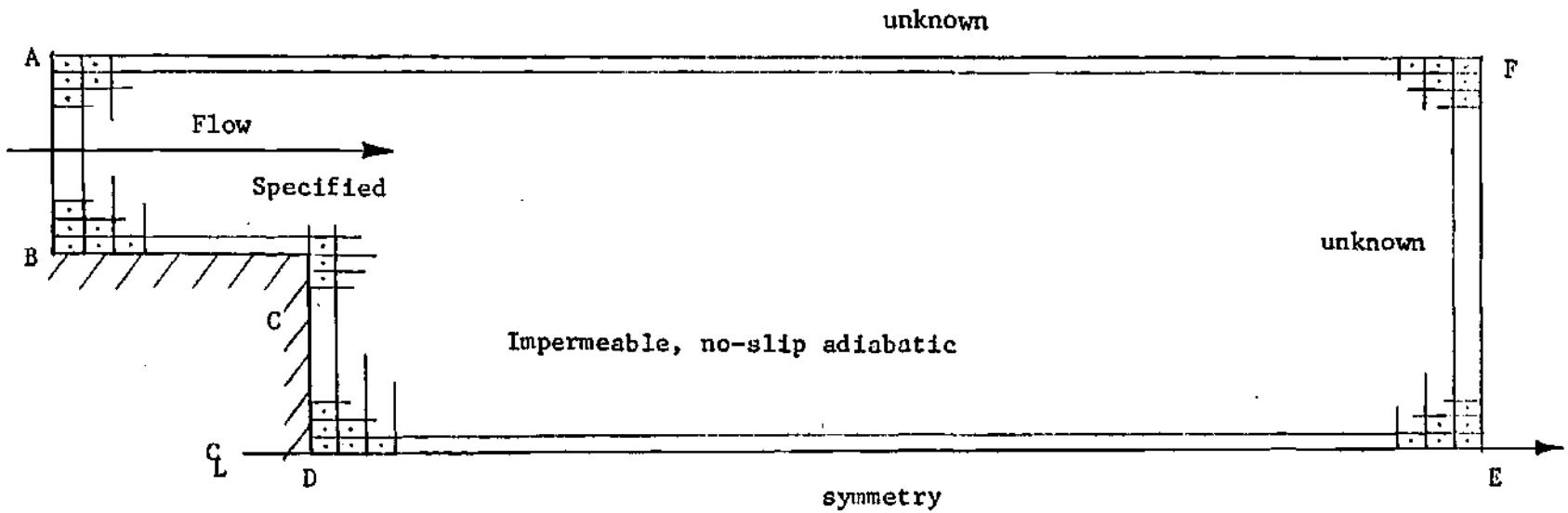

Figure 3. Flow Field Boundary and Grid (not to scale).

CHAPTER III

NUMERICAL PROCEDURE

The unsteady equations are parabolic in time and at each time step the simultaneous solution of the equations for the whole flow field is required. Numerically, this means the solution of a linear system (for implicit methods) which, in turn, requires the linearization of the non-linear terms at the implicit time level. This is accomplished by a Taylor series expansion about the solution at the known time level as outlined in Briley and McDonald.[26] They point out that this procedure, adapted for the integration of initial-value problems, permits the computationally efficient solution of coupled, non-linear equations in one space dimension by a one-step non-iterative scheme. The efficiency is retained for multidimensional problems by using alternating-direction implicit (ADI) techniques. As an example of the linearization, the continuity equation (2-11) becomes:

$$\frac{(\rho^{n+1}-\rho^{n})}{\Delta t} = -\frac{\partial}{\partial x}(\rho u)^{n+1} - \frac{\partial}{\partial x}(\rho v)^{n+1}$$

$$= -\frac{\partial}{\partial x}\left[(\rho u)^{n} + \left(u\frac{\partial \rho}{\partial t} + \rho\frac{\partial u}{\partial t} + \rho\frac{\partial u}{\partial t}\right)^{n}\Delta t\right] - \frac{\partial}{\partial y}\left[(\rho v)^{n} + \rho\frac{\partial v}{\partial t}\right)^{n}\Delta t]$$

or

$$\frac{(\rho^{n+1}-\rho^{n})}{\Delta t} = -\frac{\partial}{\partial x}[\rho^{n+1}u^{n} + \rho^{n}u^{n+1} - \rho^{n}u^{n}] - \frac{\partial}{\partial y}[\rho^{n+1}v^{n} + \rho^{n}v^{n+1} - \rho^{n}v^{n}] \tag{3-1}$$

Equation (3-1) is linear in the unknown (or n+1) variables. The complete set of linearized equations is given in Appendix A.

To obtain the finite difference form of the equations, the cell integration technique is used. This technique is best illustrated by example. Consider the differential equation for conservation of mass, using Cartesian tensor notation:

$$\partial\rho/\partial t + \partial\rho u_i/\partial x_i = 0 \tag{3-2}$$

This equation is integrated over a control volume (cv) which is a cell of dimensions Δx, Δy, Δz. Thus

$$\iiint_{cv} (\partial\rho/\partial t)dv = -\iiint_{cv} (\partial\rho u_i/\partial x_i)dv$$

$$= -\iint_{cs} \rho u_i n_i dA \tag{3-3}$$

using Gauss' theorem. For two-dimensional flow, the area integral over the control surface becomes:

$$\iint_{cs} \rho u_i n_i dA = \iint_{x+} \rho u \, dydz + \iint_{x-} \rho u(-1)dydz$$

$$+ \iint_{y+} \rho v \, dxdz + \iint_{y-} \rho v(-1) \, dxdz \tag{3-4}$$

where x+, x-, y+, y- are the control surface or cell edges (see Figure 4). Next, the following approximations are made:

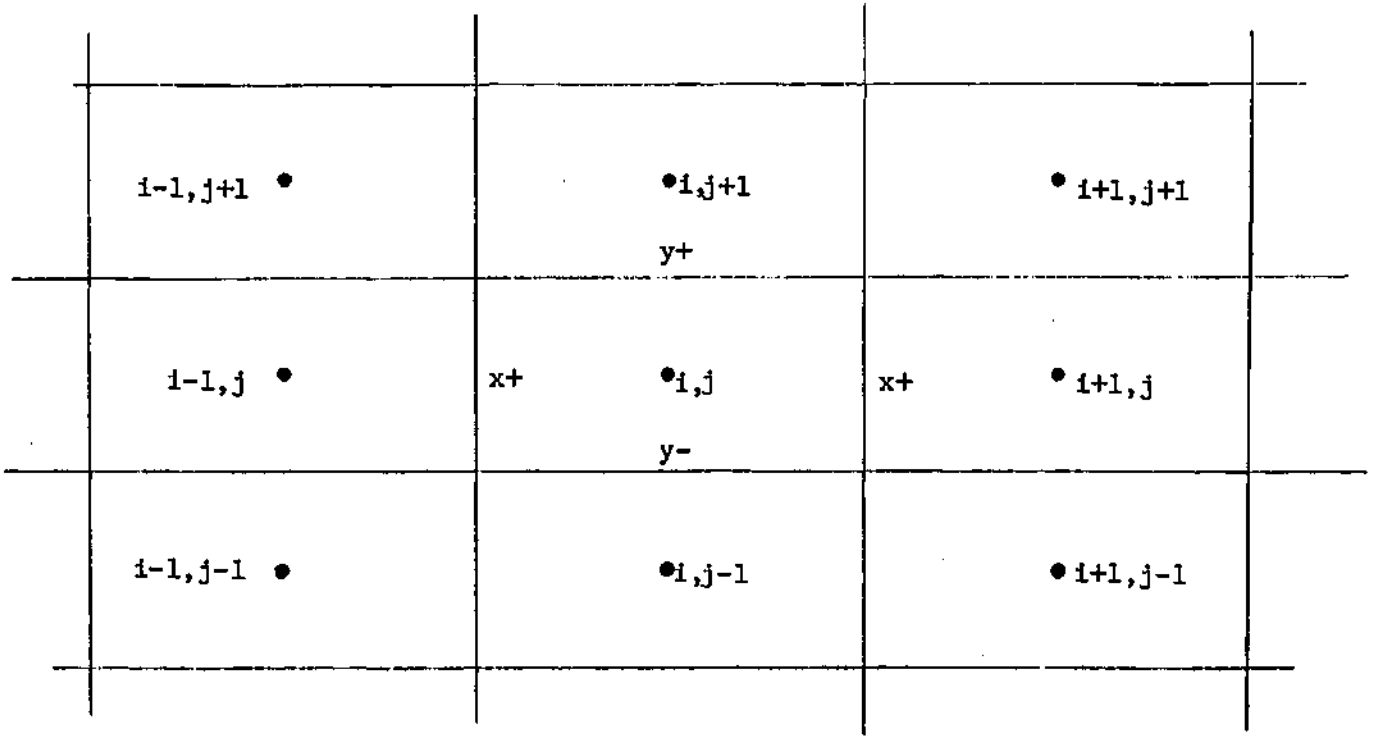

Figure 4. Typical Grid Point.

$$\iiint_{cv} (\partial\rho/\partial t)dv \cong (\partial\rho/\partial t)ij\ \Delta x\ \Delta y\Delta z$$

$$\iint_{x+} \rho u\ dydz \cong (\rho u)_{x+}\ \Delta y\Delta z \qquad (3\text{-}5)$$

etc.

Equation (3-4) then becomes

$$(\partial\rho/\partial t)ij = -\frac{1}{\Delta x}\left[(\rho u)_{x+} - (\rho u)_{x-}\right] - \frac{1}{\Delta y}\left[(\rho v)_{y+} - (\rho v)_{y-}\right]$$

or

$$\partial\rho/\partial t = -\delta x(\rho u) - \delta y(\rho v) \qquad (3\text{-}6)$$

when $(\rho u)_{x+}$, for example, is taken as the average between $(\rho u)_{ij}$ and $(\rho u)_{i+1,j}$ and similarly for $(\rho u)_{x-}$, then $\partial x(\rho u)$ becomes the standard central difference form. The chief advantage in using this formulation is the conceptual aid afforded in applying the boundary conditions. With this technique all spatial derivatives are related to values at the cell edges. Thus, when boundaries are adjacent to cell edges it becomes clear which terms must be modified to match the boundary condition. The complete set of finite difference equations is given in Appendix B. For interior points, the value of a quantity on a cell edge is always taken as the average of the cell points on either side of the edge. A derivative at the cell edge is always the difference of the two nearest cell points. Thus, for example

$$(\rho u)_{x+} = \frac{1}{2}\left[(\rho u)_{ij} + (\rho u)_{i+1,j}\right] \qquad (3\text{-}7)$$

$$\left[\frac{\partial}{\partial x}(\rho u)\right]_{x+} = \frac{1}{\Delta x}\left[(\rho u)_{i+1,j} - (\rho u)_{ij}\right] \qquad (3\text{-}8)$$

When these are carried out for all the cell edges, the result is central differencing. For example

$$\delta x(\rho u) = \frac{1}{\Delta x}\left[(\rho u)_{x+} - (\rho u)_{x-}\right] = \frac{1}{\Delta x}\left[\frac{(\rho u)_{i+ij} + (\rho u)_{ij}}{2} - \frac{(\rho u)_{ij} + (\rho u)_{i-1j}}{2}\right]$$

$$= \frac{1}{2\Delta x}\left[(\rho u)_{i+1j} - (\rho u)_{i-1j}\right]$$

then equation (3-1) can be written as:

$$a^n \phi^{n+1}_{i+1j} + b^n \phi^{n+1}_{ij+1} + c^n \phi^{n+1}_{ij} + d^n \phi^{n+1}_{i-1j} + e^n \phi^{n+1}_{ij-1} = f^n \qquad (3\text{-}9)$$

where a^n, b^n, c^n etc. are coefficient matrices containing only n-level quantities, f^n is the finite difference form of the explicit part of equation (3-1), and ϕ_{ij} is the column vector containing the dependent variables at point ij. If a single row or column of grid points were being solved by equation (3-9) (as in a one-dimensional problem) the result would be a block-tridiagonal matrix which could be quickly solved by a standard elimination technique. Application of equation (3-9) to a field of many rows or columns of points results in a large cumbersome matrix which can be solved by Gauss elimination or some iterative technique. The computation time required for solution by either method increases rapidly with the size of the grid.

As mentioned previously, the computation time of solution for a one-dimensional problem is retained by use of ADI techniques. Of the many ADI schemes (see, for example, Yanenko[31]), Briley and McDonald use a form of the general procedure of Douglas and Gunn. This procedure

generates the ADI scheme as perturbations of the fundamental implicit scheme. It is a multistep method (one step for each spatial dimension) where the first step approximates the implicit equation and subsequent steps add corrections. Yanenko calls this the "method of stabilizing corrections" and shows that the method has the two important properties of consistency and stability. Briley and McDonald point out that the consistency property allows for the use of physical boundary conditions for the intermediate step with no loss in accuracy for steady state solutions.

Each step of the procedure involves the implicit solution in one of the coordinate directions. This results in a system of one-dimensional, block tridiagonal matrices which are easily solved by standard block elimination methods. As an example, applying the ADI scheme to equation (3-1) gives:

$$\frac{(\rho^{*} - \rho^{n})}{\Delta t}_{ij} = -\delta x[\rho^{*}u^{n} + \rho^{n}u^{*} - \rho^{n}u^{n}]_{ij} - \delta y[\rho^{n}v^{n}]_{ij} \qquad (3\text{-}10)$$

$$\frac{(\rho^{**} - \rho^{n})}{\Delta t}_{ij} = \delta x[\rho^{*}u^{n} + \rho^{n}u^{*} - \rho^{n}u^{n}]_{ij} - \delta y[\rho^{**}v^{n} + \rho^{n}v^{**} - \rho^{n}v^{n}]_{ij} \qquad (3\text{-}11)$$

where * indicates the intermediate quantity given by equation (3-10) and ** represents the quantity evaluated by equation (3-11). The complete set of ADI equations is given in Appendix C. Now, equations (3-10) and (3-11) can be written as

$$\frac{(\rho^{*} - \rho^{n})}{\Delta t}_{ij} = Dx^{n}\phi^{*} + Dy^{n}\phi^{n} + Sn \qquad (3\text{-}12)$$

$$\left(\frac{\rho^{**} - \rho^{n}}{\Delta t}\right)_{ij} = Dx^{n}\phi^{*} + Dy^{n}\phi^{**} + Sn \qquad (3\text{-}13)$$

where

$$Dx^{n} = \left|- \delta x\{u^{n}\} \quad -\delta x\{\rho^{n}\} \quad 0 \right|$$

$$Dy^{n} = \left|- \delta y\{v^{n}\} \quad 0 \quad -\delta y\{\rho^{n}\}\right|$$

$$Sn = \delta x(\rho^{n}u^{n}) + \delta y(\rho^{n}v^{n}) \quad \phi = \left|\begin{matrix} C \\ v \end{matrix}\right|$$

and

{ } implies multiplication with ϕ before the difference operation is applied.

Now ϕ^{*} is computed in the intermediate equation (3-12) and ϕ^{**} is obtained in (3-13). According to Douglas and Gunn.[27] ϕ^{**} is within $\theta(\Delta t^{2})$ of ϕ^{n+1} and so is taken at ϕ^{n+1}. The system can be simplified by subtracting (3-12) from (3-13) to get the new system:

$$\left(\frac{\rho^{*} - \rho^{n}}{\Delta t}\right)_{ij} = Dx^{n}\phi^{*}_{ij} + Dy^{n}\phi^{n}_{ij} + S^{n} \qquad (3\text{-}14)$$

$$\left(\frac{\rho^{**} - \rho^{*}}{\Delta t}\right)_{ij} = Dy^{n}(\phi^{**}_{ij} - \phi^{n}_{ij}) \qquad (3\text{-}15)$$

Equations (3-14) and (3-15) can be written as:

$$\overline{\overline{c}}^{n}_{i}\,\phi^{*}_{i-1j} + \overline{\overline{b}}^{n}_{i}\,\phi^{*}_{ij} + \overline{\overline{a}}^{n}_{i}\,\phi^{*}_{i+1j} = \overline{d}^{n}_{i} \qquad (3\text{-}16)$$

$$\overline{\overline{\gamma}}^{n}_{j}\,\phi^{**}_{ij-1} + \overline{\overline{\beta}}^{n}_{i}\,\phi^{**}_{ij} + \overline{\overline{\alpha}}^{n}_{i}\,\phi^{**}_{ij+1} = \overline{\xi}^{*}_{j} + \overline{\eta}^{n}_{j} \qquad (3\text{-}17)$$

where $\overline{\overline{c}}^{n}_{i}$, $\overline{\overline{b}}^{n}_{i}$, etc. are the coefficient matrices of the unknowns

ϕ^*_{i-1j}, ϕ^*_{ij}, etc. The column vectors $\bar{d}^n_i$, $\bar{\xi}^*_j$, and $\bar{\eta}^n_j$ contain the explicit terms. The order of the coefficient matrices is equal to the number of dependent variables. The forms of $\bar{\bar{a}}^n_i$, $\bar{\bar{b}}^n_i$, $\bar{\bar{c}}^n_i$, etc. come from the finite difference equations, and, for the interior points, all have the same form. (See Appendix D.) For points adjacent to a boundary, the finite differencing must be modified. These modifications are discussed in Chapter V.

The solution for a single time step, then, proceeds as follows:

1. Equation (3-16) is applied at successive rows (x-direction) to generate a series of coupled, one-dimensional equations (there being one set of coefficient matrices $\bar{\bar{a}}^n_i$, $\bar{\bar{b}}^n_i$, $\bar{\bar{c}}^n_i$ and a $\bar{d}^n_i$ for each point in the row), which are arranged into one block-tridiagonal matrix for each row. The matrix is then solved by a standard block elimination technique (see Chapter IV) to give the values of ϕ^*.
2. The second step is similar to the first except that equation (3-17) is applied to successive columns (y-direction), which gives the ϕ^{**} vector for the flow field.

It should be noted that the "splitting" of the Douglas-Gunn procedure can be done in any coordinate direction and does not require association with coordinate directions. The criteria used is that the associated matrices are easily solved. The mixed derivatives can be treated implicitly, therefore, but this increases the number of intermediate steps and greatly complicates the procedure and was not done here. Thus, as the method was applied, it was not totally implicit.

Experience has shown that this does not seem to hinder the ability of the scheme to use larger time steps than those required by the viscous stability requirement. Briley and McDonald, for example were able to use $\Delta t = 20.6\ \Delta t_\mu$ (where $\Delta t_\mu = (\Delta x)^2/2\nu$) and $\Delta t = 1471\ \Delta t_{CFL}$. They point out that explicit treatment of a dissipation term and $\nabla \cdot u$ appeared not to affect the stability of the procedure, even at these large time steps. Hence, it was deemed not necessary to compute mixed derivatives implicitly. Subsequent experience with computations for supersonic base flow confirmed this.

CHAPTER IV

MATRIX SOLUTION

Equations (3-16) and (3-17) generate a series of coupled, linear, one-dimensional equations for each row and each column of grid points in the flow field. Each series of equations represents a complete block-tridiagonal matrix system which, as previously mentioned, can be solved by standard techniques. The one used here is the L-U decomposition and back-substitution (LUBS) method described by Isaacson and Keller.[28]

To illustrate the procedure consider the solution along the jth row of grid points. At each point, Eq. (3-16) gives:

$$\bar{\bar{C}}_i^n \phi_{i-1j}^* + \bar{\bar{b}}_i^n \phi_{ij}^* + \bar{\bar{a}}_i^n \phi_{i+1j}^* = \bar{d}_i^n$$

For the whole row, the system emerges as:

$$\begin{vmatrix} b_1^n & a_1^n & & & & \\ c_2^n & b_2^n & a_2^n & & & \\ & c_3^n & b_3^n & a_3^n & & \\ & & \ddots & \ddots & \ddots & \\ & & & & a_{N-1}^n & \\ & & & c_N^n & b_N^n & \end{vmatrix} \begin{vmatrix} \phi_{ij}^* \\ \phi_{2j}^* \\ \phi_{3j}^* \\ \vdots \\ \phi_{N-1,j}^* \\ \phi_{Nj}^* \end{vmatrix} = \begin{vmatrix} d_1^n \\ d_2^n \\ d_3^n \\ \\ d_{N-1}^n \\ d_N^n \end{vmatrix}$$

where N is the number of grid points in a row. Now each of the coefficients c_i^n, b_i^n, and a_i^n are themselves square matrices of the order k, the number of dependent variables.

The first step is to convert the coefficient matrix to the product of the upper and lower triangular matrices (hence the name LU decomposition).

$$\begin{vmatrix} b_1' & & & & \\ c_2 & b_2' & & & \\ & c_3 & b_3' & & \\ & & \ddots & \ddots & \\ & & & c_n & b_N \end{vmatrix} \begin{vmatrix} I & a_1' & & & \\ & I & a_2' & & \\ & & I & a_3' & \\ & & & \ddots & \ddots \\ & & & & I \end{vmatrix} = LU$$

where I = identity matrix.

This is accomplished by using the recursion formulas:

$$b_1' = b_1 \qquad a_1' = b_1^{-1} a_1 \tag{4-1}$$

$$b_i' = b_i - c_i a_{i-1}' \qquad (i = 2,3,\ldots,N) \tag{4-2}$$

$$a_i' = (b_i')^{-1} a_i \qquad (i = 2,3,\ldots,N-1) \tag{4-3}$$

Hence, the system becomes:

$$UL\phi = d \; ; \quad \phi = \begin{vmatrix} \phi_1 \\ \phi_2 \\ \cdot \\ \cdot \\ \cdot \\ \phi_N \end{vmatrix} \; ; \quad d = \begin{vmatrix} d_1 \\ d_2 \\ \cdot \\ \cdot \\ \cdot \\ d_N \end{vmatrix} \tag{4-4}$$

which is solved as

$$Uy = d \; ; \quad L\phi = y \; ; \quad y = \begin{vmatrix} y_1 \\ y_2 \\ \cdot \\ \cdot \\ \cdot \\ y_N \end{vmatrix} \tag{4-5}$$

Recursions, for y and ϕ are:

$$y_1 = (b_1')^{-1} d_1; \; y_i = (b_i')^{-1}(d_i - c_i y_{i-1}) \quad (i = 2,3,\ldots,N) \tag{4-6}$$

and

$$\phi_N = y_N; \; \phi_i = y_i - a_i' \phi_{i+1} \quad (i = N-1, N-2,\ldots,1) \tag{4-7}$$

This method is seen to take full advantage of the large number of zeros in the matrix by performing operations only on the nonzero elements of the coefficient matrix. It is thus seen as particularly efficient and suitable for use in a computer program. Further computational efficiency is gained if equations (4-1), (4-3) and (4-6) are solved, not as written by inverting the b_i matrix, but by solving the linear system with b_i on the left hand side of the equation. Gauss elimination, for example, was used in this problem, though other techniques could be used. The question arises, in the solution of the small linear system with b_i on the left hand side, as to whether a pivoting strategy would aid in the reduction of any round off error. These round off errors may arise, for example, from the fact that so many arithmetic operations are being performed even in the solution of one row of grid points. A check for

round-off errors was made for this problem by making a single computation using double precision (single precision on the CDC 6600 of the Georgia Tech CYBER 74 is 14 decimal places). This computation was run for 100 time steps and the results were identical to a computation made using single precision arithmetic. Thus no pivoting appeared necessary.

CHAPTER V

BOUNDARY AND INITIAL CONDITIONS

The finite difference equations all have the same form when applied to interior grid points. When a cell is adjacent to a boundary these equations must be modified. This chapter presents the modified forms of the finite difference equations for the various boundaries encountered in the flow field.

While all flows are governed by the same set of equations, the variety of phenomena (bubbles, shocks, recirculation, etc.) arise due to differing boundary conditions. It follows that these boundary conditions in a numerical study must be specified carefully, as was indeed discovered. The cell integration formulation affords great conceptual aid here, in that it becomes clear which group of terms needs to be modified. The problem becomes one of choosing among several plausible forms. Most of these forms are outlined in Roache.

Complicating the matter is the fact that appropriate forms appear to vary with solution procedure. Roache cites several instances where one form gave good results for some methods, but caused numerical divergence in others (see, for example, Roache,[30] p. 280). Allen and Cheng even found that near-wall flux terms needed to be modified within the same method for a finer mesh to get physically meaningful densities. This is not to imply that only a single form will work in a given condition; just that the solution can be very sensitive to form change. The

solution can also be quite insensitive to different forms. Many forms for the viscous terms near and on the walls were tired, and gave negligible changes in the solution. It is not surprising then, that a major effort was required to arrive at appropriate modifications of the finite difference equations for the edge regions.

The remainder of this chapter presents the final forms of the boundary conditions used for solution. A more complete discussion of other boundary condition forms considered is given in Chapter VI, Results. Only the conditions for laminar flow are given here. The extension of this method to turbulent flow and associated boundary conditions is given in Bangert and Roach.

5.1 Upper Wall

The upper wall, labeled BC in Figure 3, is no-slip, impermeable, and adiabatic. A cell adjacent to BC (see Figure 5) must then have

$$(u)_{y-} = 0 \tag{5-1}$$

$$(v)_{y-} = 0 \tag{5-2}$$

and,

$$(\partial e/\partial y)_{y-} = 0 \tag{5-3}$$

Equations (5-1) and (5-2) imply:

$$(\partial u/\partial x)_{y-} = 0 \tag{5-4}$$

$$(\partial v/\partial x)_{y-} = 0 \tag{5-5}$$

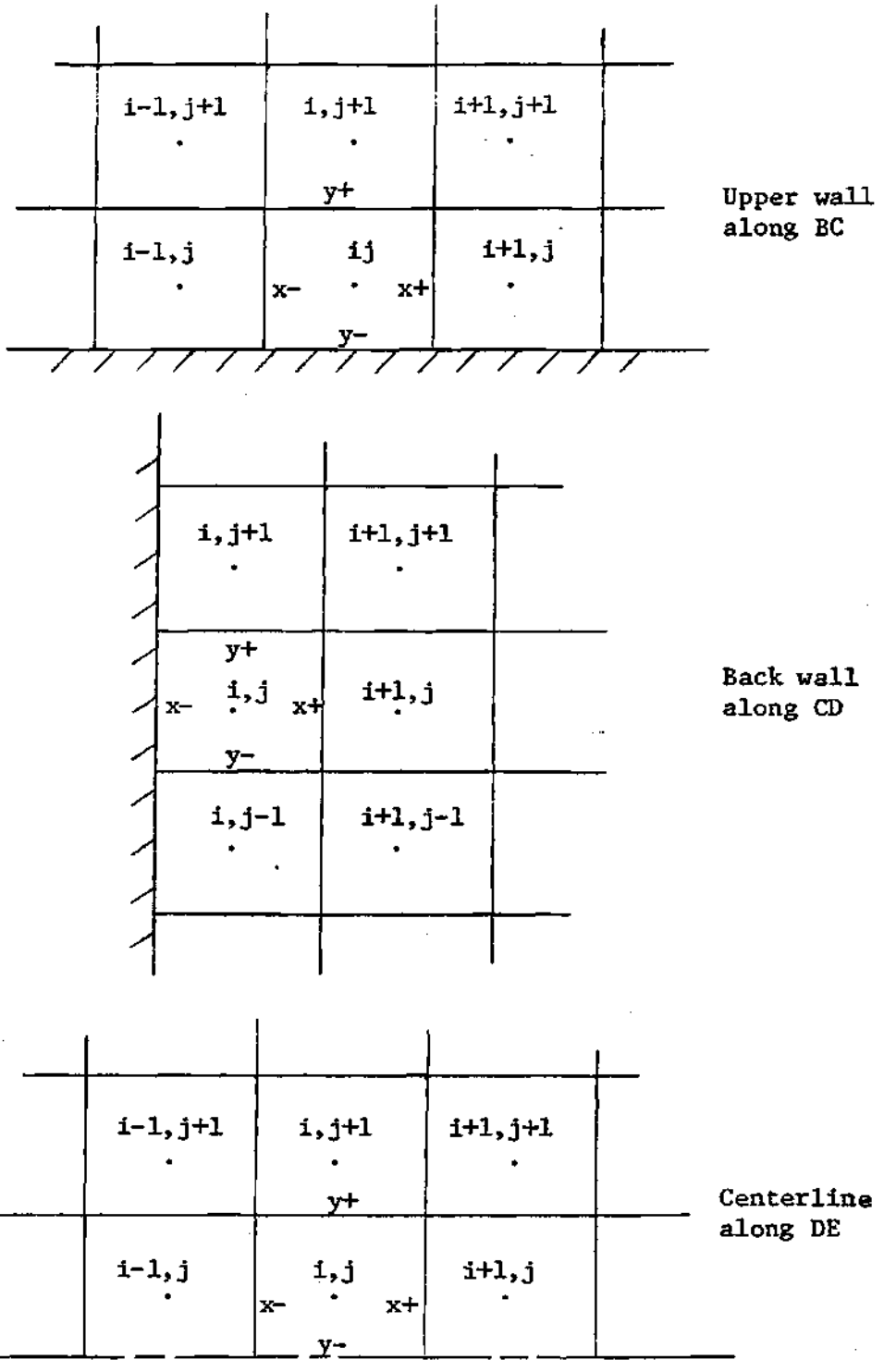

Figure 5. Boundary Cells - Upper Wall, Back Wall and Centerline.

Similarly, the shear work terms (from the energy equation) on the wall are zero:

$$[\frac{\mu}{Re} (\partial u/\partial y + \partial v/\partial x)u]_{y-} = 0 \qquad (5\text{-}6)$$

$$[\frac{\mu}{Re} (\frac{4}{3} \partial v/\partial y - \frac{2}{3} \partial u/\partial x)v]_{y-} = 0 \qquad (5\text{-}7)$$

The nondimensional pressure at the wall, $(\rho e)_{y-}$, was evaluated by a linear extrapolation through (ij) and (i,j+1) giving,

$$(\rho e)_{y-} = \frac{1}{2}[3(\rho e)_{ij} - (\rho e)_{ij+1}] \qquad (5\text{-}8)$$

This technique was also used by Allen and Cheng.

When normal derivatives are required at the surface, a second-order accurate, one-sided difference was used:

$$(\partial \phi/\partial y)_{y-} = \frac{1}{3\Delta y} (-8\phi_{y-} + 9\phi_{ij} - \phi_{ij+1}) \qquad (5\text{-}9)$$

thus

$$(\frac{\partial u}{\partial y})_{y-} = \frac{1}{3\Delta y} (9u_{ij} - u_{ij+1}) \qquad (5\text{-}10)$$

and

$$(\frac{\partial v}{\partial y})_{y-} = \frac{1}{3\Delta y}(9v_{ij} - v_{ij+1}) \qquad (5\text{-}11)$$

5.2 Back Wall

This wall, labeled CD in Figure 3, is also impermeable, no-slip, and adiabatic. A cell, then, with the wall on the x-edge (see Figure 5) has:

$$(u)_{x-} = 0 \tag{5-12}$$

$$(v)_{x-} = 0 \tag{5-13}$$

and,

$$(\partial e/\partial x)_{x-} = 0 \tag{5-14}$$

Equations (5-12) and (5-13) imply that:

$$(\partial u/\partial y)_{x-} = 0 \tag{5-15}$$

$$(\partial v/\partial y)_{x-} = 0 \tag{5-16}$$

also:

$$\left[\frac{\mu}{Re}\left(\frac{4}{3}\frac{\partial u}{\partial x} - \frac{2}{3}\frac{\partial v}{\partial y}\right)u\right]_{x-} = 0 \tag{5-17}$$

$$\left[\frac{\mu}{Re}\left(\frac{\partial u}{\partial y} + \frac{\partial v}{\partial x}\right)v\right]_{x-} = 0 \tag{5-18}$$

using the second-order form for the normal derivatives, similar to Equation (5-9), gives:

$$(\partial u/\partial x)_{x-} = \frac{1}{3\Delta x}\left(9u_{ij} - u_{i+ij}\right) \tag{5-19}$$

and

$$(\partial v/\partial x)_{x-} = \frac{1}{3\Delta x}\left(9v_{ij} - v_{i+ij}\right) \tag{5-20}$$

The form used for the pressure on the back wall was not the extrapolation used as on BC, but rather:

$$(\rho e)_{x-} = \frac{1}{8}\left(9\rho e_{ij} - \rho e_{i+1j}\right) \tag{5-21}$$

Note that this form is equivalent to a zero pressure gradient normal to the wall at x-using the second-order form for normal derivatives. The reason for the use of this form is given in Chapter VI in the section on boundary conditions.

5.3 Centerline

The centerline, labeled DE in Figure 3, is a plane of symmetry and thus has no mass flux across it. A typical cell (see Figure 5) is adjacent to DE at its y- edge. So

$$(v)_{y-} = 0 \tag{5-22}$$

$$(\partial v/\partial x)_{y-} = 0 \tag{5-23}$$

and

$$(\partial \phi/\partial y) = 0 \quad (\phi \neq v) \tag{5-24}$$

The second order form for the derivatives, eq. (5-9) is used for the normal derivative of v:

$$(\partial v/\partial y)_{y-} = \frac{1}{3\Delta y}\,(9v_{ij} - v_{ij+1}) \tag{5-25}$$

and also gives a consistent form for the nonzero variables at y-:

$$(\phi)_{y-} = \frac{1}{8}\,(9\phi_{ij} - \phi_{ij+1}) \tag{5-26}$$

Equations (5-22) through (5-24) imply that the shear work terms adjacent to DE are also zero:

$$\left[\frac{\mu}{Re}\,(\partial u/\partial y + \partial v/\partial x)u\right]_{y-} = 0 \tag{5-27}$$

$$\left[\frac{\mu}{Re}\left(\frac{4}{3}\,\partial v/\partial y - \frac{2}{3}\,\partial u/\partial x\right)v\right]_{y-} = 0 \qquad (5\text{-}28)$$

5.4 Outflow Boundary

The outflow boundary, EF in Figure 3, is adjacent to the outflow cells at their x+ edges. Little can be assumed about the flow here regarding specification of gradients or variables because the flow is not known a priori. For explicit schemes, Roache[30] suggests various extrapolation methods. He notes that, in most cases, linear extrapolation is satisfactory, except perhaps when a shock crosses the boundary. Thus, an implicit, linear extrapolation procedure was used to specify conditions at the x+ edge of the outflow cell. The schemes which computed the conditions at the outflow cell points by explicit extrapolation all caused divergence for $\Delta t > \Delta t_{CFL}$. Zero gradient forms for the outflow cell points, both explicit and implicit, resulted in wiggles in the steady state solution. Details are described in the section on boundary conditions in Chapter VI.

The values of all the dependent variables at x+ are obtained by a linear extrapolation from ij and i-1,j:

$$\phi_{x+} = \frac{1}{2}\left(3\phi_{ij} - \phi_{i-1,j}\right) \qquad (5\text{-}29)$$

Thus normal derivatives at x+ are equal to the normal derivative at x-:

$$(\partial\phi/\partial x)_{x+} = (\partial\phi/\partial x)_{x-} = \frac{1}{\Delta x}\left(\phi_{ij} - \phi_{i-1,j}\right) \qquad (5\text{-}30)$$

5.5 Upper Boundary

For the upper boundary, labeled AF in Figure 3, the properties were determined explicitly (i.e., after the rest of the flow field has

been computed) by the simple wave procedure used by Allen and Cheng and outlined by Roache (Reference 30, pp. 282-283). Briefly, it was assumed that properties are constant along the straight, left-running characteristic line passing through an upper boundary point ij. This line is determined by the angle $(\mu_{in} + \theta)$, where μ_m = arc sin(1/M) is the local Mach angle ($M \geq 1$) and θ = arc tan(v/u) is the local flow direction. The properties on the characteristic line are determined by linear interpolation between (i-1, j-1) and (i,j-1) or (i-1,j-1) and (i-1,j) depending on the local ($\mu m + \theta$) and the ratio $\Delta y/\Delta x$. Figure 6, shows the two cases.

For $\tan (\mu_m + \theta)_{i-1,j-1} > \Delta y/\Delta x$, the characteristic line runs between (i-1,j-1) and (i,j-1), and the properties at P are determined by:

$$\phi_p = \phi_{i-1,j-1} + (\frac{\ell}{\Delta x})(\phi_{i,j-1} - \phi_{i-1,j-1}) \qquad (5\text{-}31)$$

Then $\phi_{ij} = \phi_p$ is used to solve for the upper boundary points. The value of ℓ and thus the location of P are determined as follows. Consider the quantity

$$\omega = \tan [90° - (\mu_m + \theta)]$$

By geometry:

$$\omega_p = \frac{\Delta x - \ell}{\Delta y} \qquad (5\text{-}32)$$

But from (5-40)

$$\omega_p = \omega_{i-1,j-1} + (\frac{\ell}{\Delta x})(\omega_{i,j-1} - \omega_{i-1,j-1}) \qquad (5\text{-}33)$$

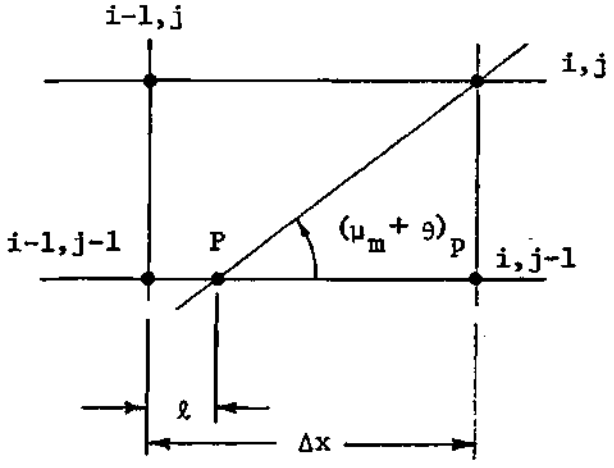

$\tan(\mu_m + \theta)_p > \Delta y/\Delta x$

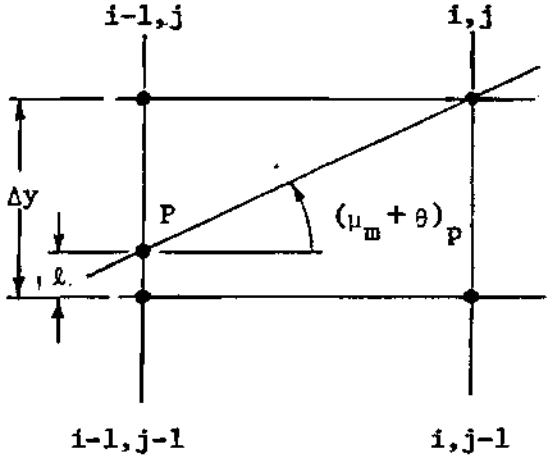

$\tan(\mu_m + \theta)_{i-1,j-1} < \Delta y/\Delta x$

Figure 6. Boundary Cells - Upper Boundary.

Equating (5-41) to (5-42) and solving for gives.

$$\ell = \frac{(\Delta x/\Delta y - \omega_{i-1,j-1})}{\frac{1}{\Delta x}(\omega_{i,j-1} - \omega_{i-1,j-1}) + \frac{1}{\Delta y}} \tag{5-34}$$

For the case of $\tan(\mu_m + \theta) < \frac{\Delta y}{\Delta x}$, the characteristic line runs between (i-1,j-1) and (i-1,j). The properties at p are determined by

$$\phi_p = \phi_{i-1,j-1} + \frac{\ell}{\Delta y}(\phi_{i-1,j} - \phi_{i-1,j-1}) \tag{5-35}$$

and then $\phi_{ij} = \phi_p$ as before. Here the quantity $\omega = \tan(\mu_m + \theta)$ is used and

$$\omega_p = \frac{\Delta y - \ell}{\Delta x} \tag{5-36}$$

is equated with

$$\omega_p = \omega_{i-1,j-1} + \frac{\ell}{\Delta y}(\omega_{i-1j} - \omega_{i-1,j-1}) \tag{5-37}$$

to get

$$\ell = \frac{(\Delta y/\Delta x - \omega_{i-1,j-1})}{\frac{1}{\Delta y}(\omega_{i-1,j} - \omega_{i-1,j-1}) + \frac{1}{\Delta x}} \tag{5-38}$$

5.6 Inflow Boundary

The flow properties on the inflow boundary (AB in Figure 3) were held fixed during the computation. Their values were chosen starting with the assumed velocity profile used by Allen and Cheng.

$$\begin{aligned} u &= \frac{1}{9}(2\eta^7 - 7\eta^4 + 14\eta) \qquad 0 \leq \eta \leq 1 \\ u &= 1 \qquad\qquad\qquad\qquad\quad \eta > 1 \end{aligned} \tag{5-39}$$

where $\eta = y/\delta$

δ = nondimensional boundary layer height

The internal energy profile was determined from the Busemaun integral of the compressible laminar boundary-layer energy equation for an adiabatic wall:

$$e = 1 + \frac{1}{2}(\gamma - 1)M_1^2(1 - u^2) \tag{5-40}$$

with the assumption of constant pressure through the inflow boundary layer, the density is determined from the equation of state. Here

$$\rho = \frac{1}{e} \tag{5-41}$$

With these values fixed the vertical velocity component is determined from the boundary layer equations. As in Allen and Cheng, an ordinary differential equation for v can be derived by combining the x-momentum and continuity equations and using the energy integral. Integrating both sides gives:

$$v(\eta) = -\frac{u}{Re\delta}\int_o^\eta \frac{1}{u^2}\left[1 + \frac{1}{2}(\gamma-1)M_1^2(1+u^2)\right]\frac{d^2u}{d\eta^2}\,d\eta \quad 0 < \eta \leq 1$$

$$v(\eta) = v(1) \qquad \eta > 1 \tag{5-42}$$

where $\eta = y/\delta$ $\quad \delta = .41$

5.7 Initial Conditions

The unsteady equations require that initial conditions be specified everywhere before computation can begin. This specification is

arbitrary but some care must be taken. Initial conditions with very steep gradients near the expansion corner, for example, were found to cause divergence. An examination of the effect of a few different initial conditions is discussed in Section 6.3-4. For the development of the procedure and for most of the computations the same initial conditions were used. The boundary layer and freestream conditions were imposed along the upper wall to corner point C. Beyond this corner and above it, the freestream conditions were applied but with $v = 0$. Below the expansion corner v was zero also and u was 30% of the freestream value. The parameters of the flow were set to correspond to Allen and Cheng's Case B1, where the freestream Mach number was 3, the Reynolds number was 550, the nondimensional boundary layer height was 0.41, and the walls were adiabatic. This also corresponds to Allen's cases C1 and C5.

CHAPTER VI

RESULTS

This chapter is divided into three parts. The first part discusses the various finite difference schemes tried for the boundary conditions and the reasons for the final choices. The second part gives the results of the flow field computations and the comparison with the results obtained by Allen and Cheng. The last part discusses the results of some numerical tests on the method, especially the use of a finer grid, larger time steps, and different initial conditions.

6.1 Boundary Conditions

Like the finite difference schemes, the boundary conditions can be either explicit or implicit. For an overall implicit procedure, it is desirable to have implicit boundary conditions to prevent problems associated with time lagging of the boundary conditions behind the flow field. For time steps much larger than the explicit stability limit, the use of explicit forms on some boundaries may not be possible. Additionally, the use of implicit boundary conditions may accelerate convergence, a very desirable feature. When the term "implicit" is applied to any of the forms to be described below, it means that the form was incorporated into the block tridiagonal matrix and the variables at the boundary solved along with those on the interior. "Explicit" refers to those schemes which compute the boundary variables after those at interior points have been computed.

As stated in the previous chapter, boundary conditions can not be treated haphazardly. Care must be taken in the selection, from the many forms possible, to prevent "wiggles" or even divergence. Several of these forms are discussed in the following sections but some preliminary comments about wiggles are appropriate.

Wiggles are nonphysical spatial oscillations occurring in the solution. Roache points out that wiggles are not usually caused by iterative instability, nonlinearities, or spatially varying coefficients, but are actually the solution of the finite difference equations. Moretti gives several examples where the appearance of wiggles was caused by poor modeling of the physical behavior (or, in some cases, no modeling at all), particularly poor treatment of the boundary conditions.

Standard techniques for treating procedures which produce wiggles are the use of artificial viscosity or switching from central differencing to upwind differencing. Roache, however, shows that the two are roughly equivalent, the truncation error of upwind differencing corresponding to an artificial viscosity. Use of upwind differencing can become complicated in regions where the flow direction is not known beforehand, as in a recirculation region. Further, artificial viscosity may tend to smooth important flow features over too large an area or even change the flow problem. Moretti,[32] for example, shows that artificial viscosity completely wipes out a shock in a Laval nozzle and causes the procedure to be significantly in error for the critical throat conditions.

Because of the foregoing, the assumption was made that appropriate

forms for the boundary conditions could be found without having to abandon central differencing or having to apply artificial viscosity. This proved to be the case. Indeed, all nonphysical behavior of preliminary solutions came from ill treatment of one or more of the boundary conditions. (Many times a programming error connected with the boundaries was responsible. A considerable amount of time was required to completely "debug" the program, due largely to the complexity of the equations).

As mentioned before, a great advantage in the cell integration technique is the conceptual aid afforded in specifying boundary conditions. When fluxes are required to be zero, for example, it is clear which terms should be eliminated from the finite difference equations so that enforcement is automatic. Ambiguity arises when a dependent variable or its derivatives are not specified on the boundary by physical conditions (such as wall pressure). Then, one of the many extrapolation or one-sided forms must be chosen. As stated in Chapter V, much effort was required to determine which forms were stable, consistent, and accurate. This section summarizes that effort.

6.1-1 Wall Boundaries

Surprisingly, the solution was insensitive to many of the differing forms for conditions at the walls. Whenever a problem occurred, it was either a programming error or a problem on some other boundary. This was perhaps a result of no slip and impermeability being strictly enfroced. These are the dominant conditions that characterize the wall.

Most of the forms used on the wall were those used by Allen and

Cheng,[24] although many other forms were tried attempting to get rid of wiggles in the solution near the back wall. It was discovered, however, that these wiggles were a result of poor downstream boundary treatment (see Section 6.1-3) and the Allen and Cheng forms appeared to work best. The different forms used seemed to have little effect on the solution although second-order forms gave more physically correct answers than first order forms, as is explained next.

Since the walls are impermeable, there is no mass, momentum, or energy flux across a cell boundary coinciding with a wall. Hence, the contribution to the convection term from the cell edge is zero, leaving a first order, one-sided difference for the flux derivative. For example, consider the finite difference form for a flux term of a cell ij

$$(\partial \rho u\phi/\partial x)_{ij} = \frac{1}{\Delta x}\,(\rho u\phi_{x+} - \rho u\phi_{x-}) \qquad \phi = \begin{vmatrix} 1 & \text{mass} \\ u & \text{x-mom.} \\ y & \text{y-mom.} \\ e & \text{energy} \end{vmatrix} \tag{6-1}$$

For a wall at x-, (i.e., ij is next to the back wall) $(\rho u\phi)_{x-} = 0$ and

$$(\partial \rho u\phi/\partial x) = \frac{1}{\Delta x}\,(\rho u\phi_{x+} - 0) = \frac{1}{2\Delta x}\,[(\rho u\phi)_{i\omega,j} + (\rho u\phi)_{i\omega+1,j}] \tag{6-2}$$

When this form was used the zero streamline extended from the rear stagnation point forward to another point on the centerline. The expected behavior, and that obtained by Allen, Allen and Cheng, and Kronzon, et al., was for the zero streamline to extend forward from the rear stagnation point to a point on the back wall just below the expansion

corner. The reason for the unexpected streamline behavior can be seen in the velocity vector plot in Figure 7. As will be explained again in Section 6.2, the plot shows total velocity magnitudes and directions (with the arrow heads a constant size) for each point in the coarse mesh field. The zero streamline intersects the centerline near point D instead of on the wall near C because all the velocities in the column nearest the back wall are positive, when most, starting at the point nearest D should have been negative. That equation (6-2) was the problem can be seen by considering a typical flux term for a cell adjacent to the back wall.

$$\frac{\partial}{\partial x}(\rho u\phi)_{ij} = \frac{1}{\Delta x}\left[(\rho u\phi)_{x+} - (\rho u\phi)_{x-}\right]$$

$$= \frac{1}{\Delta x}(\rho u\phi)_{x+} \qquad \phi = \begin{vmatrix} 1 \\ u \\ y \\ e \end{vmatrix} \qquad (6\text{-}3)$$

since

$$(\rho u\phi)_{x-} = (\rho u\phi)_{wall} = 0$$

Using equation (6-2) for $(\rho u\phi)_{x+}$ assumes a linear variation in the flux across the cell. Thus

$$\rho u\phi = c_1 x = \frac{1}{2}(\rho u\phi_{i+1j} + \rho u\phi_{ij})x \qquad (6\text{-}4)$$

where x = distance from the wall.

This means that

$$\frac{\partial}{\partial x}(\rho u\phi) = c_1 = \frac{1}{2}(\rho u\phi_{i+1j} + \rho u\phi_{ij}) \qquad (6\text{-}5)$$

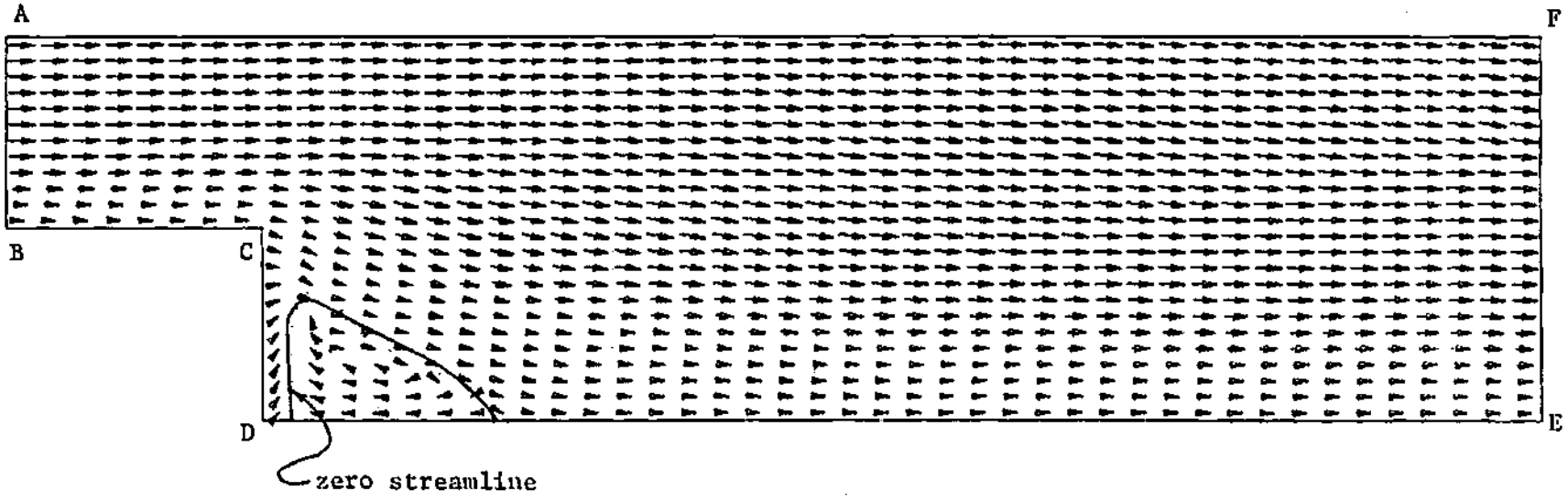

Figure 7. Velocity Vectors for First-Order Backwall Flux Differencing.

for the whole cell from the wall to x+. From the steady-state continuity equation, evaluated at the wall

$$\left(\frac{\partial \rho u}{\partial x}\right)_w + \left(\frac{\partial \rho v}{\partial y}\right)_w = 0 \qquad (6\text{-}6)$$

but

$$\left(\frac{\partial \rho v}{\partial y}\right)_w = 0$$

since $\rho v = 0$ all along the wall. So

$$\left(\frac{\partial \rho u}{\partial x}\right)_w = 0 \qquad (6\text{-}7)$$

Now

$$\frac{\partial \rho u \phi}{\partial x} = \rho u \frac{\partial \phi}{\partial x} + \phi \frac{\partial \rho u}{\partial x} \qquad (6\text{-}8)$$

Evaluating equation (6-8) at the wall gives

$$\left(\frac{\partial \rho u \phi}{\partial x}\right)_w = 0 \qquad (6\text{-}9)$$

since $(u)_w = 0$ and $\left(\frac{\partial \rho u}{\partial x}\right)_w = 0$. But this implies that

$$c_1 = \frac{1}{2} \left(\rho u \phi_{i+1j} + \rho u \phi_{ij}\right) = 0 \qquad (6\text{-}10)$$

and

$$\rho u \phi_{i+1j} = - \rho u \phi_{ij} \qquad (6\text{-}11)$$

Since velocities are small near the lower part of the back wall, the

dominant flux terms are those for $\phi = 1$ and $\phi = e$, the mass and energy fluxes. Therefore, since ρ, 1, and e are all positive, u is required to change sign between (i,j) and (i+1,j). Thus u was positive for the column nearest the wall and negative in the next for the cells in the recirculation region. Negative u was expected in both. Further, the fact that $\rho u\phi$ changes sign between (i,j) and (i+1,j), having been zero at the x-edge of (i,j), implies at least quadratic behavior in violation of the linear assumption of equation (6-2).

Allen and Cheng encountered negative densities on the upper part of the back wall near the expansion corner when they used equation (6-2) and fine grid spacing. Equation (6-11) may explain this behavior. In this region, u is not small so that for $\phi = u$, equation (6-11) implies

$$(\rho u^2)_{ij} = -(\rho u^2)_{i+1j}$$

which may explain why negative densities were encountered. It has already been shown that the assumption of a linear variation in $\rho u\phi$ leads to a violation of that assumption and some physically unrealistic results. Equation (6-9) and the fact that $\rho u\phi = 0$ at the wall imply at least a quadratic variation in the flux across the cell. Allen and Cheng suggested a second-degree polynomial through the two cell centers nearest the wall, and used the known value of $u = 0$ at the wall to get an expression for the flux at x+:

$$(\rho u\phi)_{x+} = \frac{1}{3}\left[(\rho u\phi)_{i\omega+1,j} + 3(\rho u\phi)_{i\omega,j}\right] \qquad (6\text{-}12)$$

This gives

$$(\partial \rho u \phi / \partial x)_{i\omega,j} = \frac{1}{3\Delta x} \left[(\rho u \phi)_{i\omega+1,j} + 3(\rho u \phi)_{i\omega,j} \right] \tag{6-13}$$

This form gave the correct behavior for the cells adjacent to the back wall in the present calculations.

The pressure at the wall is unknown. Allen and Cheng suggested a linear extrapolation from the two nearest cells:

$$(\rho e)_{\omega} = \frac{1}{2} \left[3(\rho e)_{i\omega,j} - (\rho e)_{i\omega+1,j} \right] \tag{6-14}$$

This form was used initially on the back wall and its equivalent form was used on the upper wall.

Two other forms were tried. Allen and Cheng's results showed that the pressure gradient normal to the back wall is very small. Thus, the other two forms tried for the wall pressure involved a zero pressure gradient. The first form is the simple

$$(\rho e)_{\omega} = (\rho e)_{i\omega,j} \tag{6-15}$$

The second form makes use of the second-order, one-sided form (equation (5-21))

$$(\rho e)_{\omega} = \frac{1}{8} \left[9(\rho e)_{i\omega,j} - (\rho e)_{i\omega+1,j} \right] \tag{6-16}$$

Experience with calculations on all the boundaries indicates that a second-order form is superior to a first-order form in that the results are usually more physically realistic and more consistent with the basic finite difference method. Indeed, when equation (6-2) was used for the flux terms, equation (6-16) tended to bring the zero streamline off the

centerline and back to the back wall. Equations (6-14) and (6-15), on the other hand, resulted in little change. When equation (6-12) was used for the flux terms, there was little difference in the solution with any of the wall pressure forms. Thus, for some conditions equation (6-16) gave better physical results and was the form used for the back wall pressure.

Four forms were tried for the viscous terms involving cross-derivatives. None of these forms appeared to be preferred. Most, in fact, gave identical answers to several decimal places. There are two types of cross-derivatives. Considering the upper wall, the first form is

$$\frac{\partial}{\partial y}\left(\xi \frac{\partial \phi}{\partial x}\right)_{ij} \quad \text{where } \phi = \begin{Bmatrix} u \\ v \end{Bmatrix}, \quad \xi = \begin{cases} \mu/\mathrm{Re} \text{ momentum eqns.} \\ (\mu/\mathrm{Re})\phi \text{ energy eqn.} \end{cases} \tag{6-17}$$

Applying cell integration this becomes

$$\frac{1}{\Delta y}\left[\left(\xi \frac{\partial \phi}{\partial x}\right)_{y+} - \left(\xi \frac{\partial \phi}{\partial x}\right)_{y-}\right] = \frac{1}{\Delta y}\left[\left(\xi \frac{\partial \phi}{\partial x}\right)_{y+}\right] \tag{6-18}$$

since

$$\left(\frac{\partial \phi}{\partial x}\right)_{y-} = \left(\frac{\partial \phi}{\partial x}\right)_{w} = 0$$

Two forms for equation (6-18) are:

$$\frac{1}{\Delta y}\left(\xi \frac{\partial \phi}{\partial x}\right)_{y+} = \frac{1}{\Delta y}(\xi)_{y+}\left(\frac{\partial \phi}{\partial x}\right)_{y+} = \frac{1}{\Delta y}\left[\left(\frac{\xi_{i,j+1} + \xi_{ij}}{2}\right)\left(\frac{\phi_{i+1,j+1} + \phi_{i+1,j} - \phi_{i-1,j+1} - \phi_{i-1,j}}{4\Delta x}\right)\right] \tag{6-19}$$

$$\frac{1}{\Delta y}\left(\xi \frac{\partial \phi}{\partial x}\right)_{y+} = \frac{1}{\Delta y} \cdot \frac{1}{2}\left[\xi_{ij+1}\left(\frac{\phi_{i+1,j+1} - \phi_{i-1,j+1}}{2\Delta x}\right) + \xi_{ij}\left(\frac{\phi_{i+1j} - \phi_{i-1j}}{2\Delta x}\right)\right] \qquad (6\text{-}20)$$

The question here is whether to split $\left(\xi \frac{\partial \phi}{\partial x}\right)_{y+}$ into $(\xi)_{y+}\left(\frac{\partial \phi}{\partial x}\right)_{y+}$ or to evaluate it as a single quantity. Naturally, the use of either (6-19) or (6-20) depends on the form used for the interior points, to be consistent. Both forms were tried and the results were identical. Equation (6-20) was the final form used because the non-cross-derivative viscous terms (i.e., $\frac{\partial}{\partial y}\left(\xi \frac{\partial \phi}{\partial y}\right)$ and $\frac{\partial}{\partial x}\left(\xi \frac{\partial \phi}{\partial x}\right)$) were not split. Thus equation (6-20) is more consistent with the present method than equation (6-19).

The same question about splitting arises with the second cross-derivative type

$$\frac{\partial}{\partial x}\left(\xi \frac{\partial \phi}{\partial y}\right)_{ij} \qquad (6\text{-}21)$$

Applying the cell integration, equation (6-21) becomes

$$\frac{1}{\Delta x}\left[\left(\xi \frac{\partial \phi}{\partial y}\right)_{x+} - \left(\xi \frac{\partial \phi}{\partial y}\right)_{x-}\right] \qquad (6\text{-}22)$$

Neither term is zero here (except for the cell nearest corner point D where $\phi = v$ and when $\xi = \frac{\mu}{Re} v$), but whether they are split or not, they need to be evaluated. Since the velocity on the wall is zero, the question arises (as in the flux terms) whether a simple form like equation (6-2) is sufficient. Here the answer is yes. Both equations (6-2) and (6-13) were tried on the back wall for these viscous cross derivatives with no detectable difference. As an example of the simple form, the

first term of equation (6-22) becomes

$$\left(\xi \frac{\partial \phi}{\partial y}\right)_{x+} = \left[\xi_{x+}\left(\frac{\phi_{y+} - \phi_{y-}}{\Delta y}\right)_{x+}\right] = \left\{\frac{1}{2}\left(\xi_{i+1j} + \xi_{ij}\right)\left[\frac{1}{4}\left(\phi_{i+1j+1} + \phi_{ij+1} + \phi_{i+1j} + \phi_{ij}\right) - 0\right]/\Delta y\right\} \tag{6-23}$$

The last modification which was tried before the actual cause of the wiggles was discovered, was to make the back wall a slip wall. This was done by making $\left(\frac{\partial v}{\partial y}\right)_{\omega}$ nonzero. The value of v on the wall was given by an extrapolation through the nearest two grid points. This slip wall tended to lower the v-component of velocity in the back wall cells near corner point C by up to 10% (though one point changed 36%), and it also increased the pressure in these cells by about 5%. Nearer the centerline and out into the rest of the flow field the effect was negligible.

All of these modifications had little effect on the wiggles, and seemed to point out the relative insensitivity of the solution to various one-sided forms at some boundaries. The greatest effect on the solution in the cells along the back wall was the difference between the flux derivatives (equations (6-12) and (6-13)). For the upper wall, the inflow conditions were important (see Section 6.1.5).

For some finite difference schemes, a point like the one nearest corner point C, where the two walls intersect, can be difficult to formulate. No real problem was encountered here as the cell-integration method made clear which terms needed to be modified. For this cell (whose indices are $i\omega, j\omega$), the x- edge was considered normal to the upper wall and the y- edge normal to the back wall.

6.1.2 Centerline

Initially, all of the finite difference forms used for the centerline were derived in a similar manner as those on the wall boundaries. Oscillations of period $2\Delta y$ (better known as wiggles) appeared in the solution for density (and pressure) normal to the centerline and extended some distance into the flow field. Kothari and Anderson,[33] solved the Navier-Stokes equations for the nonreacting case of the near field of a chemical laser. Their solutions of the supersonic flow between the centerlines of two adjacent nozzles had wiggles normal to the centerlines. They cited central differencing as the cause of the wiggles. Central differencing was definitely not the problem here, but rather treatment of the normal derivative. Consider

$$\left(\frac{\partial \phi}{\partial y}\right)_{y-} = \left(\frac{\partial \phi}{\partial y}\right)_{\text{C}_\text{L}} = 0 \qquad \phi \neq v \tag{6-24}$$

For $\left(\frac{\partial \phi}{\partial y}\right)_{ij} = \frac{1}{\Delta y}\left(\phi_{y+} - \phi_{y-}\right)$, ϕ_{y-} is zero for all the flux terms because $v = 0$ on the centerline. But for $\phi = \rho e = p$, an expression is needed. Initially, the simple first-order expression

$$(\rho e)_{y-} = (\rho e)_{ij} \tag{6-25}$$

was used. This resulted in the wiggles. When equation (6-25) was replaced by the second-order expression

$$(\rho e)_{y-} = \frac{1}{9}\left[8(\rho e)_{ij} - (\rho e)_{ij+1}\right] \tag{6-26}$$

similar to equation (6-16), the solution became smooth. The nonzero normal derivative, $(\partial v/\partial y)_{y-}$, was based on the second order form from

equation (5-9):

$$(\partial v/\partial y)_{y-} = \frac{1}{3\Delta y}\left[9(v)_{ij} - (v)_{ij+1}\right] \qquad (6\text{-}27)$$

6.1.3 Downstream Boundary

The conditions at the downstream boundary, $\phi_{ii,j}$, are not known before hand, hence some sort of extrapolation is normally employed. The extrapolation can either be explicit or implicit. Several schemes of each were tried.

Explicit forms are applied after the interior points have been computed and are lagging the solution. The linear form

$$\phi_{ii,j} = 2\phi_{ii-1,j} - \phi_{ii-2,j} \qquad (6\text{-}28)$$

where ii = downstream column cell index, caused no problems for the time step $\Delta t = \Delta t_{CFL}$, but the quadratic form

$$\phi_{ii,j} = 3\phi_{ii-1,j} - 3\phi_{ii-2,j} + \phi_{ii-3,j} \qquad (6\text{-}29)$$

resulted in diverging spatial oscillations.

When Δt was increased, equation (6-28) resulted in divergence at the downstream boundary, apparently due to lagging. An explicit zero gradient expression

$$\phi_{ii,j} = \frac{1}{3}\left[4\phi_{ii-1,j} - \phi_{ii-2,j}\right] \qquad (6\text{-}30)$$

was tried with $\Delta t = 4\ \Delta t_{CFL}$. Equation (6-30) was obtained by fitting a quadratic through (ii-2,j), (ii-1,j), and requiring that $(\frac{\partial \phi}{\partial x})_{ii,j} = 0$.

Convergent solutions were obtained but it was later discovered that wiggles in ρ, e, and p were created at the downstream boundary as soon as the shock began to cross it. These wiggles then proceeded to travel upstream and increase in amplitude near the back wall, and then decrease to small amplitude at the downstream boundary. This rather unusual sequence is shown clearly in the 3-dimensional plots in Figure 8. This figure shows the pressure as a surface at six different time steps. The initial pressure was constant everywhere, as shown in Figure 8(a). (The wall is represented by the zero values in each plot.) At first (Figure 8(b)) the pressure quickly dropped in the back wall region while the downstream pressure remained near its initial value. This resulted in a recompression wave that travelled downstream to become the shock. While the wave intersects the upper boundary (Figures 8(b) and 8(c)), the pressure appears relatively smooth except for the inflow region (see Section 6.1.5). As the wave moves to the downstream boundary (Figure 8(d)), the wiggles form normal to the downstream boundary. As previously mentioned, the wiggles then travel upstream to the back wall and inflow regions and reduce in amplitude near the downstream boundary. Notice the inflow pattern change (Figures 8(e) and 8(f)).

The fact that the wiggles occurred normal to the boundary is typical. Moretti[32] points out that wiggles form in the direction along which there is an inconsistency. Indeed, treatment of any boundary involves modification of terms normal to it. Hence poor treatment there can cause wiggles which are normal to the boundary. This also occurred on the centerline.

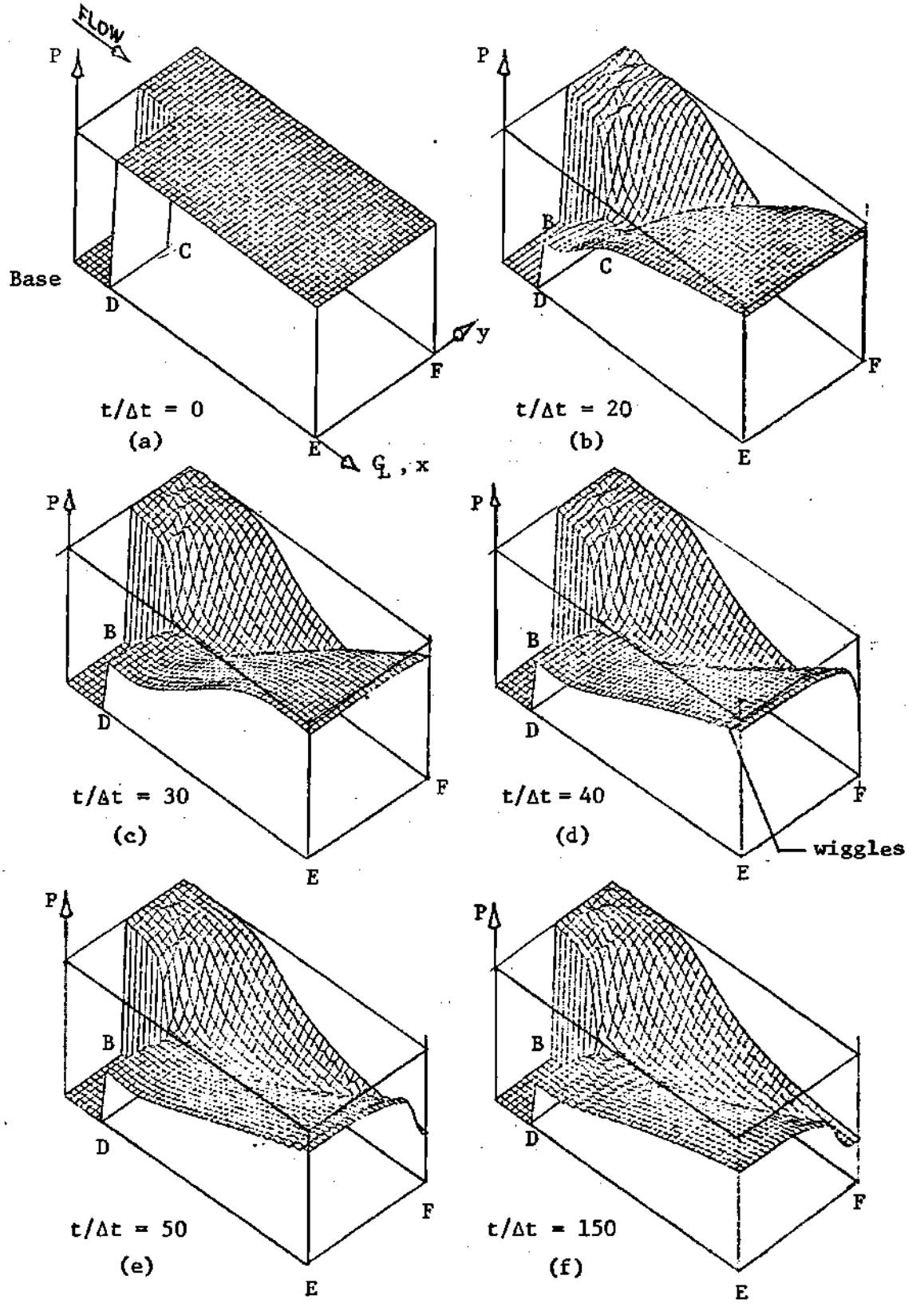

Figure 8. Development of Pressure with Time for $\partial\phi/\partial x = 0$ at Outflow Boundary.

When this was discovered, two implicit schemes were tried. The first used the simple first-order algebraic form

$$\phi_{ii,j} = \phi_{ii-1,j} \tag{6-31}$$

This form resulted in wiggles also.

The second implicit scheme specified the value at the x+ edge of a downstream boundary cell by the linear extrapolation form

$$(\phi)_{x+} = \frac{1}{2}(3\phi_{ii,j} - \phi_{ii-1,j}) \tag{6-32}$$

This also requires that

$$(\frac{\partial\phi}{\partial x})_{x+} = (\frac{\partial\phi}{\partial x})_{x-} \tag{6-33}$$

with equations (6-32) and (6-33), the finite difference conservation equations can be applied for the dependent variables at (ii,j). A derivative for a downstream cell becomes, for example

$$(\frac{\partial\phi}{\partial x})_{ii,j} = \frac{1}{\Delta x}(\phi_{x+} - \phi_{x-}) = \frac{1}{\Delta x}[(\frac{3\phi_{ii,j} - \phi_{ii-1,j}}{2}) - (\frac{\phi_{ii,j} + \phi_{ii-1,j}}{2})]$$

$$= \frac{1}{\Delta x}(\phi_{ii,j} - \phi_{ii-1,j}) \tag{6-34}$$

Note that equation (6-34) corresponds to upwind differencing, so that the outflow column of points has upwind differencing. This form resulted in a smooth density and pressure variation and eliminated the wiggles. It should be noted that a higher order extrapolation could be used instead of equations (6-31) and (6-32). This would result, however, in the block coefficient matrix no longer being tridiagonal. While this

is not too difficult a task to overcome by Gauss elimination, the extra programming effort was not done here since the linear form was satisfactory.

6.1.4 Upper Boundary

The conditions at the upper boundary are not known beforehand either. However, the boundary does lie outside the regions of major viscous transport and is assumed to be nearly inviscid. Thus a simple wave condition, as described in Section 5.5, appeared to be a logical choice. Allen and Cheng[24] obtained stable and realistic results using this scheme.

While the simple wave condition as applied is an explicit procedure, it produced stable and realistic results here even for $\Delta t = 32\ \Delta t_{CFL}$. The time lagging appeared not to hinder convergence. Here, the explicit boundary condition is desirable since it is easier to apply in a computer program than an implicit form.

One other scheme was tried for the upper boundary in an investigation of the spurious compressions in the inflow region. This alternate form was similar to the implicit extrapolation scheme which worked so well for the downstream boundary (see Section 6.1.3). In this case the values at the y+ edge were specified as

$$\phi_{y+} = \frac{1}{2}\,(3\phi_{i,jj} - \phi_{i,jj-1}) \qquad (6\text{-}35)$$

This results in a derivative for the upper boundary point as

$$\left(\frac{\partial\phi}{\partial y}\right)_{i,jj} = \frac{1}{\Delta y}(\phi_{i,jj} - \phi_{i,jj-1}) \qquad (6\text{-}36)$$

This form did not work well. The pressure, internal energy, and density of the upper boundary became very small near the downstream end and the vertical velocity component became absurdly large positive. The probable cause can be seen from the form of equation (6-36). When ϕ is positive this expression is the first-order upwind difference. For ϕ negative, equation (6-36) is the downwind difference form, which has been shown to be unstable (see for example, Roache, p. 69). Near the inflow region all the dependent variables are positive. But the corner expansion causes the vertical velocity component, v, to become negative on the rest of the upper boundary. This means that equation (6-35) is stable for the short distance that v is positive and unstable for the remainder of the upper boundary. It also did not eliminate the inflow compressions.

Since the explicit simple wave procedure appeared not to cause any problem, even for large Δt, it was retained as the method for computing the row of points along the upper boundary.

6.1.5 Inflow Boundary

Initially, as discussed in Section 5.6, the inflow boundary was specified and held fixed. The conditions were derived by first assuming a u-profile and solving for internal energy by the Busemann energy integral of the compressible boundary-layer equations and density by the equation of state, assuming $\partial p/\partial y = 0$. The normal velocity component was then solved by combining the continuity and the momentum boundary-layer equations and using the energy integral.

Two u-profiles were used, corresponding to those used by Allen and Cheng.[24] The first was a linear u-profile up to the boundary layer edge (which was one third the base half height). When Allen and Cheng

used this profile they had v = 0 as required by the formula for v. The second u-profile was the polynomial

$$u(\eta) = \frac{1}{9}\,(14\eta - 7\eta^4 + 2\eta^7) \tag{6-37}$$

where $\eta = y/\delta$ and $\delta = .41$. Here, v was not zero.

When the linear u-profile was used with v = 0, a series of compressions in the inflow region caused a pressure rise of as much as 22% of the freestream value near the upper wall. By requiring the normal pressure gradient on the upper wall to be zero by using equation (6-26), this was reduced to a rise of 6%. The zero pressure gradient is unrealistic near the expansion corner, however, where v becomes 50% of u.

Allen[34] also encountered pressure rises with v = 0. The next modification, then, was an attempt to compute v at each time step. Two schemes were tried. The first used the explicit, backward, linear extrapolation scheme

$$v_{1,j} = 2v_{2,j} - v_{3,j} \tag{6-38}$$

This form caused diverging oscillations in v which fed into the other variables. The second scheme used the implicit form

$$v_{1,j} = v_{2,j} \tag{6-39}$$

This resulted in stable computations and reduced the pressure increase in the compressions to 2% of freestream. The zero pressure gradient was still applied and v continued to increase outside of the boundary layer along the inflow boundary. Because these results were non-physical,

and because the linear u-profile has an abrupt change in slope at the boundary layer edge, it was decided to use equation (6-37), which has continuous first and second derivatives at the boundary-layer edge.

Then v was computed by the quadrature of equation (5-51) and held fixed. For the inflow cells outside the boundary layer, v was equal to the value computed by equation (5-51) for $\eta = 1$. When this was applied and the normal pressure gradient condition removed, the compressions were still there and resulted in a maximum pressure rise of about 3%. Allen[34] pointed out that too few grid points in the boundary layer could result in an inaccurate representation of the large gradients in density and internal energy (and hence pressure) near the boundary-layer edge. If this were true, then a finer mesh would reduce the magnitude of the compressions. This was tried (see Section 6.2) and indeed the compressions disappeared. A single wave originating from the top of the boundary layer does exist in the fine mesh solution, but it does not have the same character as the other irregularities. It appears to be an expansion wave, since the pressure drops immediately downstream of it. As discussed in Section 6.2, this wave may be a result of the use of $\partial P/\partial y = 0$ along the inflow boundary, when, in fact, the corner expansion is being felt this far upstream of the corner.

6.2 Computational Results

In this section the results of the computational method are given and compared to those obtained by Allen and Cheng[24] and Allen.[34] The computations were made for a laminar, supersonic two-dimensional flow past a corner (see Figure 2) at $M_1 = 3$ and Re = 550 with a boundary-layer

height of 41% of the base half height. The inflow profiles were those given by Allen and Cheng and the initial conditions were those described in Section 5.7. The mesh size was $\Delta x = 1/6$ and $\Delta y = 1/12$. This was coarser than the Allen and Cheng mesh ($\Delta x = 1/9.75$ and $\Delta y = 1/19.5$) and was chosen to increase computational speed since fewer grid points were needed to retain reasonable accuracy. The check of the coarse mesh accuracy was done by using a finer mesh for comparison (see Section 6.3). The ratio $\Delta x/\Delta y = 2$ was maintained. The time step size used in this test was four times the maximum time step for stability in explicit methods, known as the Courant-Freidrichs-Lewy (CFL) time step. Stable and convergent solutions were obtained, demonstrating potentially large savings in computer time. This is discussed in more detail in Section 6.3.

Figures 9-20 give the results of the computations using the above conditions. Figure 9 shows the velocity vectors, giving both magnitude and direction. The arrowheads are all the same size so that direction can still be seen for very small velocities. The main features of the flow field can be seen, including the upper wall boundary layer along AB, the expansion and turning at corner point C, the weak shock and turning downstream, the retarded flow near the centerline DE, and the recirculating region near the back wall CD. A rear stagnation point on the centerline and the separation point below the corner are also evident. That the flow separates below the corner has been shown in experiments by Hama[35] and by Donaldson.[36] By linear interpolation to find where $v = 0$ in the column of points nearest the wall, the flow appears to separate 20-25% of the base half height, H, below the corner. The separation point obtained by Allen and Cheng was roughly 20% of H below the corner.

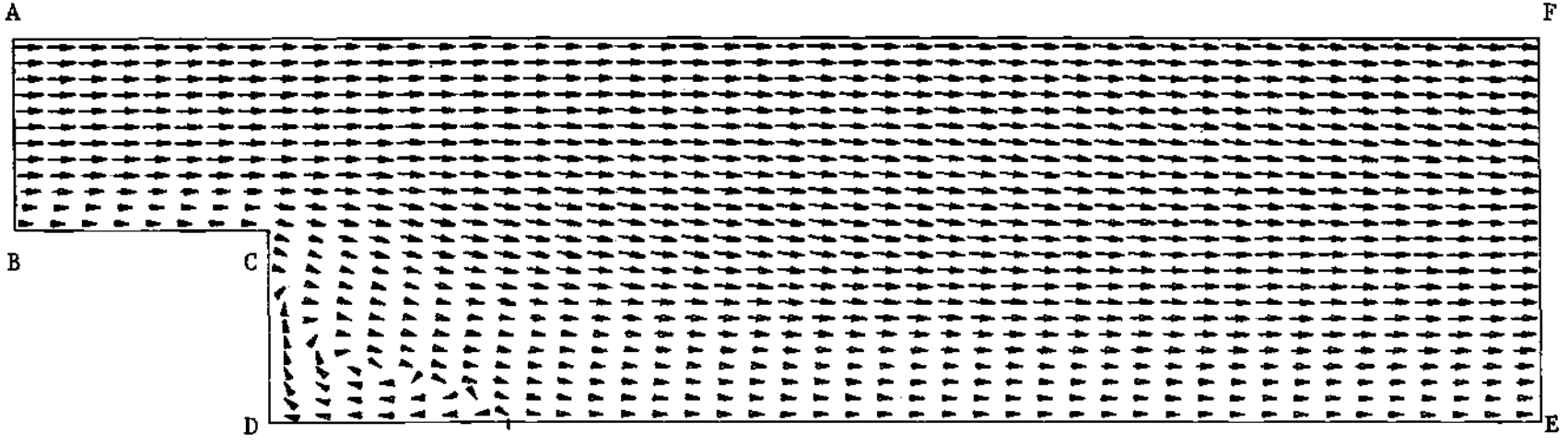

$\Delta x = 1/6$ $\Delta y = 1/12$ $M_1 = 3$

$Re = 550$ $t = 4\Delta t_{CFL}$

Figure 9. Velocity Vectors.

The rear stagnation point here was 2% closer to the wall than the one computed by Allen and Cheng.

Some of these features are more clearly shown in the streamline plot of Figure 10. Expansion and compression are shown by the spreading and converging of the streamlines. Flow direction is indicated by streamline slope (this also illustrates the inflow through AF). The recirculation region is characterized by the closed loops near the back wall and the dividing streamline (denoted by the "+" symbols) is shown extending from the back wall to the centerline.

The value of the stream function was computed at each point in the flow field by summing the mass flows vertically starting from the zero streamline BCDE. For example,

$$\psi_{ij} = \psi_{ij-1} + (\Delta y/2)[(\rho u)_{ij} + (\rho u)_{ij-1}] \qquad (6\text{-}40)$$

Maximum and minimum ψ were found to determine the range. The range was then divided into a number of incremental values. Between the minimum value of ψ and $\psi = 0$, two equally spaced values were determined. Between $\psi = 0$ and the maximum value of ψ, the increments were evenly spaced along the inflow boundary. With the array of incremental values, the plotting routine searched row by row and column by column to find where these incremental values occurred between grid points. Linear interpolation was used here to determine the variation between grid points. The location of the separation point given by the dividing streamline is not accurate for two reasons. The first is that the back wall region has been shown to be sensitive to the boundary condition treatment, thus the variables themselves are suspect. Summing over several cells adds all

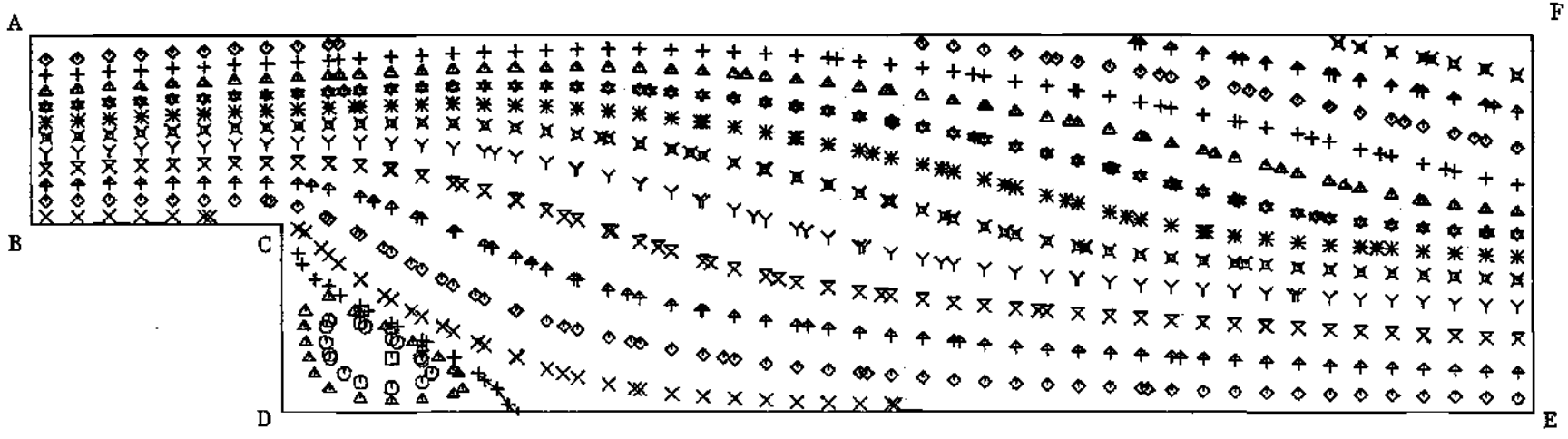

$\Delta x = 1/6$ $\Delta y = 1/12$ $M_1 = 3$

$Re = 550$ $\Delta t = 4\Delta t_{CFL}$

Figure 10. Streamlines.

the errors. Thus determination of the separation point by interpolation between velocity vectors is thought to be more accurate. Second, the location of the dividing streamline is not given at the wall but half a cell away. Since the wall is also a $\psi = 0$ line, the angle of approach is not known exactly.

The contour plots (Figures 11 through 13) were made in a similar way as the streamline plot, except that there were equal increments between maximum and minimum values. The maximum, minimum, and incremental values of the variable are pointed out above each plot with the corresponding symbols.

Figure 11 clearly shows the effect of the expansion and compression on the pressure. As expected, the pressure drops rapidly as the flow expands around the corner. Note that the expansion begins upstream of the corner. The single wiggle in the "Y" line upstream of the corner and the wiggles in the " ◇ " line at the downstream boundary appear to be caused by the coarseness of the mesh. In the fine mesh solution, these two wiggles are nearly gone. A growing region of $\partial p/\partial y \doteq 0$ near the centerline indicates the region where use of the boundary-layer equations would be a valid representation of the viscous wake. The pressure distribution across the base was relatively constant except for a sharp 50% drop near the separation point. Hama[35] made measurements of the base pressure variation for $M_1 = 4.54$ and $22 \times 10^5 < Re < 2.03 \times 10^6$ while studying the lip shock. His results show the same behavior. He found that the lip shock strength increases with Mach number and Reynolds number, but decreases with boundary layer height. This probably explains why no lip shock was observed in these calculations. The Reynolds number was only 550, the boundary-layer relatively thick, and

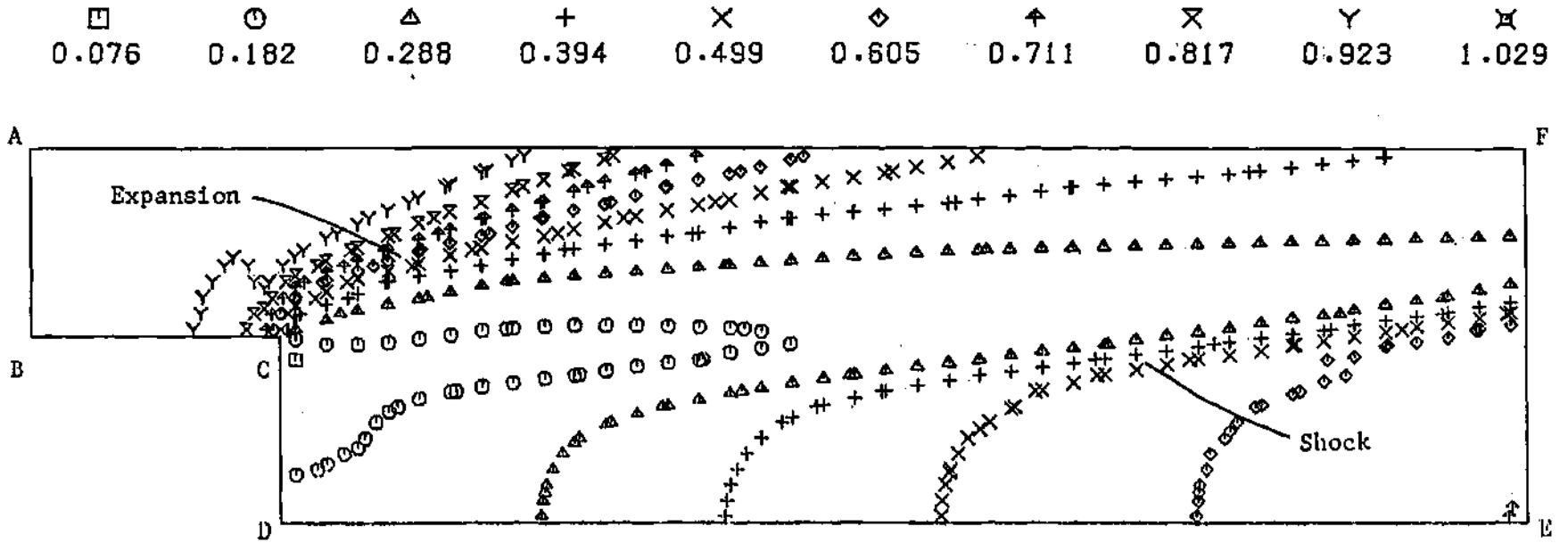

$\Delta x = 1/6$ $\Delta y = 1/12$ $M_1 = 3$

$Re = 550$ $\Delta t = 4\Delta t_{CFL}$

Figure 11. Pressure Contours.

the Mach number not particularly high.

The density contours in Figure 12 and the corresponding internal energies in Figure 13 also show the effect of expansion and compression. Near the adiabatic wall the temperature (e/c_v) is higher than the free-stream and the density shows a steep gradient in the upper part of the boundary layer. The linear nature of the contour lines for pressure (Figure 11), density, and internal energy near the upper boundary show the validity of the simple wave condition. The maximum density was within 1.5% of Allen and Cheng, the minimum within 17.0%. The maximum internal energy was within 1.0% and the minimum 1.4%.

Figure 14 compares the results for the pressure along the centerline with the results of Allen and Cheng. The agreement is very close. The Allen and Cheng line was taken directly from their results. The present results line is not actually on the centerline but $\Delta y/2$ above it. That this should be an accurate representation of the pressure on the centerline can be argued by the fact that $dp/dy = 0$ on the centerline. Hence the error is of the order of $(\Delta y)^2$ by Taylor series expansion. Also, the pressure contours show that there is little variation between the pressure on the centerline and at points nearby.

Further close agreement with the pressure computations of Allen is shown in pressure profiles in Figure 15. Here, the vertical pressure variations at several x/H locations are plotted. Once again $\partial p/\partial y$ approximately zero near the centerline is indicated. The pressure drop due to expansion is shown by the decrease in pressure from the upper part of the plot down to about $y/H = 1.0$. Then the pressure rises, more sharply as X/H increases, due to the flow turning and the formation of

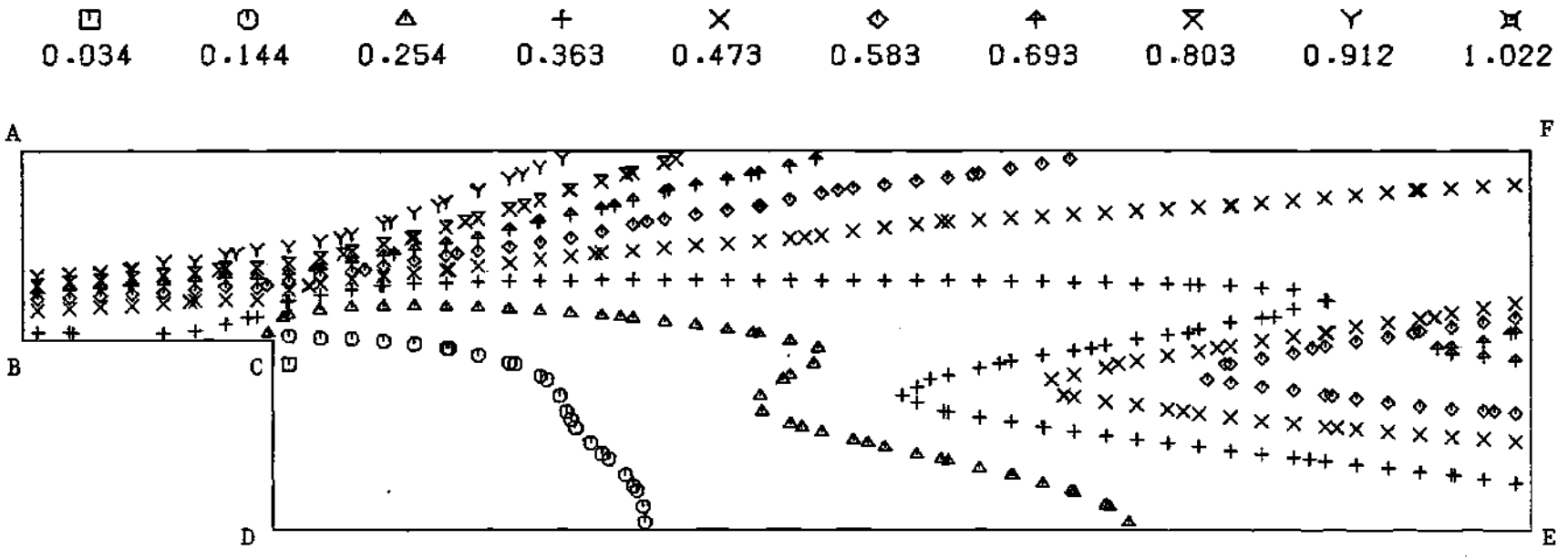

$\Delta x = 1/6$ $\Delta y = 1/12$ $M_1 = 3$

$Re = 550$ $\Delta t = 4\Delta t_{CFL}$

Figure 12. Density Contours.

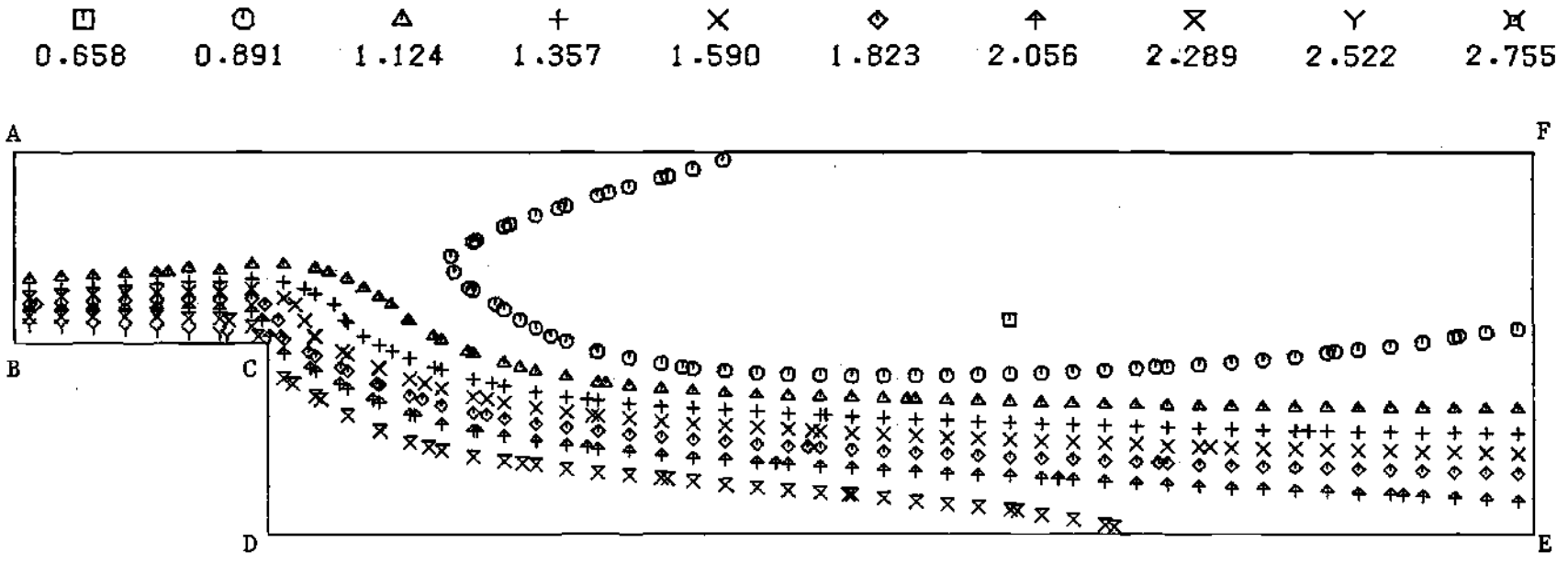

$\Delta x = 1/6$ $\Delta y = 1/12$ $M_1 = 3$

$Re = 550$ $\Delta t = 4\ \Delta t_{CFL}$

Figure 13. Internal Energy Contours.

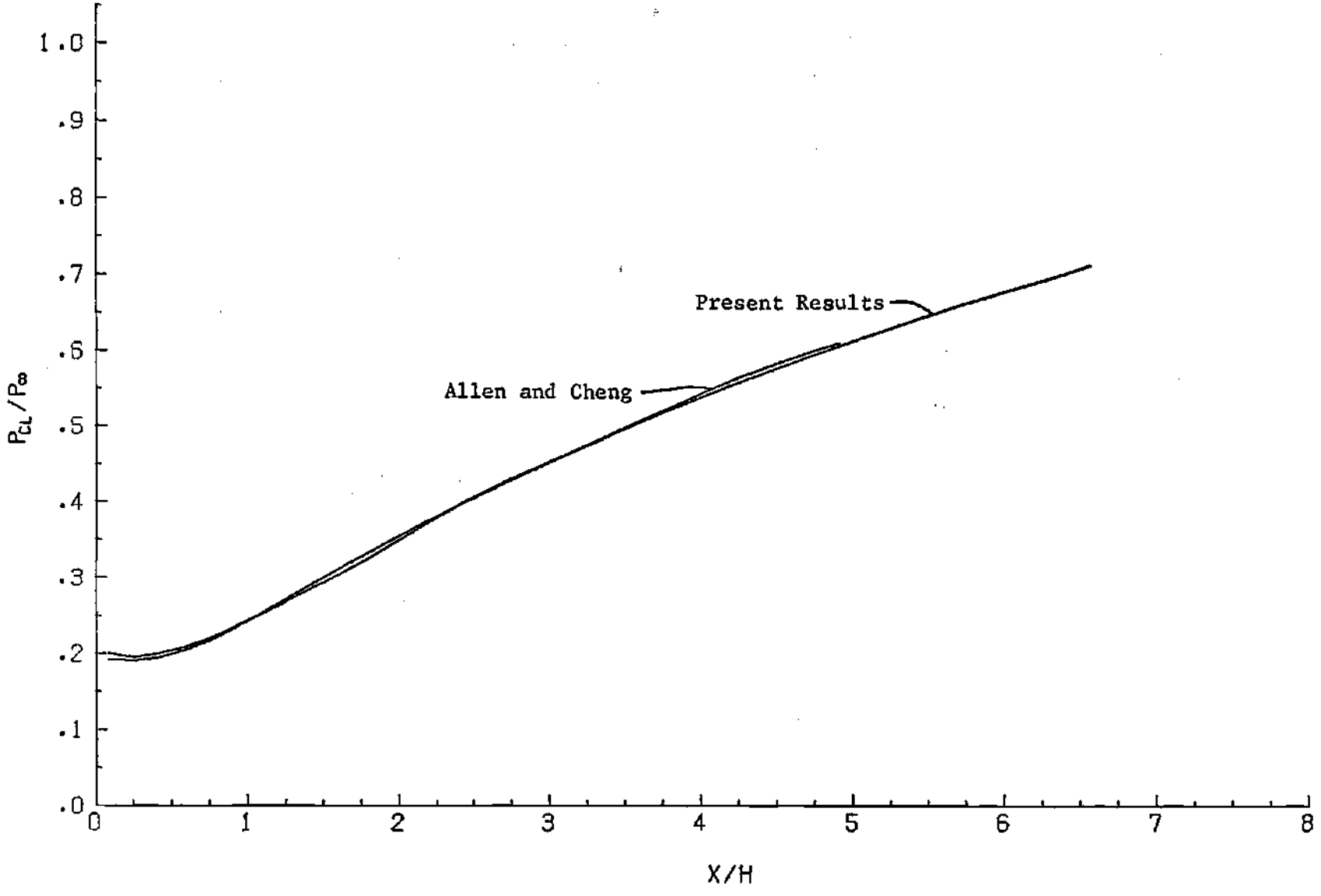

Figure 14. Centerline Pressure Distribution.

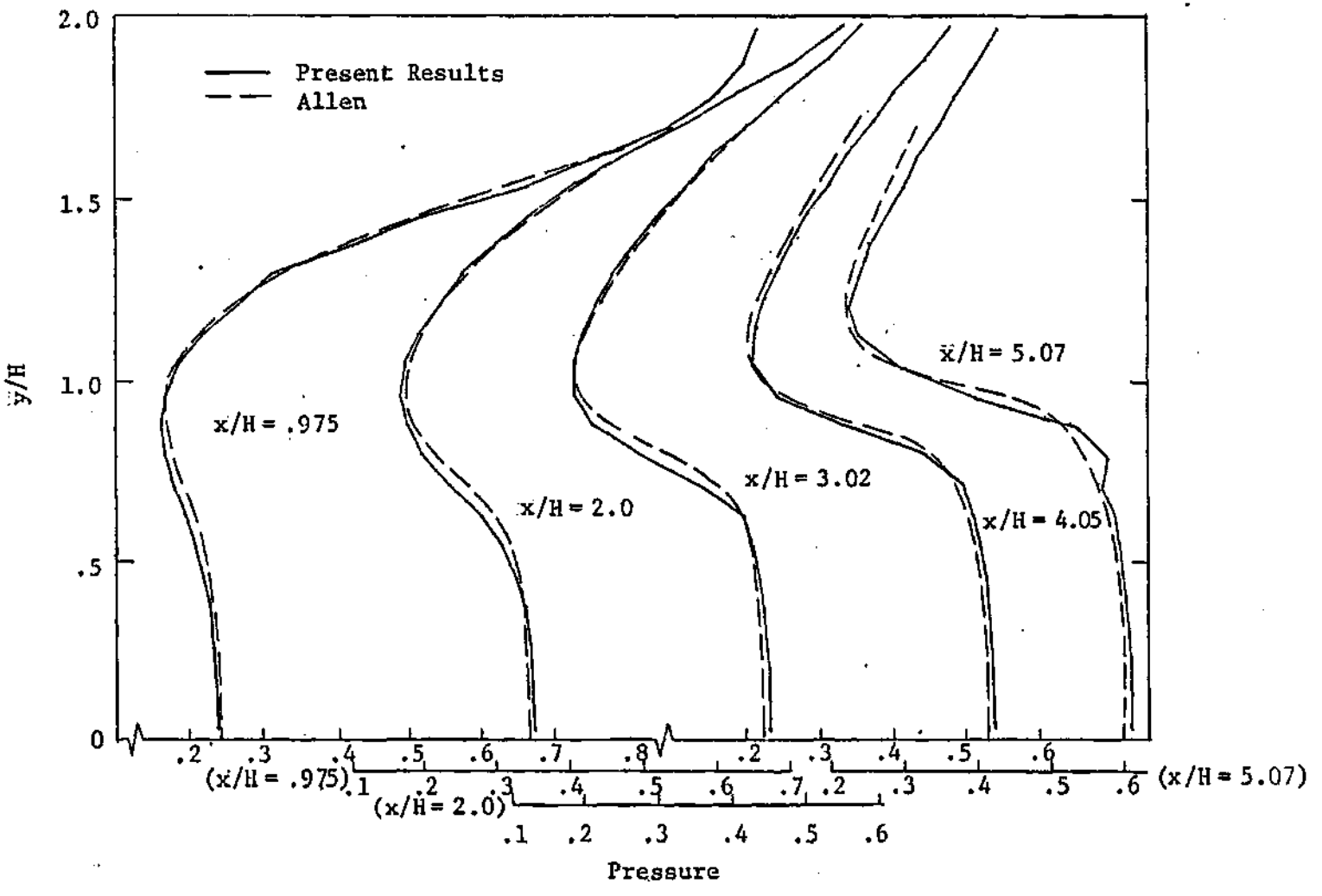

Figure 15. Pressure Profiles.

of the shock.

This behavior can be seen more clearly in the three-dimensional pressure plot of Figure 16. This shows the pressure in the entire flow field as a surface. The height in the three-dimensional plot is the pressure. The "floor" of the box around the contour is the plane defined by ABCDEF of the two dimensional flow field (see Figure 3). The values inside the wall are arbitrary, of course, since they are never used and have been set equal to zero. The inflow region is at the upper left and the outflow at the lower right (EF). The centerline DE is also shown. The points A and C are hidden. The plot is easy to generate, being a simple FORTRAN CALL in the CALCOMP plotting package.

The expansion around the corner is very clear as the contour shows a steep drop from the inflow value. The downstream development of the recompression shock as shown as the growing difference in height between the pressure near the center of the field and the region above the centerline. The extent of this difference can be seen on the vertical plane through EF.

As demonstrated in Figure 8, this type of plot can be extremely useful in visualization, not only of flow features, but of the propagation of disturbances. In Figure 16 there are a series of pressure fluctuations near the inflow and at the "crest" of the recompression wave. Those at the inflow are present from the beginning of the computation (see Figure 8), while those in the shock appear only after the shock has settled to its final position. Both appear to be caused by the coarseness of the mesh, however, since these irregularities are absent in the fine mesh solution.

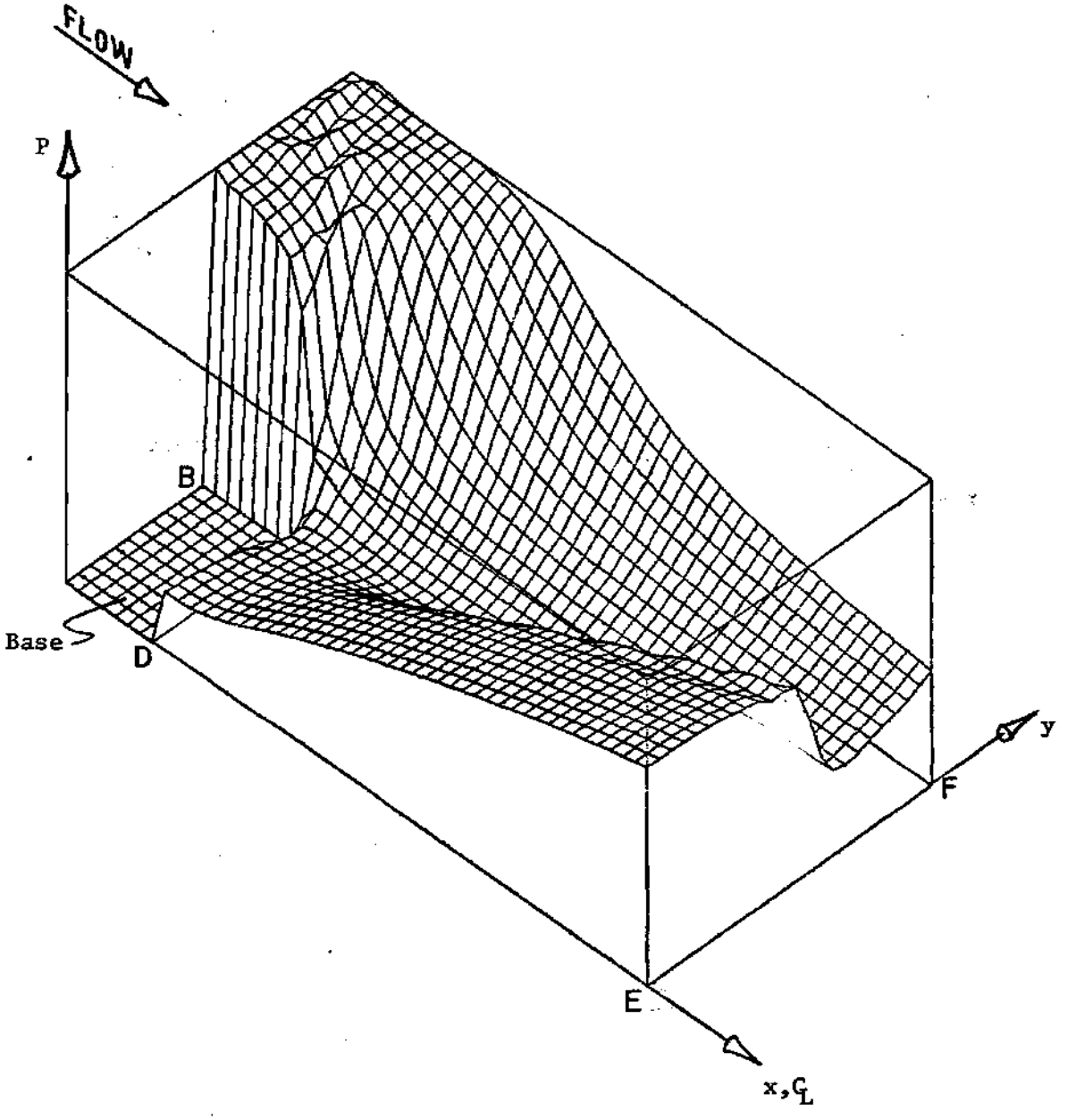

Figure 16. Pressure Surface - Coarse Mesh.

The centerline Mach number distribution is given in Figure 17. The extent of the recirculation region and the downstream acceleration are indicated. Slightly further downstream of the computation region the centerline Mach number will exceed one. The flow is already supersonic a short distance above the centerline. No singularities associated with the Mach one (sonic) condition, such as the Crocco-Lees singularity, were encountered.

The values computed here were somewhat higher than Allen's. At $x/H = 4.75$ the difference was about 6%. The reason for the higher Mach numbers on the centerline were due to the lower speeds of sound, since the temperature was lower. These lower temperatures are indicated by the lower internal energies as indicated in Figure 18. The present results for the internal energy on the centerline were typically 12-15% lower than those computed by Allen. The reason for the difference is not known, although it is presumed to be a result of the difference in the way the centerline was treated as a boundary. Allen uses the "reflection principle" rather than one-sided difference forms. He passes the centerline through the center of a cell rather than its y- edge. The centerline conditions are then enforced in a row of cells below those on the centerline by setting the dependent variables there equal to the values in the row of cells above the centerline cells. As previously stated, the centerline conditions were enforced in the present method by using appropriate one-sided forms at the cell edges adjacent to the centerline.

Away from the centerline, the internal energy comparison with

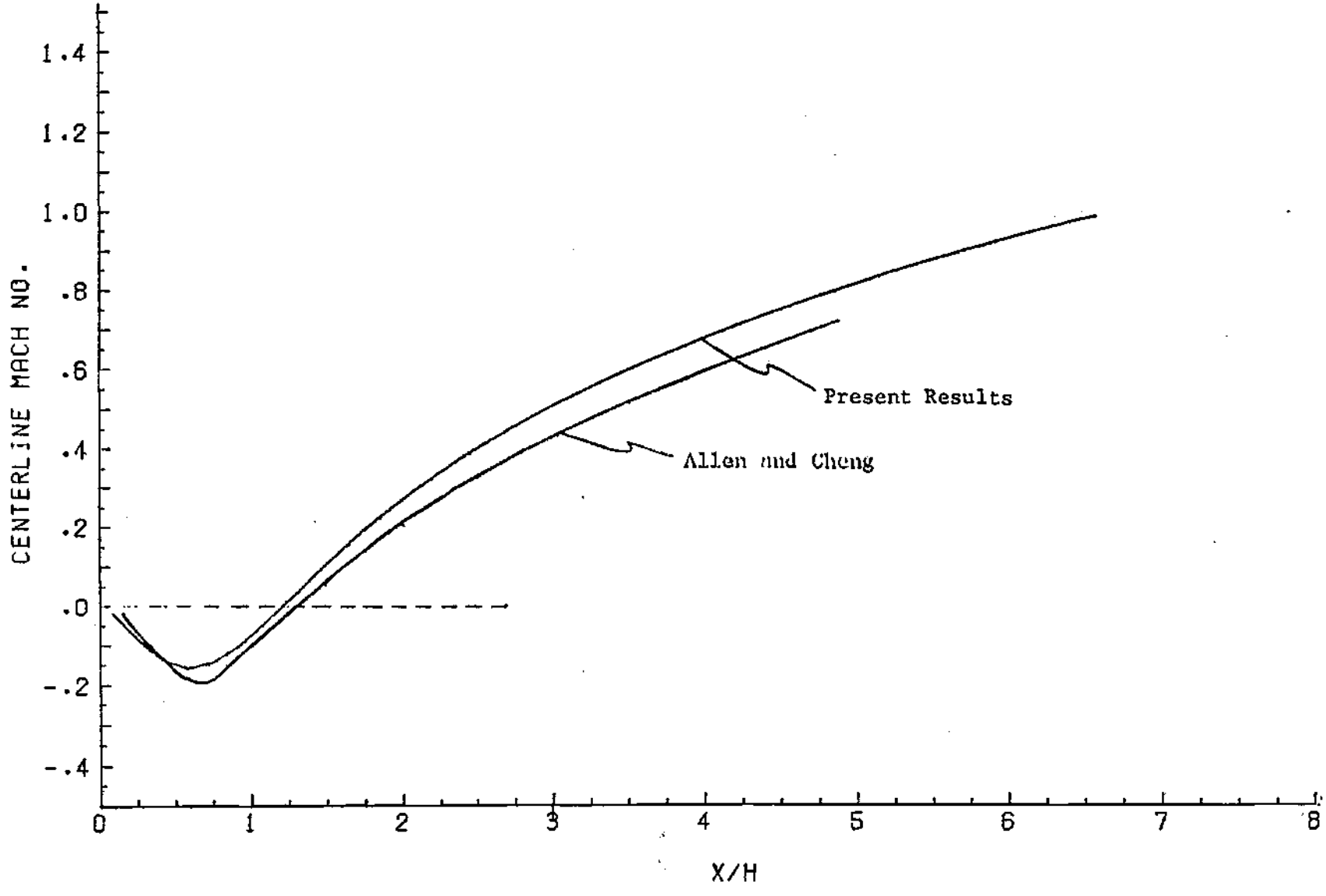

Figure 17. Centerline Mach Number Distribution.

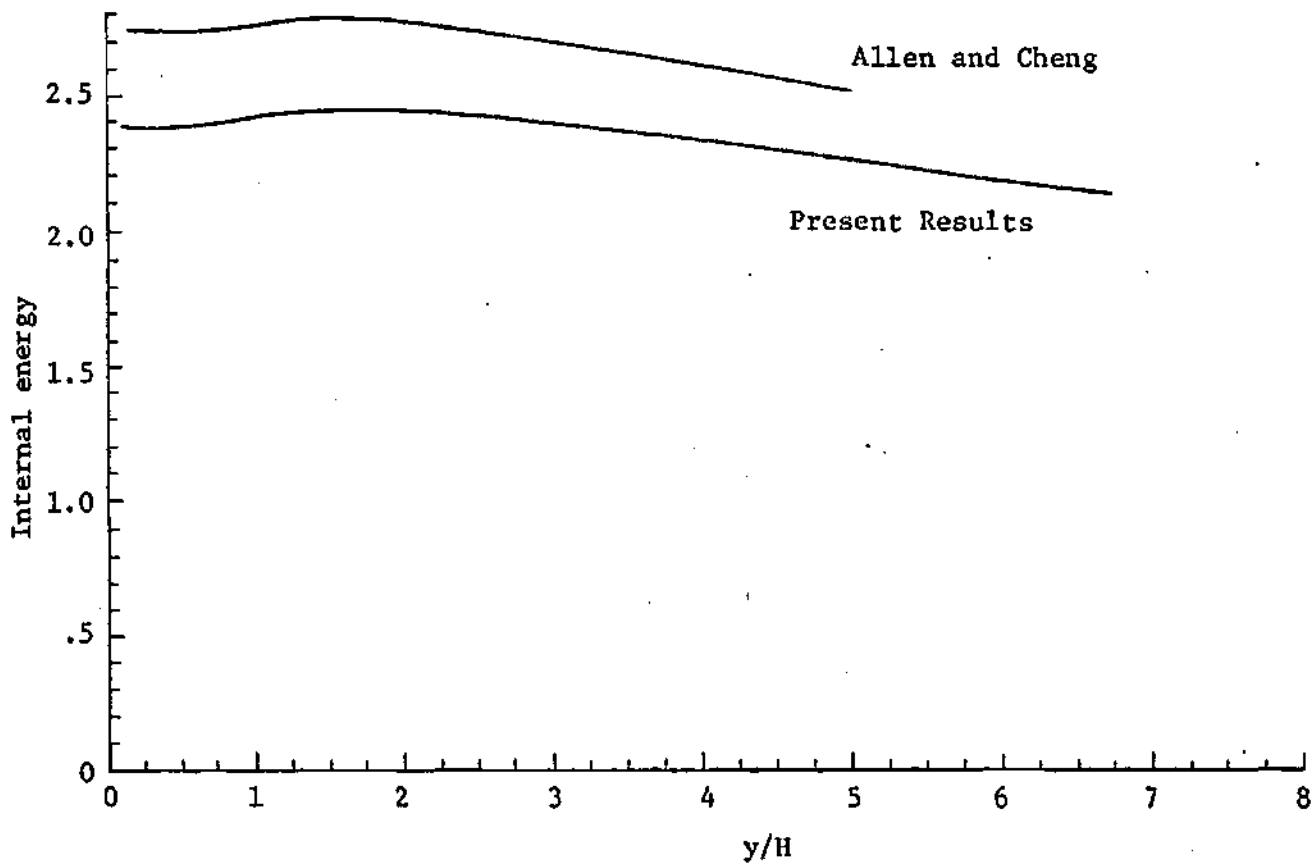

Figure 18. Centerline Internal Energy.

Allen improves. This is seen in the internal energy profiles of Figure 19. Thus the variation in the centerline values appears to have been caused by the difference in boundary condition treatment.

6.3 Computational Experiments

This section discusses the numerical considerations and the results of some experiments concerning grid size, time step size, and initial conditions.

All computations were done on the CDC 6600 of the Georgia Tech Cyber-74 computer system. The storage capacity of this machine permits over 5000 computational grid points, though that many were never used. The solution of the four conservation equations using 1056 grid point in the flow field (coarse mesh) required 10 CPU minutes to 1 CPU hour, depending on the convergence criteria (see Section 6.3-2), the size of the time step (Section 6.3-3), and on the initial conditions (Section 6.3-4).

The basic grid configuration used 48 points in the x-direction and 24 points in the y-direction. The length of the upper wall was 4/3 the back wall height. This was 23% longer than used by Allen and Cheng. The downstream boundary was also further from the back wall than in Allen and Cheng, being 6 2/3 step heights away compared with 5.13. For the finer mesh experiments, the number of grid points in each direction was doubled with all distances remaining the same. Thus the coarse mesh solutions used 1056 grid points in the flow field, and the fine mesh had 4224.

6.3-1 Fine Mesh Comparisons

To test the accuracy of the coarse mesh it is desirable to make

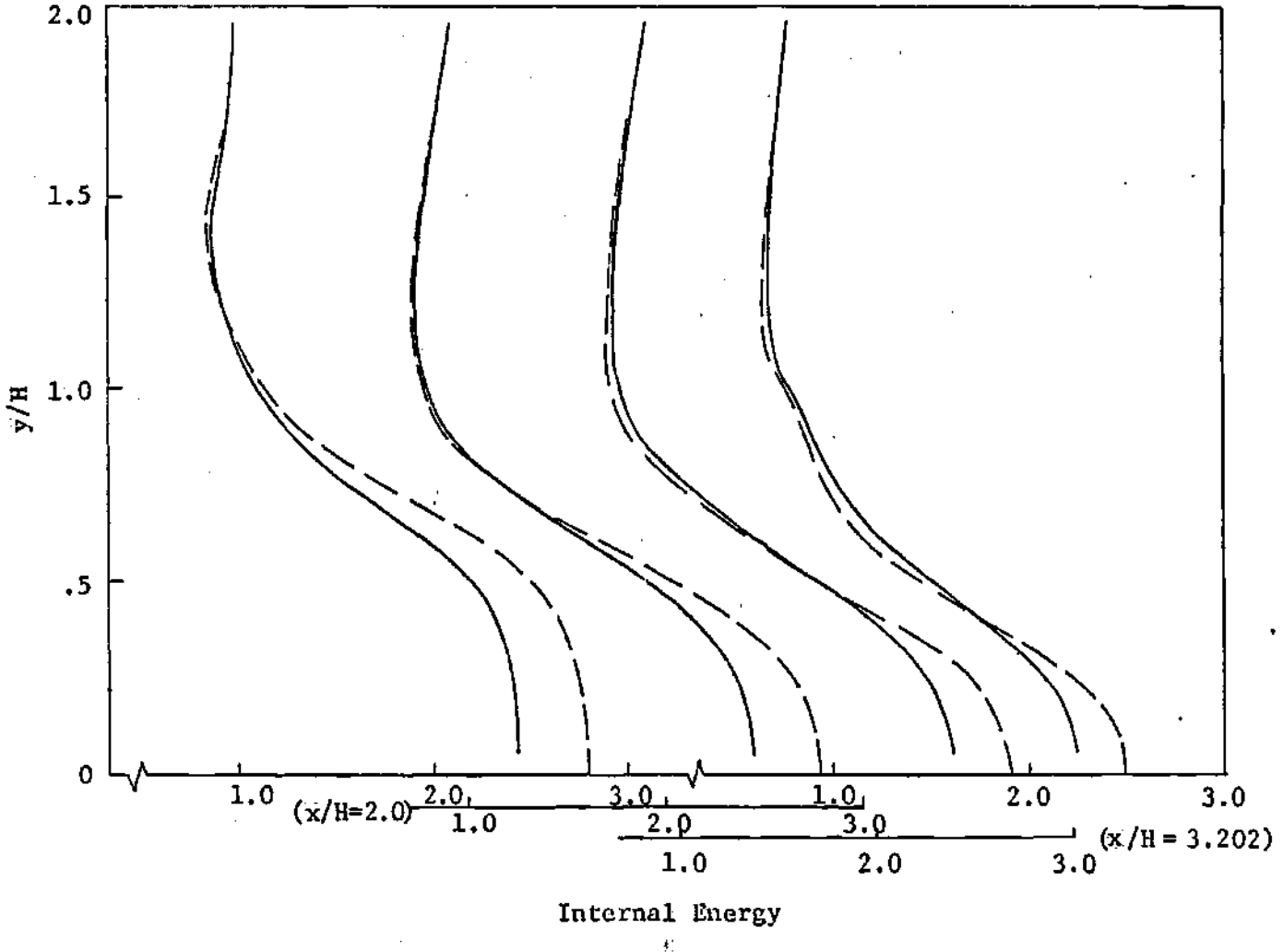

Figure 19. Internal Energy Profiles.

the same computations with a much finer grid. Since the finite-difference equations are consistent with the differential equations (see Chapter III), greater accuracy should be expected as Δx and Δy get smaller. In addition, the scale of variation of some quantities is not large compared with the size of the coarse mesh. A smaller mesh would thus increase resolution.

The mesh was made finer by dividing each coarse mesh cell into four equal cells (see Figure 20). Thus no fine mesh point coincides with a coarse mesh point, and to compare the two solutions, values at the four fine mesh points located in a coarse mesh cell were averaged. The basic results of the fine mesh computations are given in Appendix D.

Two comparisons between fine and coarse grid computations were made. The first uses the form

$$\left|\frac{\phi_{coarse} - \phi_{fine}}{\phi_{fine}}\right| \tag{6-41}$$

This form is useful for ϕ near or greater than 1 and represents a percentage change. For ϕ small (i.e., near zero), equation (6-41) can give a large number, even for a small change in ϕ. In this case a more appropriate comparison may be the simple form

$$|\phi_{fine} - \phi_{coarse}| \tag{6-42}$$

Tables 1 and 2 show the results of using both equation (6-41) and (6-42). For equation (6-41), ϕ is also given. Table 1 gives the maximum difference in the flow field between the coarse and fine meshes. Most of these maximum differences occur near the back wall.

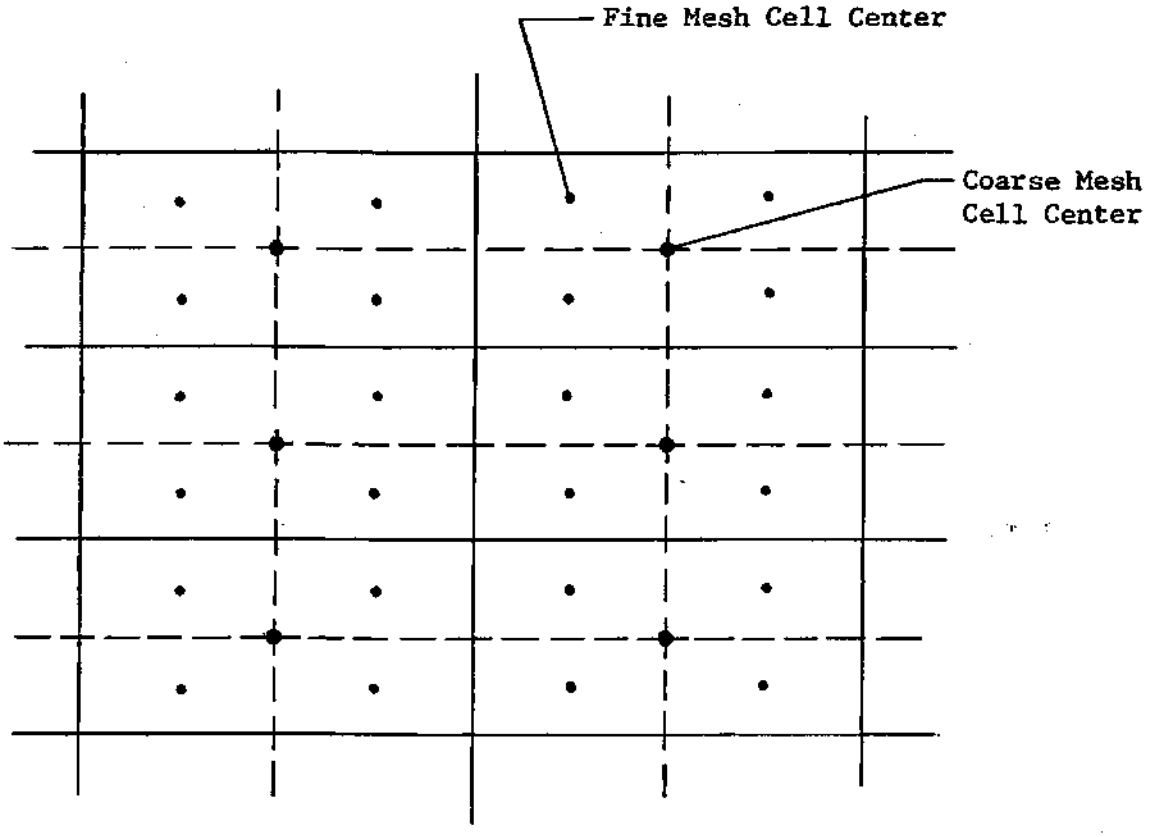

Figure 20. Coarse and Fine Mesh Cell Centers.

Table 1. Coarse-fine Mesh Comparisons - Flow Field Maximums

ϕ	$\lvert\Delta\phi/\phi_f\rvert_{max}$	i	j	ϕ_f	$\lvert\Delta\phi\rvert_{max}$	i	j
ρ	.227	9	10	.050	.048	47	12
u	26.713	9	6	-.0002	.098	9	12
v	8.733	9	9	.0032	.045	9	13
e	.070	9	13	1.898	.133	9	13
p	.231	9	10	.117	.086	8	16

$$\Delta\phi = \phi_{fine} - \phi_{coarse} = \phi_f - \phi_c$$

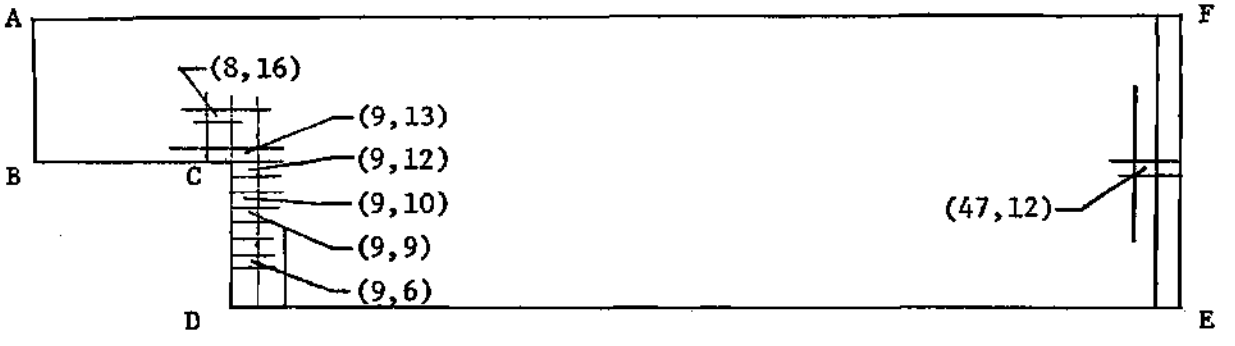

Table 2. Coarse-fine Mesh Comparisons - Selected Points

Point	ϕ	$\lvert\Delta\phi/\phi_f\rvert$	ϕ_f	$\lvert\Delta\phi\rvert$
(9,13)	ρ	.027	.167	.004
near C	u	.112	.540	.060
	v	.193	-.231	.045
	e	.070	1.898	.133
	p	.095	.318	.030
(9,1)	ρ	.029	.084	.002
near D	u	.323	-.007	.002
	v	.201	.004	.001
	e	.003	2.385	.007
	p	.032	.199	.006
(48,1)	ρ	.044	.316	.014
near E	u	.018	.492	.009
	v	.038	-.004	.0001
	e	.008	2.140	.018
	p	.053	.676	.036
(37,17)	ρ	.021	.374	.008
	u	.003	1.062	.003
	v	.038	-.236	.009
	e	.007	.678	.005
	p	.028	.254	.007

$$\Delta\phi = \phi_{fine} - \phi_{coarse} = \phi_f - \phi_c$$

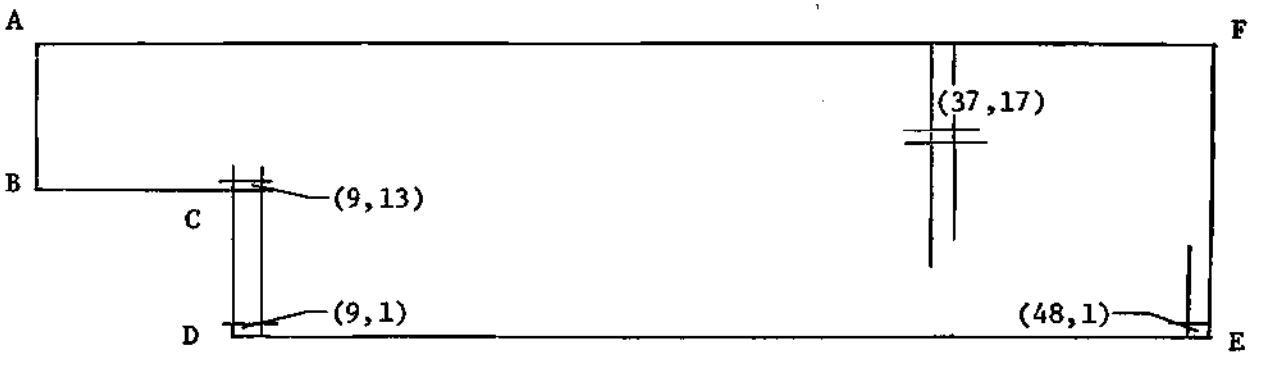

Table 2 gives the result for some selected points in the flow field. Included are the cells nearest to corner point C, corner point D, corner point E, and a point about 4.8 step heights downstream and in the recompression. Again, the largest differences are near the back wall. This serves to point out the sensitivity of this region.

One important result of the fine mesh study was to show that the coarse mesh was responsible for the irregularities near the inflow and those in the shock near the downstream boundary. Apparently, the finer mesh allowed greater resolution. Figure 21 is a three-dimensional plot of the pressure using the fine mesh.

A single wave remains at the inflow, but its character is different from those in the coarse mesh. This wave has an angle of about 21°, relatively close to the inflow Mach angle (19.5°) and appears to be related to the choice of inflow boundary conditions. As mentioned previously, $\partial p/\partial y$ was assumed to be zero along the inflow, but it can be seen that the expansion corner is being felt even this far upstream (4/3 H) to reduce the pressure near the wall. The wave, originating at the top of the boundary layer, may be a flow adjustment because of the inconsistency. The wave may also be caused by the change from the boundary layer u-profile to the freestream u = const. profile.

6.3.2 Convergence Criteria

As the rate of change with time of the dependent variables in the flow field decreases, the solution is said to be converging. When this rate is zero, the steady state has been reached. It is usually not necessary or practical to continue the calculation until the rate

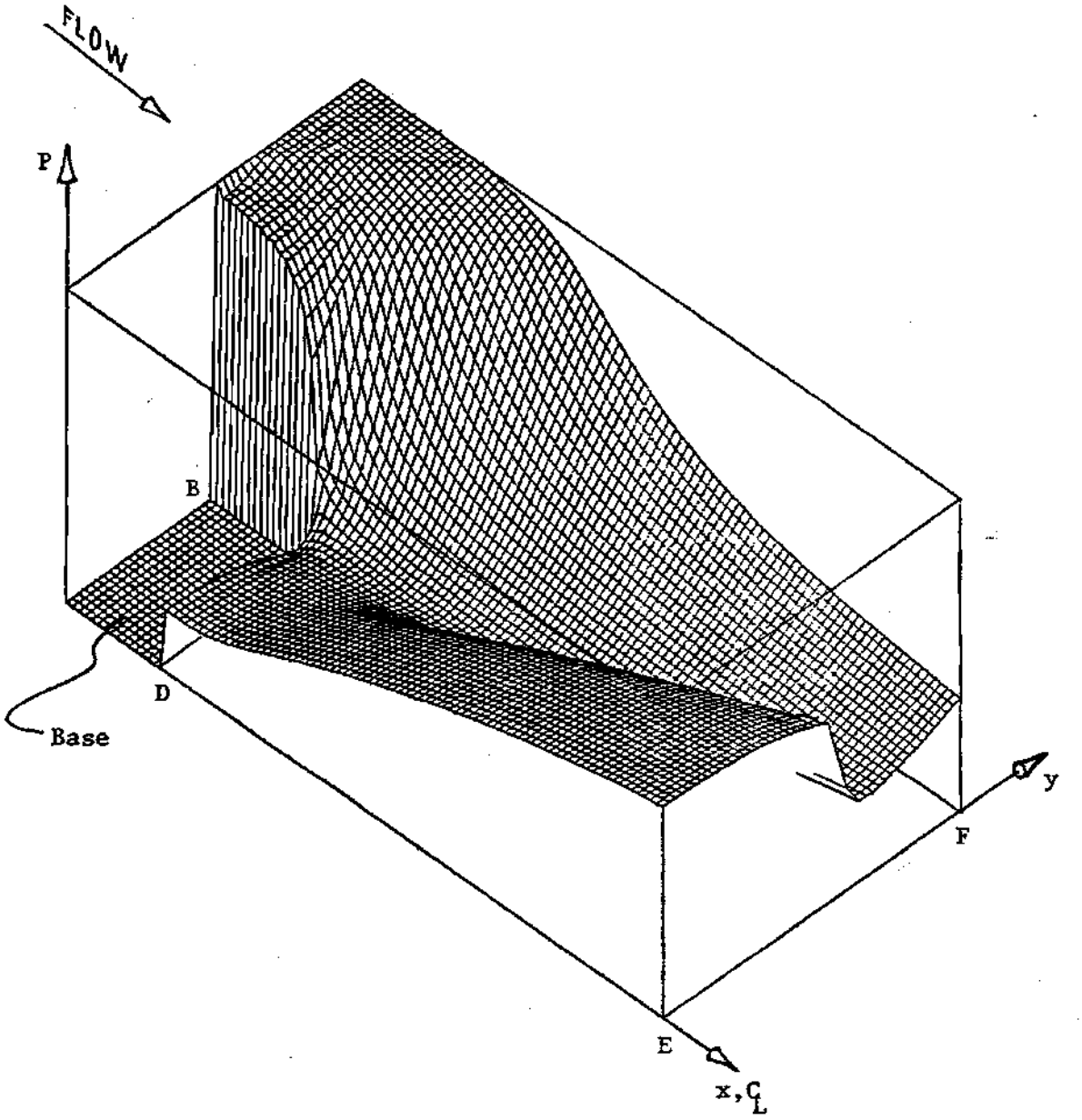

Figure 21. Pressure Surface - Fine Mesh.

is zero, however. Allen, for example, uses a convergence criteria of

$$|\rho^{n+1} - \rho^{n}|_{max} < \varepsilon \tag{6-43}$$

where $2 \times 10^{-6} < \varepsilon < 2 \times 10^{-5}$.

In the present work, the form normally used was

$$\frac{|\rho^{n+1} - \rho^{n}|_{max}}{\rho^{n}} < \varepsilon_1 \tag{6-44}$$

with ρ^n known, the range of $(\rho^n \varepsilon_1)$ can be compared directly with the range of Allen's ε:

$$2 \times 10^{-6} < \rho^{n}\varepsilon_1 < 5.3 \times 10^{-5} \tag{6-45}$$

As in Allen and Cheng,[25] a check on density was normally sufficient to determine convergence. Equation (6-44) was applied also to u, v and e as an additional check.

The rate of convergence varied over the whole flow field. The most rapid convergence was in the supersonic regions, especially upstream of the corner. The slowest rate of convergence was in the region near the back wall. It may be possible, therefore, to shorten the calculation for cases where the near wall region is not a region of primary interest.

6.3.3 Time Step Studies

As mentioned before, the chief advantage in using an implicit procedure is the ability to use larger time steps than allowable in explicit methods, and hence reduce computation time. Here, the CFL stability condition in two dimensions is

$$\Delta t_{CFL} \leq \left[\frac{1}{\Delta x} + \frac{1}{m_1}\left(\frac{1}{\Delta x^2} + \frac{1}{\Delta y^2}\right)^{1/2}\right]^{-1} \qquad (6\text{-}46)$$

In the present work, a time step size of $\Delta t = 4\Delta t_{CFL}$ was used while developing the method. This was chosen because it is large enough to be appreciably larger than Δt_{CFL} but small enough to avoid possible problems with the initial conditions. Results for $\Delta t = 4\ \Delta t_{CFL}$ were given in Section 6.2.

To examine the ability of the procedure to use larger time steps, $\Delta t = 8$, 16, 32 and 40 Δt_{CFL} were also attempted. A time step limitation was expected because the finite-difference equations are linearized with respect to time about the known time level. This allows a simpler and more rapid solution of the finite-difference equations than if they were left nonlinear. Still, the allowable Δt is much larger than Δt_{CFL}, which more than compensates for the larger computation time per time step relative to explicit methods.

For $\Delta t = 40\ \Delta t_{CFL}$ the solution did not converge, but diverged in less than 10 time steps. Whether this would happen with different initial conditions has not been determined. The rest of the discussion concerns the convergent solutions for $\Delta t = 4$, 8, 16, 32 Δt_{CFL}. The difference in the solutions at convergence for each of these time steps was very slight. The difference in ρ between the two solutions for $\Delta t = 4\Delta t_{CFL}$ and $\Delta t = 16\ \Delta t_{CFL}$, for example was typically around 1%.

For $\Delta t = 4$, 8, 16 Δt_{CFL}, the solution at equal elapsed times appeared quite similar, that is, the solution in time appeared to be relatively insensitive to the size of Δt. Table 3 presents the solution at

Table 3. Solutions at Equal Elapsed Times for Different Time Steps

		$\Delta t/\Delta t_{CFL}$ (T = 15.279)			$\Delta t/\Delta t_{CFL}$ (T = 76.393)		
Pt	ϕ	4	8	16	4	8	16
C	ρ	.19	.19	.21	.17	.17	.16
	u	.50	.51	.49	.56	.58	.58
	v	-.189	-.191	-.180	-.255	-.260	-.267
	e	1.98	1.97	1.89	1.85	1.83	1.81
	p	.38	.38	.40	.31	.31	.30
D	ρ	.37	.35	.33	.12	.15	.13
	u	-.01	-.01	-.01	-.01	-.01	-.01
	v	.004	.004	.005	.005	.005	.005
	e	1.08	1.14	1.24	2.07	2.05	2.02
	p	.40	.40	.41	.25	.26	.27
E	ρ	.96	.97	.94	.32	.32	.32
	u	.24	.24	.24	.35	.34	.32
	v	-.001	-.002	-.001	-.003	-.003	-.003
	e	1.00	1.00	1.00	2.20	2.21	2.21
	p	.97	.97	.94	.70	.71	.71
37,17	ρ	.74	.79	.79	.39	.40	.40
	u	1.02	1.01	1.01	1.06	1.06	1.06
	v	-.041	-.046	-.037	-.232	-.232	-.233
	e	.91	.94	.95	.69	.70	.70
	p	.68	.75	.76	.27	.28	.28
$T/\Delta t$		40	20	10	200	100	50

selected points in the flow field for elapsed times of T = 15.279 and T = 76.393 (where $T = H/U_1$) for Δt = 4, 8, and 16 Δt_{CFL}. It appears, then, that up to 16 Δt_{CFL}, for these initial conditions, doubling the time step allows the same point in time to be reached about twice as fast and thus doubles the rate of convergence. This can be seen in Figure 22 which gives the maximum time rate of change of density of the flow field versus the number of time steps. Since computation time is directly related to the number of time steps taken, this is shown as the lower abcissa. This figure clearly shows the substantial computation time savings from the ability to use larger time steps. The "humps" on each curve are caused by a shift in location of the maximum change in $\Delta\rho/\rho$ from a point near the outflow boundary to a point near the back wall.

The rate of convergence for $\Delta t = 32\ \Delta t_{CFL}$ is also given. Initial oscillations which damped out prevented the run at this time-step size from following the same temporal path as the other time-step sizes. This is reflected in Figure 22 as the convergence was not smooth. When the computation did smooth out, the solution still converged faster than 16 Δt_{CFL}, though not twice as fast.

The curve for $\Delta t = 8\Delta t_{CFL}$ shows a sudden drop at $t/\Delta t = 150$. As indicated, this corresponded to continuing the computation with $\Delta t = 32\Delta t_{CFL}$. This demonstrates that convergence can be speeded even after computation has begun by increasing the time step size. While no attempt was made to develop a scheme for relating time step size to rate of convergence, such procedures can be very useful to obtain very fast convergence.

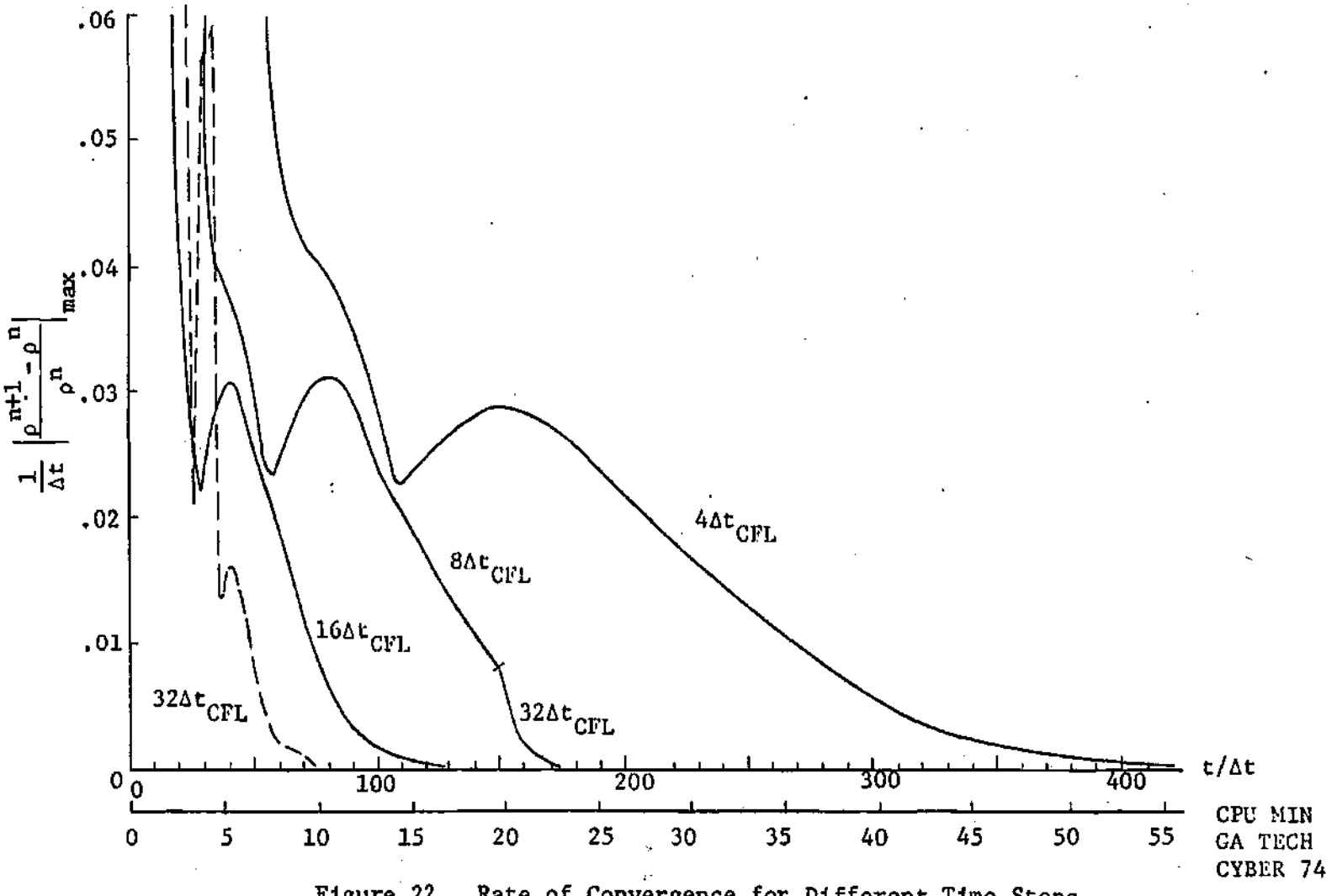

Figure 22. Rate of Convergence for Different Time Steps

The maximum time step also seems to be related to the grid size. For the fine mesh case, use of $\Delta t = 32\ \Delta t_{CFL}$ resulted in diverging oscillations related to the recompression (see Figure 23). However, the fine mesh solution was stopped at $t/\Delta t = 85$ and Δt was changed to $16\ \Delta t_{CFL}$. The oscillations decreased and the solution was stopped at $t/\Delta t = 300$. Figure 17 is the 3-D pressure plot. Convergence was greatly slowed by the presence of the initial oscillations. No other time step studies were accomplished with the fine mesh because of increased run time associated with the increased number of grid points.

As mentioned before, the computation time depends on the size of the time step and this was shown dramatically in Figure 22. The number of time steps required for the same degree of convergence was reduced nearly sixfold as Δt was increased from four to $32\ \Delta t_{CFL}$. In comparing the computation time with Allen's method, it was helpful that he had also made some calculations on a CDC-6600 machine. He required about 1.5 msec per time step per grid point and typically required between 1000 and 2000 time steps for convergence. The present procedure required 7.7 msec per time step per grid point. Since the present method was able to use a time step 30 times larger, this represents a sixfold decrease in overall computation time for these conditions.

6.3.4 Initial Conditions

To insure that the given initial conditions were not unique for a given set of boundary conditions, and to examine the effect of initial conditions on the ability to take large time steps, it is desirable to examine several different initial conditions. Computer time and cost, however, placed restrictions on the number of choices.

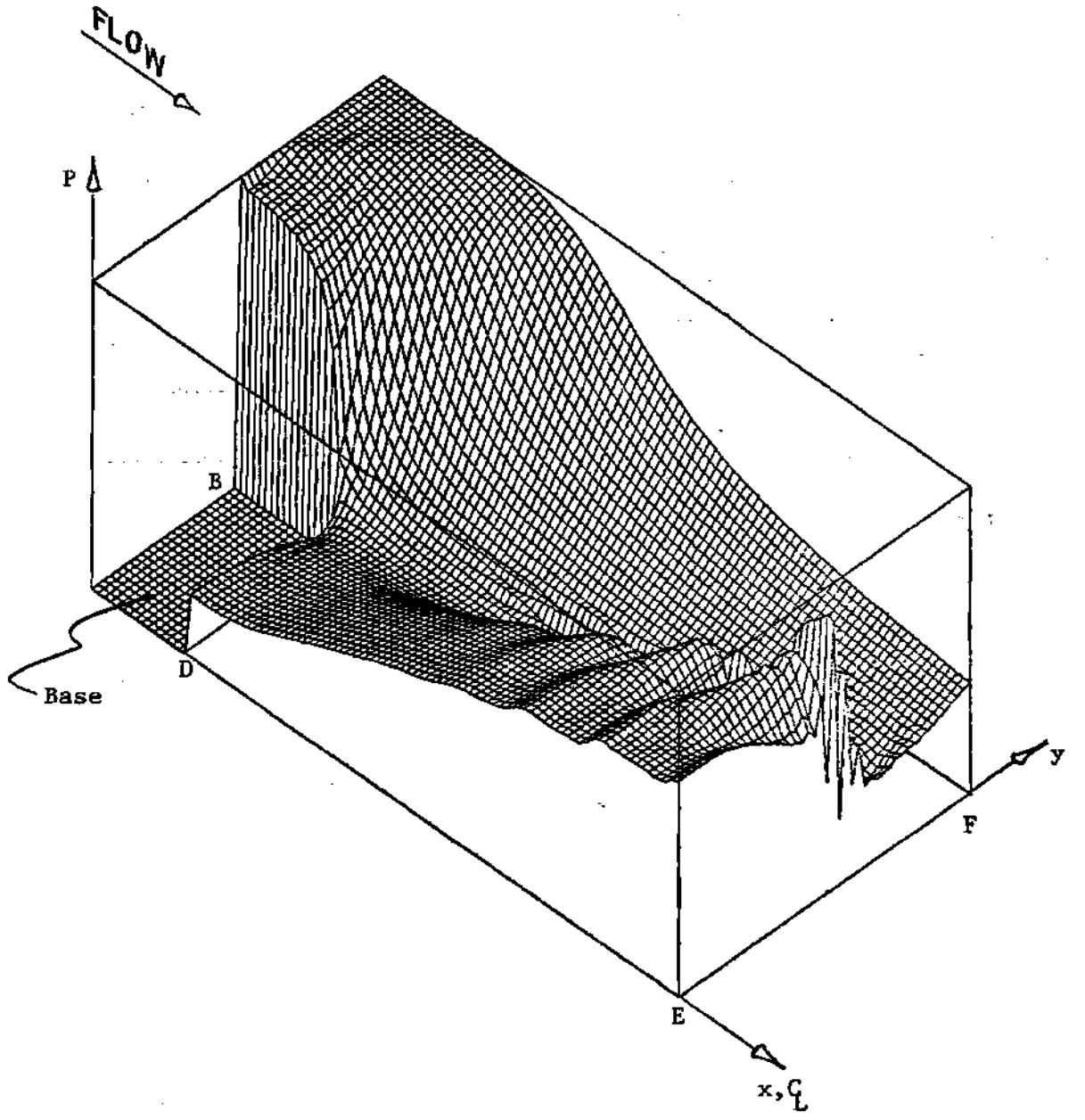

Figure 23. Pressure Surface - Fine Mesh with $\Delta t = 32\ \Delta t_{CFL}$ after 85 time Steps.

Since the region near the back wall (below the corner) seemed to be the most sensitive to other changes, a wide range of initial horizontal velocity components ($0 \leq u \leq 1.0$) below the corner was examined. The time step for this study was held fixed at $\Delta t = 16\ \Delta t_{CFL}$.

For $u = 0$, the computation diverged. For $0.1 \leq u \leq 1.0$, the computations converged. As in the case of different time step sizes, the final solutions for the different initial conditions were nearly identical. The rates of convergence, however, were much different. Figure 24 shows that for $u = 1.0$, the rate of convergence was several times faster than when $u = 0.1$. Note also that the convergence paths are not similar. The curve for $u = 0.3$, for example, has a rise at $t/\Delta t = 30$ corresponding to a shift of the maximum $\Delta\rho/\rho$ in the flow field from the downstream boundary to the back wall region. The shift of maximum $\Delta\rho/\rho$ to the back wall for $u = 1.0$ occurred at $t/\Delta t = 62$ but was not attended by a rise in the curve. The recirculation region appeared to already be near its final solution in this case.

6.3.5 Net Mass Flux

The net mass flux through the flow field was computed at each time step. In the steady state, the net mass flux should be zero. The computation was accomplished by summing $-\rho u \Delta y$ across the inflow boundary cells along AB, $\rho v \Delta x$ across the upper boundary cells along AF, and $\rho u \Delta y$ across the downstream boundary cells along EF. For coarse mesh solutions, the net inflow differed from the net outflow by 1.6 to 1.8%. For the fine mesh computations the difference was 1%.

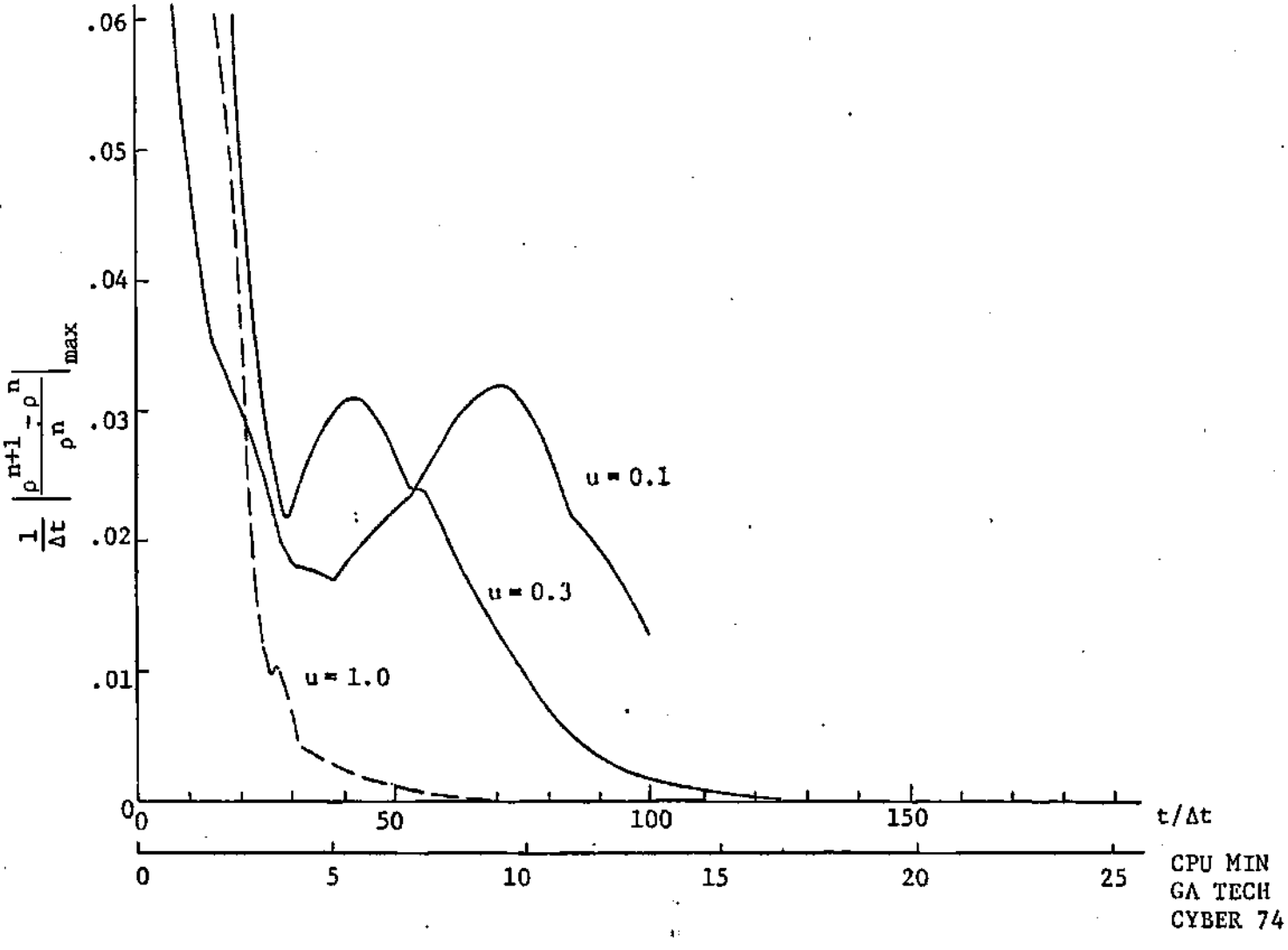

Figure 24. Rates of Convergence for Different Back Wall Initial Velocities $\Delta t = 16\Delta t_{CFL}$.

CHAPTER VII

CONCLUSIONS

1. The results in Section 6.2 show that the method successfully computed all the main features of the flow, including the corner expansion, the recompression shock, the recirculation region, the viscous wake near the centerline, and the simple wave nature of the flow near the upper boundary.

2. Great care must be taken in the formulation of the boundary conditions to achieve physically realistic results, convergence, and to avoid wiggles in the steady-state solution. First-order forms for pressure and $\partial v/\partial y$ on the centerline, for example, gave a converged solution but had y-direction wiggles in the steady state. Second-order, one-sided forms removed the wiggles. For the outflow boundary, all explicit extrapolation schemes caused divergence for $\Delta t > \Delta t_{CFL}$. Zero-gradient forms, both explicit and implicit, gave x-direction wiggles for the converged, steady state solution. A new implicit, linear extrapolation scheme which uses the finite difference equations was developed for the downstream boundary and gave a smooth, converged solution.

3. No artificial viscosity was required for stability and convergence. Briley and McDonald, however, required additional explicit artificial viscosity in their subsonic duct flow solutions. The reasons for this difference are not known. It may be speculated, however, that the difference arises from the present use of the conservative form of

the conservation equations (Briley and McDonald use the nonconservation form of the energy equation), the cell integration technique for generating finite-difference equations, and the corresponding careful treatment of the boundary conditions.

4. Three-dimensional contour plots were an important diagnostic tool. It was not discovered that the x-direction wiggles were caused by the treatment of the downstream boundary until the 3-D plots were made. The plots clearly revealed that as the recompression wave crossed the downstream boundary, the wiggles formed and propagated upstream to the back wall and inflow regions. Up to then, the wiggles were thought to have been caused by ill-treatment of the back wall boundary conditions or by the cell Reynolds numbers greater than two. The use of upwind differencing, artificial viscosity, or a much smaller Δx were avoided as they were considered to be undesirable remedies.

5. The results for the contour plots showed qualitative agreement with Allen and Cheng and with Kronzon, et al., and close quantitative agreement where comparisons were possible. The centerline pressure plot showed very close quantitative agreement with Allen and Cheng. As a further check on accuracy, overall mass balances were computed at each time step. For the coarse mesh solutions, the net mass inflow rate differed from the net mass outflow rate by 1.6 to 1.8%. For the fine mesh solutions the difference was about 1.0%.

6. For one set of initial conditions a time step limitation was established at about 32 Δt_{CFL}. The limitation was expected because the equations are linearized with time, even though the method is implicit.

Compared with Allen's procedure, this method had a computation time per time step per gria point approximately five times longer, but could take five steps over 30 times larger. This represents a six-fold decrease in computation time. In addition, the ability to change (increase) the size of the time step during computation to reduce the computation time was demonstrated. Thus a time step strategy might be successful wherein smaller Δt's were used at the beginning, followed by increasing Δt as the steady state is approached. This would be appropriate, for example, when the assumed initial conditions were very far from the steady state solution. Hence, the method appears to offer significant time savings.

7. The steady state solution was quite insensitive to the choice of initial conditions, but the time to convergence appeared to be highly dependent on them. A range of initial horizontal velocities were applied in the region below the expansion corner, while the boundary layer on the upper wall ahead of the corner and the freestream conditions for the rest of the flow were the same for these tests. It was shown that an initial $u = 0$ below the corner led to divergence for $\Delta t = 16\ \Delta t_{CFL}$. As u was increased from 10% to 100% of the freestream value, increasingly faster times to convergence were realized. In addition, convergence was shown for a significant range of initial backwall u.

8. Accuracy of the coarse mesh results was shown by comparisons with the fine mesh solution. Both solutions were in close agreement. Small, irregular disturbances in the inflow region and in the shock near the outflow boundary occurred in the coarse mesh solutions. These are attributable to the lack of the resolution in the coarse mesh in the inflow

boundary layer and in the shock at the outflow, as they disappeared in the fine mesh solution.

9. These numerical results served to demonstrate that this procedure produced stable, convergent, and accurate solutions, without the use of artificial viscosity, when applied to this complex problem. To the author's knowledge, no other implicit scheme has been successfully applied to the multidimensional, non-linear Navier-Stokes equations for the supersonic base flow problem.

APPENDIX A

THE LINEARIZED CONSERVATION EQUATIONS

Conservation of Mass

Also given as equation (3-1)

$$\left(\frac{\rho^{n+1} - \rho^{n}}{\Delta t}\right) = -\frac{\partial}{\partial x}\left[\rho^{n+1}u^{n} + \rho^{n}u^{n+1} - \rho^{n}u^{n}\right] - \frac{\partial}{\partial y}\left[\rho^{n}v^{n+1} + \rho^{n+1}v^{n} - \rho^{n}v^{n}\right] \quad \text{(A-1)}$$

Conservation of x-Momentum

Application of the linearization to equation (2-12) gives:

$$\left(\frac{\rho^{n+1}u^{n} + \rho^{n}u^{n+1} - 2\rho^{n}u^{n}}{\Delta t}\right) = -\frac{\partial}{\partial x}\left[\rho^{n+1}u^{n^2} + 2\rho^{n}u^{n}u^{n+1} - 2\rho^{n}u^{n^2} + \frac{1}{\gamma M_1^2}\left(\rho^{n+1}e^{n}\right.\right.$$

$$\left. + \rho^{n}e^{n+1} - \rho^{n}e^{n}\right) - \frac{1}{Re}\,S_{xx}^{n+1}\Big] - \frac{\partial}{\partial y}\left[\rho^{n+1}u^{n}v^{n} + \rho^{n}u^{n+1}v^{n} + \rho^{n}u^{n}v^{n+1}\right.$$

$$\left. - 2\rho^{n}u^{n}v^{n} - \frac{1}{Re}\,S_{xy}^{n+1}\right] \quad \text{(A-2)}$$

$$S_{xx} = \frac{4}{3}\frac{\partial u}{\partial x} - \frac{2}{3}\frac{\partial v}{\partial y}$$

$$S_{xy} = \frac{\partial u}{\partial y} + \frac{\partial v}{\partial x}$$

Conservation of y-Momentum

Application of the linearization to equation (2-13) gives:

$$\left(\frac{\rho^{n+1}v^{n}+\rho^{n}v^{n+1}-2\rho^{n}v^{n}}{\Delta t}\right) = -\frac{\partial}{\partial x}\left[\rho^{n+1}u^{n}v^{n}+\rho^{n}u^{n+1}v^{n}+\rho^{n}u^{n}v^{n+1}-2\rho^{n}u^{n}v^{n}\right.$$

$$\left.-\frac{1}{Re}S_{xy}^{n+1}\right]-\frac{\partial}{\partial y}\left[\rho^{n+1}v^{n2}+2\rho^{n}v^{n}v^{n+1}-2\rho^{n}v^{n2}+\frac{\partial 1}{\gamma M_1^2}\left(\rho^{n+1}e^{n}+\rho^{n}e^{n+1}\right.\right.$$

$$\left.\left.-\rho^{n}e^{n}\right)-\frac{1}{Re}S_{yy}^{n+1}\right] \qquad \text{(A-3)}$$

$$S_{yy} = \frac{4}{3}\frac{\partial v}{\partial y}-\frac{2}{3}\frac{\partial u}{\partial x}$$

Conservation of Energy

Equation (2-14) becomes:

$$\frac{1}{\Delta t}\left\{\rho^{n+1}e^{n}+\rho^{n}e^{n+1}-2\rho^{n}e^{n}+\rho^{n+1}\frac{K}{2}\left(u^{n2}+v^{n2}\right)+\rho^{n}K\left[u^{n+1}u^{n}+v^{n+1}v^{n}\right.\right.$$

$$\left.\left.-\frac{3}{2}\left(u^2+v^2\right)\right]\right\} = -\frac{\partial}{\partial x}\left\{\gamma\left(\rho^{n+1}u^{n}e^{n}+\rho^{n}u^{n+1}e^{n}+\rho^{n}u^{n}e^{n+1}-2\rho^{n}u^{n}e^{n}\right)\right.$$

$$+\frac{K}{2}\left[\rho^{n+1}u^{n}\left(u^{n2}+v^{n2}\right)+3\rho^{n}u^{n+1}u^{n2}+\rho^{n}u^{n+1}v^{n2}+2\rho^{n}u^{n}v^{n}v^{n+1}\right.$$

$$\left.\left.-3\rho^{n}u^{n}\left(u^{n2}+v^{n2}\right)\right]-\frac{\gamma}{PrRe}\frac{\partial}{\partial x}e^{n+1}\right\}-\frac{\partial}{\partial y}\left\{\gamma\left(\rho^{n+1}v^{n}e^{n}+\rho^{n}v^{n+1}e^{n}\right.\right.$$

$$+\rho^{n}v^{n}e^{n+1}-2\rho^{n}v^{n}e^{n}\left.\right)+\frac{K}{2}\left[\rho^{n+1}v^{n}\left(u^{n2}+v^{n2}\right)+\rho^{n}u^{n+1}v^{n2}+2\rho^{n}v^{n}u^{n}u^{n+1}\right.$$

$$\left.+3\rho^{n}v^{n2}v^{n+1}-3\,\rho^{n}v^{n}\left(u^{n2}+v^{n2}\right)\right]-\frac{\gamma}{RePr}\frac{\partial}{\partial y}e^{n+1}\left.\right\}+K\left[\frac{\partial}{\partial x}\left(u^{n}\tau_{xx}^{n}\right.\right.$$

$$\left.\left.+v^{n}\tau_{xy}^{n}\right)+\frac{\partial}{\partial y}\left(u^{n}\tau_{xy}^{n}+v\tau_{yy}^{n}\right)\right] \qquad \text{(A-4)}$$

τ_{xx}, τ_{xy}, and τ_{yy} are given in Chapter II.

APPENDIX B

FINITE DIFFERENCE FORMS OF THE CONSERVATION EQUATIONS

Conservation of Mass

Also given as equation (3-6)

$$\partial\rho/\partial t = -\delta x(\rho u) - \delta y(\rho v) \tag{B-1}$$

Conservation of x-Momentum

$$\partial\rho u/\partial t = -\delta x[\rho u^2 + (\frac{1}{\gamma M_1^2})\rho e - \tau_{xx}] - \delta y[\rho uv - \tau_{xy}] \tag{B-2}$$

Conservation of y-Momentum

$$\partial\rho v/\partial t = -\delta x[\rho uv - \tau_{xy}] - \delta y[\rho v^2 + (\frac{1}{\gamma M_1^2})\rho e - \tau_{yy}] \tag{B-3}$$

Conservation of Energy

$$\begin{aligned}\frac{\partial}{\partial t}\,[\rho e + \tfrac{K}{2}\,(u^2+v^2)] = &-\delta x\{\rho u[\gamma e + \tfrac{K}{2}\,(u^2+v^2)] + (\tfrac{\gamma}{PrRe})\,q_x \\ &- (\tfrac{K}{Re})(u\tau_{xx} + v\tau_{yy})\} - \delta y\{\rho v[\gamma e + \tfrac{K}{2}\,(u^2+v^2)] + (\tfrac{\gamma}{PrRe})q_y \\ &- (\tfrac{K}{Re})(u\tau_{xy} + v\tau_{yy})\}\end{aligned} \tag{B-4}$$

$\tau_{xx}, \tau_{xy}, \tau_{yy}$, q_x, and q_y are given in Chapter II.

APPENDIX C

ALTERNATING DIRECTION IMPLICIT FORMS OF THE CONSERVATION EQUATIONS

Conservation of Mass

$$\left(\frac{\rho^{*} - \rho}{\Delta t}\right) = -\delta x[\rho^{*}u + \rho u^{*} - \rho u] - \delta y[\rho v] \tag{C-1}$$

$$\left(\frac{\rho^{**} - \rho}{\Delta t}\right) = -\delta x[\rho^{*}u + \rho u^{*} - \rho u] - \delta y[\rho^{**}v + v^{**} - \rho v] \tag{C-2}$$

Subtracting (C-1) from (C-2) a simplified system is:

$$\frac{(\rho^{*} - \rho)}{\Delta t} = -\delta x[\rho^{*}u + u^{*} - \rho u] - \delta y[\rho v] \tag{C-3}$$

$$\left(\frac{\rho^{**} - \rho^{*}}{\Delta t}\right) = -\delta y[\rho^{**}v + \rho v^{**} - 2\rho v] \tag{C-4}$$

Here a quantity with no superscript is considered as being an n-level quantity. All the remaining equations are written in the simplified form.

Conservation of x-Momentum

$$\left(\frac{\rho^{*}u + \rho u^{*} - 2\rho u}{\Delta t}\right) = -\delta x[\rho^{*}u^{2} + 2\rho u u^{*} - 2\rho u^{2} + \left(\frac{1}{\gamma M_1^2}\right)(\rho^{*}e + \rho e^{*} - \rho e)$$

$$- \frac{1}{Re}\left(\frac{4}{3}\delta x\, u^{*} - \frac{2}{3}\delta y\, v\right)] - \delta y[\rho uv - \tau_{xy}] \tag{C-5}$$

$$\left(\frac{\rho^{**}u + \rho u^{**} - \rho^{*}u - u^{*}}{\Delta t}\right) = -\delta y[\rho^{**}uv + \rho u^{**}v + \rho uv^{**} - 3\rho uv - \frac{1}{Re}\delta y(u^{**} - u)] \tag{C-6}$$

Conservation of y-Momentum

$$\left(\frac{\rho^{*}v+\rho v^{*}-2\rho v}{\Delta t}\right) = -\delta x[\rho^{*}uv + \rho u^{*}v + \rho uv^{*} - 2\rho uv - \frac{1}{Re}(\delta yu + \delta x\, v^{*})]$$

$$- \delta y[\rho v^{2} + \left(\frac{1}{\gamma M_{1}^{2}}\right)\rho e - \tau_{yy}] \qquad \text{(C-7)}$$

$$\left(\frac{\rho^{**}v + \rho v^{**} - \rho^{*}v - \rho v^{*}}{\Delta t}\right) = -\delta y[\rho^{**}v^{2} + 2\rho vv^{**} - 3\rho v^{2} + \left(\frac{1}{\gamma M_{1}^{2}}\right)(\rho^{**}e$$

$$+ \rho e^{**} - 2\rho e) - \frac{1}{Re}\,\delta y(v^{**} - v)] \qquad \text{(C-8)}$$

Conservation of Energy

$$\frac{1}{\Delta t}\{\rho^{*}e + \rho e^{*} - 2\rho e + \rho^{*}\frac{K}{2}(u^{2}+v^{2}) + \rho K[u^{*}u + v^{*}v - \frac{3}{2}(u^{2}+v^{2})]\} =$$

$$-\delta x\{\gamma(\rho^{*}ue + \rho u^{*}e + \rho ue^{*} - 2\rho ue) + \frac{K}{2}[\rho^{*}u(u^{2}+v^{2}) + 3\rho u^{2}u^{*} + \rho u^{*}v^{2}$$

$$+ 2\rho uvv^{*} - 3\rho u(u^{2}+v^{2})] - \frac{\gamma}{PrRe}\,\delta xe^{*}\} - \delta y\{\rho v[\gamma e + \frac{K}{2}(u^{2}+v^{2})]$$

$$- \frac{\gamma}{PrRe}\,\delta y\, e\} + K[\frac{\partial}{\partial x}(u\tau_{xx} + v\tau_{xy}) + \frac{\partial}{\partial y}(u\tau_{xy} + v\tau_{yy})]\} \qquad \text{(C-9)}$$

$$\frac{1}{\Delta t}\{(\rho^{**} - \rho^{*})[e + \frac{K}{2}(u^{2} + v^{2})] + \rho K[(u^{**} - u^{*})u + (v^{**} - v^{*})v]$$

$$+ \rho(e^{**} - e^{*})\} = -\delta y\{(\rho^{**} - \rho)v[\gamma e + \frac{K}{2}(u^{2}+v^{2})] + \rho(v^{**} - v)[\gamma e$$

$$+ \frac{K}{2}(u^{2}+v^{2})] + \rho K(u^{**} - u)uv - \frac{\gamma}{PrRe}\,\delta y(e^{**} - e)\} \qquad \text{(C-10)}$$

τ_{xy} and τ_{yy} are given in Chapter II.

APPENDIX D

COEFFICIENT MATRICES

The coefficient matrices for the x-sweep equations are:

$$\overline{\overline{c}}_i^n = \begin{vmatrix} \frac{-u^n}{2\Delta x} & \frac{-\rho^n}{2\Delta x} & 0 & 0 \\ \frac{-1}{2\Delta x}\left(u^{n^2} + \frac{e^n}{\gamma M^2}\right) & \frac{-\rho^n v^n}{\Delta x} - \frac{4}{3Re\Delta x^2} & 0 & \frac{-\rho^n}{2\gamma M_1^2 \Delta x} \\ \frac{-u^n v^n}{2\Delta x} & \frac{-\rho^n v^n}{2\Delta x} & \frac{-\rho^n u^n}{2\Delta x} - \frac{1}{Re\Delta x^2} & 0 \\ \frac{-u^n(\gamma e^n + \frac{K}{2}(u^2+v^2))}{2\Delta x} & \frac{-\rho^n(\gamma e^n + \frac{K}{2}(3u^2+v^2))}{2\Delta x} & \frac{-K\rho^n u^n v^n}{2\Delta x} & \frac{-\gamma\rho^n u^n}{2\Delta x} - \frac{\gamma}{PrRe\Delta x^2} \end{vmatrix}_{i-1,j}$$

$$\overline{\overline{b}}_i^n = \begin{vmatrix} \frac{1}{\Delta t} & 0 & 0 & 0 \\ \frac{u^n}{\Delta t} & \frac{\rho^n}{\Delta t} + \frac{8}{3Re\Delta x^2} & 0 & 0 \\ \frac{v^n}{t} & 0 & \frac{\rho^n}{\Delta t} + \frac{2}{Re\Delta x^2} & 0 \\ \frac{e^n + \frac{K}{2}(u^2+v^2)}{\Delta t} & \frac{K\rho^n u^n}{\Delta t} & \frac{K\rho^n v^n}{\Delta t} & \frac{\rho^n}{\Delta t} + \frac{2\gamma}{RePr\Delta x^2} \end{vmatrix}_{ij}$$

$$\overline{\overline{a}}_i^n = \begin{vmatrix} \frac{u^n}{2\Delta x} & \frac{\rho^n}{2\Delta x} & 0 & 0 \\ \frac{1}{2\Delta x}\left(u^{n^2} + \frac{e^n}{\gamma M_1^2}\right) & \frac{\rho^n u^n}{\Delta x} - \frac{8}{3Re\Delta x^2} & 0 & \frac{\rho^n}{2\gamma M_1^2 \Delta x} \\ \frac{u^n v^n}{2\Delta x} & \frac{\rho^n v^n}{2\Delta x} & \frac{\rho^n u^n}{2\Delta x} - \frac{1}{Re\Delta x^2} & 0 \\ \frac{u^n(\gamma e^n + \frac{K}{2}(u^2+v^2))}{2\Delta x} & \frac{\rho^n(\gamma e^n + \frac{K}{2}(3u^{n^2} + v^{n^2})}{2\Delta x} & \frac{K\rho^n u^n v^n}{2\Delta x} & \frac{\gamma\rho^n u^n}{2\Delta x} - \frac{\gamma}{PrRe\Delta x^2} \end{vmatrix}_{i+1,j}$$

The coefficient matrices for the y-sweep equations are:

$$\overline{\overline{\gamma}}_j^n = \begin{vmatrix} \frac{-v^n}{2\Delta y} & 0 & \frac{-\rho^n}{2\Delta y} & 0 \\ \frac{-u^n v^n}{2\Delta y} & \frac{-\rho^n v^n}{2\Delta y} - \frac{1}{Re\Delta y^2} & \frac{-\rho^n u^n}{2\Delta y} & 0 \\ \frac{-v^{n^2}}{2\Delta y} - \frac{e^n}{2\Delta y \gamma M_1^2} & 0 & \frac{-\rho^n v^n}{\Delta y} - \frac{4}{3Re\Delta y^2} & \frac{-\rho^n}{2\Delta y \gamma M_1^2} \\ \frac{-v^n(\gamma e^n + \frac{K}{2}(u^2+v^2))}{2\Delta y} & \frac{-\rho^n K u^n v^n}{2\Delta y} & \frac{-\rho^n(\gamma e^n + \frac{K}{2}(u^2+3v^2))}{2\Delta y} & \frac{-\gamma\rho^n v^n}{2\Delta y} - \frac{\gamma}{PrRe\Delta y^2} \end{vmatrix}_{i,j-1}$$

$$\bar{\bar{\beta}}_j^n = \begin{pmatrix} \frac{1}{\Delta t} & 0 & 0 & 0 \\ \frac{u^n}{\Delta t} & \frac{\rho^n}{\Delta t} + \frac{2}{Re\Delta y^2} & 0 & 0 \\ \frac{v^n}{\Delta t} & 0 & \frac{\rho^n}{\Delta t} + \frac{8}{3Re\Delta y^2} & 0 \\ \frac{e^n + \frac{K}{2}(u^2+v^2)}{\Delta t} & \frac{K\rho^n u^n}{\Delta t} & \frac{K\rho^n v^n}{\Delta t} & \frac{\rho^n}{\Delta t} + \frac{2\gamma}{PrRe\Delta y^2} \end{pmatrix}_{ij}$$

$$\bar{\bar{\alpha}}_j^n = \begin{pmatrix} \frac{v^n}{2\Delta y} & 0 & \frac{\rho^n}{2\Delta y} & 0 \\ \frac{u^n v^n}{2\Delta y} & \frac{\rho^n v^n}{2\Delta y} - \frac{1}{Re\Delta y^2} & \frac{\rho^n u^n}{2\Delta y} & 0 \\ \frac{v^{n^2}}{2\Delta y} + \frac{e^n}{2\Delta y\gamma M_1^2} & 0 & \frac{\rho^n v^n}{\Delta y} - \frac{4}{3Re\Delta y^2} & \frac{\rho^n}{2\Delta y\gamma M_1^2} \\ \frac{v^n(\gamma e^n + \frac{K}{2}(u^2+v^2))}{2\Delta y} & \frac{\rho^n K n u^n v^n}{2\Delta y} & \frac{\rho^n(\gamma e^n + \frac{K}{2}(u^2+3v^2))}{2\Delta y} & \frac{\gamma\rho^n v^n}{2\Delta y} - \frac{\gamma}{PrRe\Delta y^2} \end{pmatrix}_{ij+1}$$

The right hand side column vector for the x-sweep equations is:

$$\bar{d}_i^n = \begin{pmatrix} \frac{\rho^n}{\Delta t} + \delta x(\rho^n u^n) - \delta y(\rho^n v^n) \\ \frac{2\rho^n u^n}{\Delta t} + \delta x[2\rho^n u^{n^2} + \frac{\rho^n e^n}{\gamma M_1^2} - \frac{2}{3Re}\delta y v^n] - \delta y[\rho^n u^n v^n - \frac{1}{Re}(\delta y u^n + \delta x v^n)] \\ \frac{2\rho^n v^n}{\Delta t} + \delta x[2\rho^n u^n v^n + \frac{1}{Re}\delta y u^n] - \delta y[\rho^n v^{n^2} + \frac{\rho^n e^n}{\gamma M_1^2} - \frac{1}{Re}(\frac{4}{3}\delta y v^n - \frac{2}{3}\delta x u^n)] \\ \frac{\rho^n(2e^n + \frac{3K}{2}(u^{n^2} + v^{n^2}))}{\Delta t} + \delta x[\rho^n u^n(2\gamma e^n + \frac{3K}{2}(u^{n^2} + v^{n^2}))] - \\ -\delta y[\rho^n v^n(\gamma e^n + \frac{K}{2}(u^{n^2} + v^{n^2})) - \frac{\gamma}{PrRe}\delta y e^n] + K\{\delta x(u\tau_{xx} + v\tau_{xy}) \\ + \delta y(u\tau_{xy} + v\tau_{yy})\} \end{pmatrix}$$

The two right hand side matrices for the y-sweep equations are:

$$\bar{\xi}_j^* = \begin{pmatrix} \frac{\rho^*}{\Delta t} \\ \frac{\rho^* u^n + \rho^n u^*}{\Delta t} \\ \frac{\rho^* v^n + \rho^n v^*}{\Delta t} \\ \frac{\rho^*(e^n + \frac{K}{2}(u^2 + v^2)) + \rho^n K(u^* u^n + v^* v^n) + \rho^n e^*}{\Delta t} \end{pmatrix}$$

$$\overline{n}_j^n = \left| \begin{array}{c} 2\delta y(\rho^n v^n) \\ \hline \delta y[3\rho^n u^n v^n - \frac{1}{Re}\delta y\, u^n] \\ \hline \delta y[3\rho^n v^{n^2} + 2(\frac{\rho^n e^n}{\gamma M_1^2}) - \frac{4}{3Re}\delta y\, v^n] \\ \hline \delta y[\rho^n v^n(3\gamma e^n + 2K(u^{n^2} + v^{n^2})) - \frac{\gamma}{PrRe}\delta y\, e^n] \end{array} \right|$$

APPENDIX E

FINE MESH RESULTS

The following figures are the results for the fine mesh computations. There were 4224 grid points in the flow field. The ratio of $\Delta x/\Delta y$ was 2.0 with $\Delta x = 1/12$. The inflow Mach number was 3.0 and the Reynolds number was 550. The time step size used to reach convergence was 16 Δt_{CFL}.

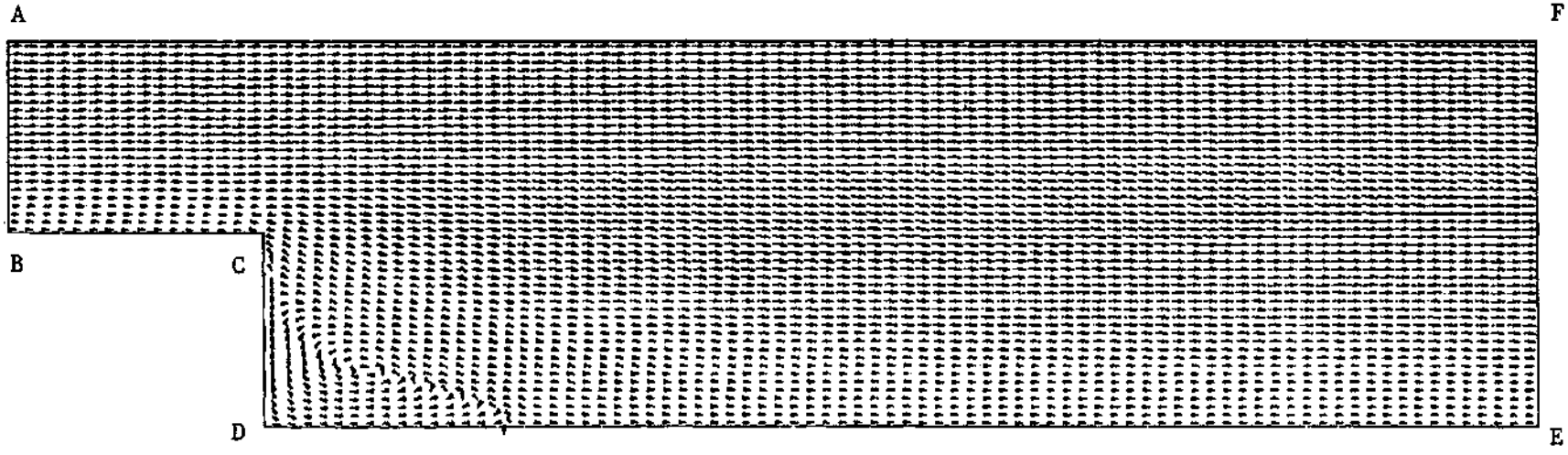

$\Delta x = 1/12$ $\Delta y = 1/24$ $M_1 = 3$

$Re = 550$ $\Delta t = 16\Delta t_{CFL}$

Figure E-1. Velocity Vectors - Fine Mesh.

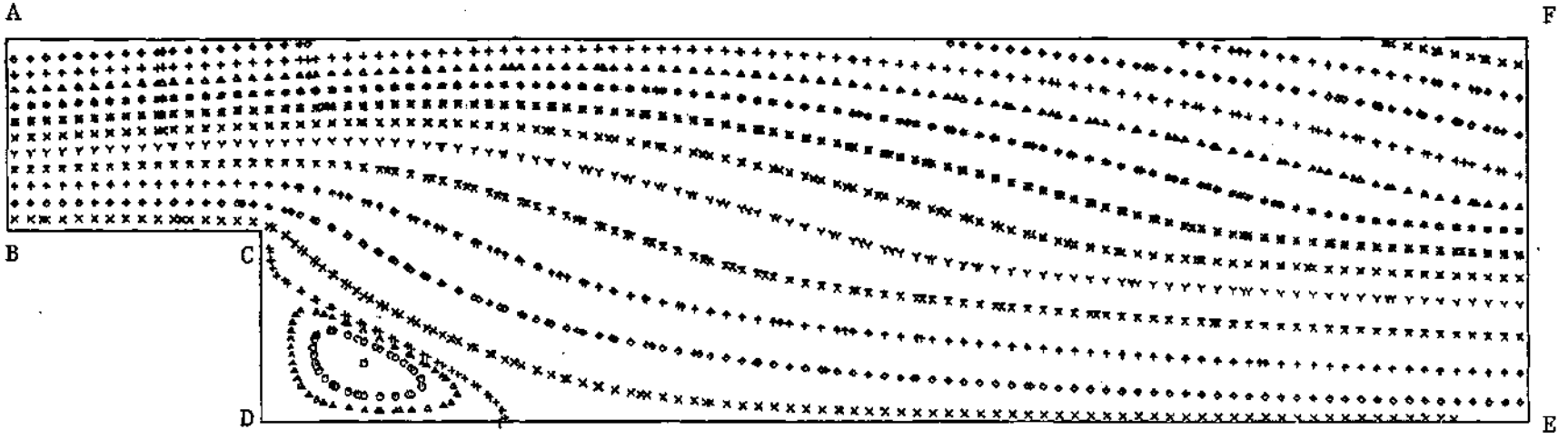

$\Delta x = 1/12$ $\Delta y = 1/24$ $M_1 = 3$

$Re = 550$ $\Delta t = 16\Delta t_{CFL}$

Figure E-2. Streamlines - Fine Mesh.

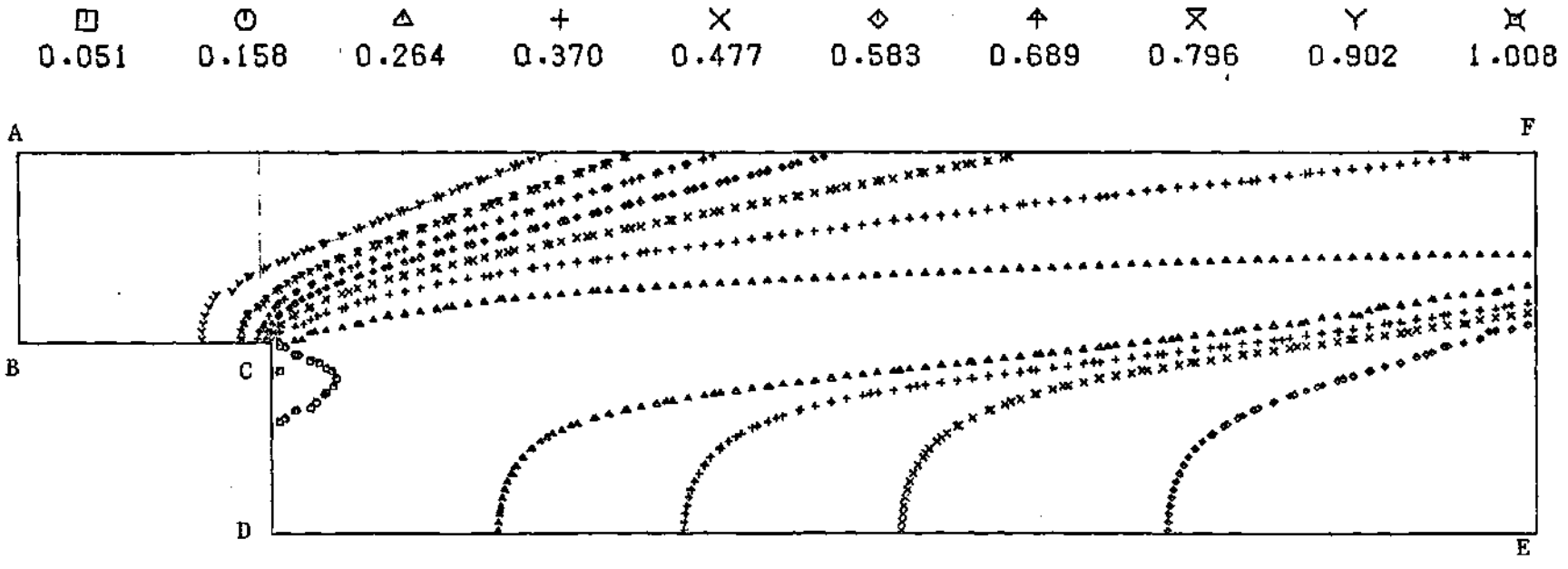

$\Delta x = 1/12$ $\Delta y = 1/24$ $M_1 = 3$

$Re = 550$ $\Delta t = 16\ \Delta t_{CFL}$

Figure E-3. Pressure Contours - Fine Mesh.

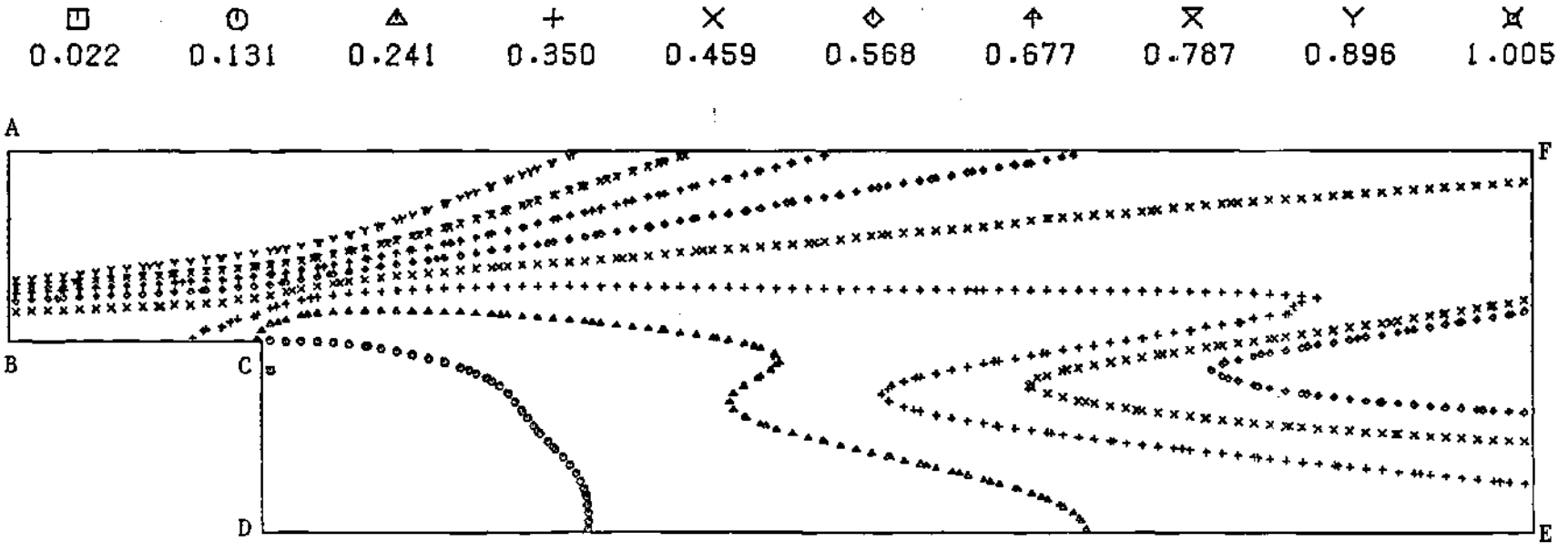

$\Delta x = 1/12$ $\Delta y = 1/24$ $M_1 = 3$

$Re = 550$ $\Delta t = 16\ \Delta t_{CFL}$

Figure E-4. Density Contours - Fine Mesh.

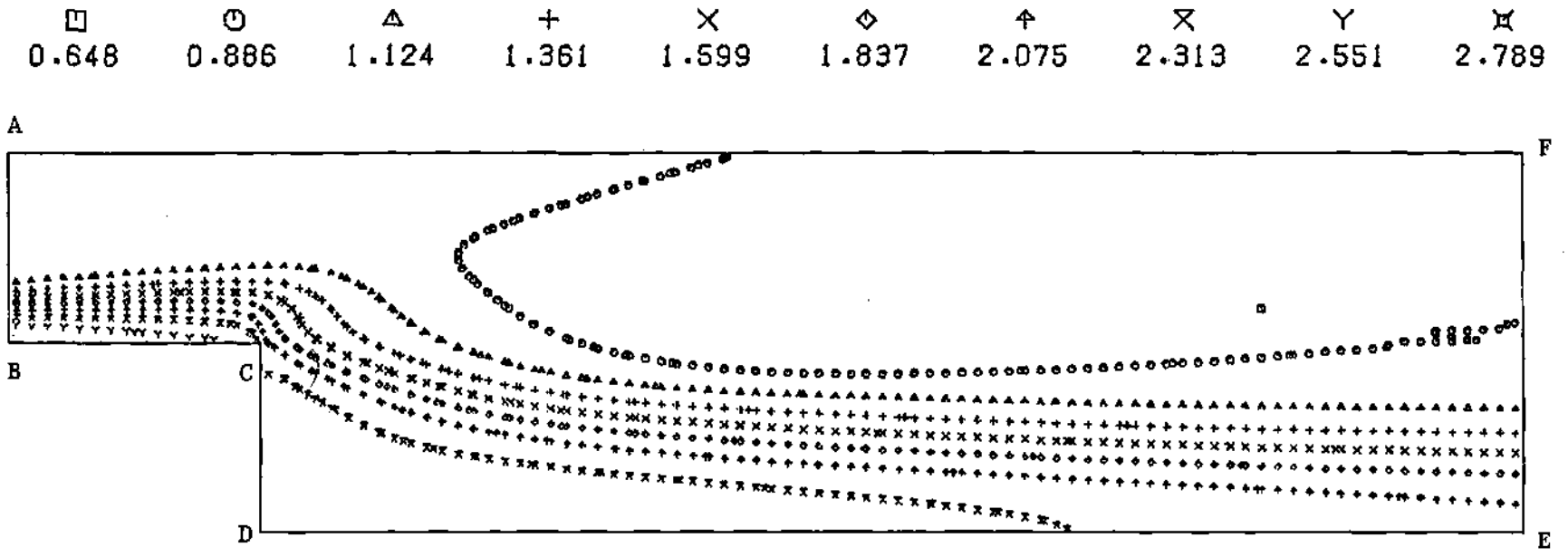

$\Delta x = 1/12$ $\Delta y = 1/24$ $M_1 = 3$

$Re = 550$ $\Delta t = 16\ \Delta t_{CFL}$

Figure E-5. Internal Energy Contours - Fine Mesh.

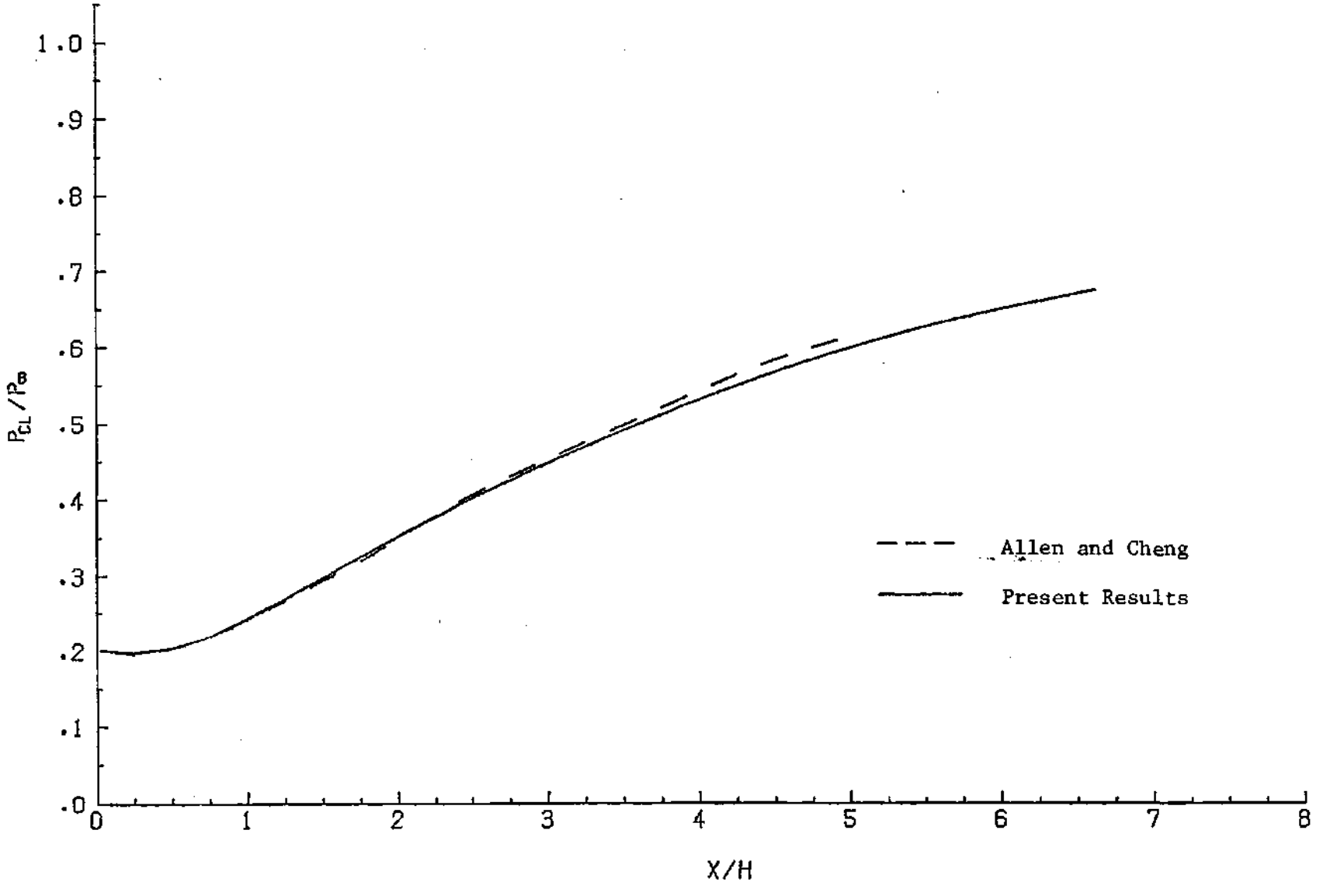

Figure E-6. Centerline Pressure - Fine Mesh.

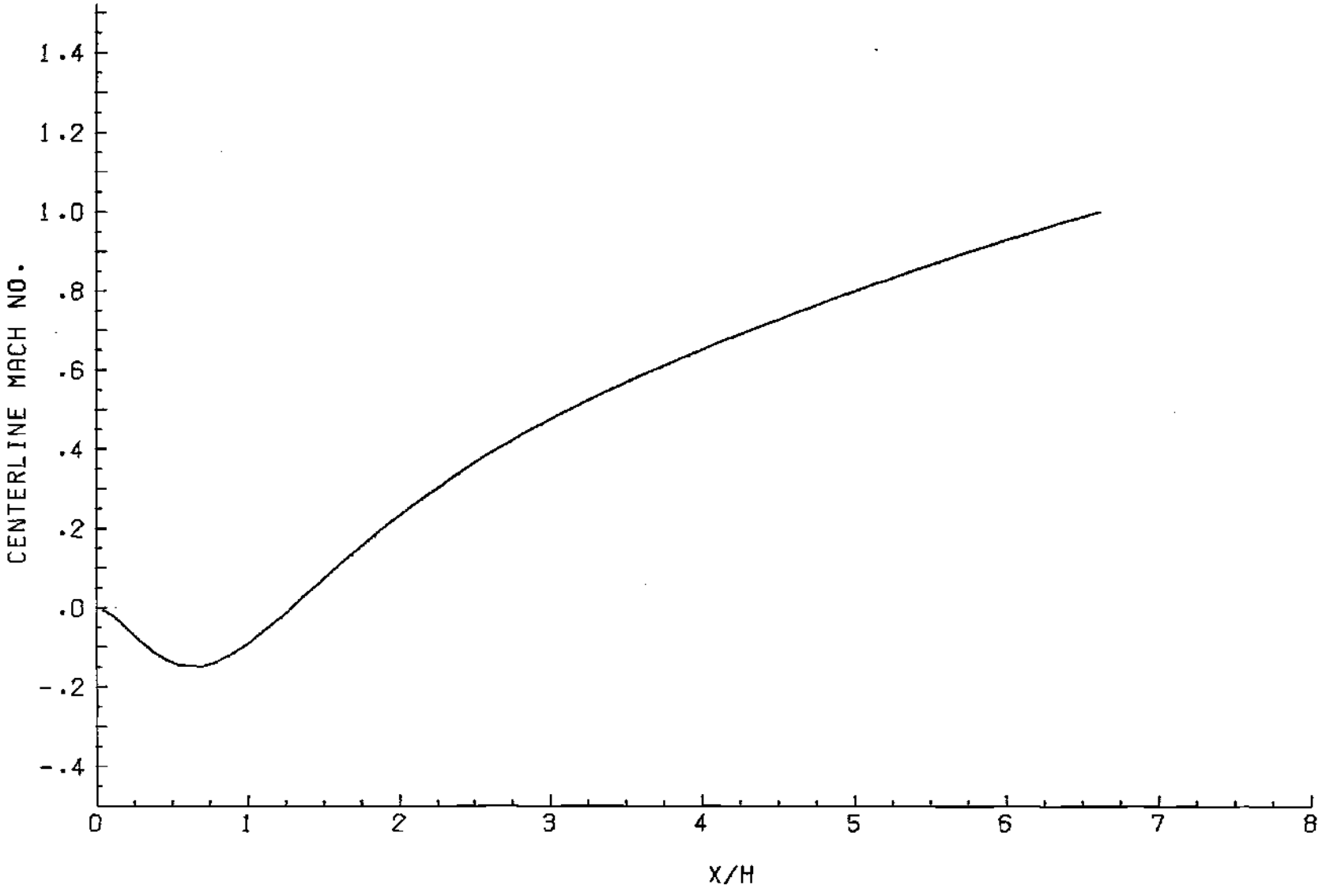

Figure E-7. Centerline Mach Number - Fine Mesh

REFERENCES

1. Gregory, T. J., L. J. Williams, and D. E. Wilcox, "Airbreathing Launch Vehicle for Earth Orbit Shuttle - Performance and Operation," Journal of Aircraft, Vol. 8, No. 9, Sept. 1971, pp. 724-731.

2. Henry, John R. and Griffin Y. Anderson, "Design Considerations for the Airframe-Integrated Scramjet," Paper presented at the 1st International Symposium on Air Breathing Engines, Marseille, France, June 19-23, 1972.

3. Becker, J. V., "New Approaches to Hypersonic Aircraft," Seventh Congress of International Council of the Aeronautical Sciences, Rome, Italy, Sept. 1970.

4. Becker, J. V., "Prospects for Actively Cooled Hypersonic Transports," Astronautics and Aeronautics, Vol. 9, No. 8, Aug. 1971, 1404-1408.

5. Matsumoto, I. R., K. Kimoto, and N. Tsuchinoto, "A Study of Double Concentric Jets," JSME Bulletin, Vol. 16, March 1973, pp. 529-540.

6. Lewis, J. E. and R. L. Chapkins, "Mean Properties of the Turbulent Near Wake of a Slender Body with and without Base Injection," AIAA Journal, Vol. 7, May 1969, pp. 835-841.

7. Lewis, J. E., W. Behrens, and C. J. Collins, "Experimental Investigation of the Effects of Base Mass Addition on the Near Wake of a Slender Body," AIAA Journal, Vol. 9, August 1971, pp. 1506-1513.

8. Valentine, D. T. and C. E. G. Przirembel, "Turbulent Axisymmetric Near Wake at Mach 4 with Base Injection," AIAA Journal, Vol. 8, December 1970, pp. 2279-2280.

9. Tennekes, H. and J. L. Lumley, A First Course in Turbulence, MIT Press, Cambridge, Massachusetts, 1972.

10. Peters, C. E., W. J. Phares, and T. H. M. Cunningham, "Theoretical and Experimental Studies of Ducted Mixing and Burning of Coaxial Streams," AIAA Paper 69-85, New York, 1969.

11. Channapragada, R. S. and J. P. Woolley, "Turbulent Mixing of Parallel Compressible Non-Isoenergetic Streams," Astronautica Acta, Vol. 13, No. 4, 1967, pp. 341-352.

12. Vasiliu, J., "Turbulent Mixing of a Rocket Exhaust with a Supersonic Stream, Including Chemical Reaction," Journal of the Aerospace Sciences, Vol. 29, No. 1, January 1962, pp. 19-28.

13. Cohen, L. S., "An Analytical Study of the Mixing and Nonequilibrium Chemical Reaction of Coflowing Compressible Streams," AIAA Paper 66-617, Colorado Springs, Colorado, 1966.

14. Edelman, R. and O. Fortune, "An Analysis of Mixing and Combustion in Ducted Flows," AIAA Paper 68-114, New York, 1968.

15. Patankar, S. V. and D. B. Spalding, Heat and Mass Transfer in Boundary Layers, International Textbook Co., London, 1970.

16. Launder, B. E. and D. B. Spalding, "Turbulence Models and Their Application to the Prediction of Internal Flows," Heat and Fluid Flow, Vol. 2, No. 1, 1972, pp. 43-54.

17. Launder, B. E. and D. B. Spalding, "The Numerical Computation of Turbulent Flows," Computer Methods in Applied Mechanics and Engineering, Vol. 3, 1974, pp. 269-289.

18. Launder, B. E., A. Morse, W. Rodi, and D. B. Spalding, "Prediction of Free Shear Flows - A Comparison of the Performance of Six Turbulence Models," in Free Turbulent Shear Flows, Vol. 1, NASA SP-321, 1973, pp. 361-426.

19. Krause, E., "Application of Numerical Techniques in Fluid Mechanics," Aeronautical Journal, August 1974, pp. 337-354.

20. Bangert, L. H. and R. L. Roach, "Study of Effects of Injector Geometry on Fuel-Air Mixing and Combustion," Final Report, NASA Grant NGR-11-002-177, Georgia Institute of Technology, August 1977.

21. Mueller, Thomas J., "Determination of the Turbulent Base Pressure in Supersonic Axisymmetric Flow," Journal of Spacecraft, Vol. 5, No. 1, January 1968, pp. 101-107.

22. Alber, I. E. and L. Lees, "Integral Theory for Supersonic Turbulent Base Flows," AIAA Journal, Vol. 6, July 1968, pp. 1343-1351.

23. Mehta, Gopal K., A Theory of the Supersonic Turbulent Axisymmetric Near Wake Behind a Bluff Body, Ph.D. Thesis, Georgia Institute of Technology, May 1977.

24. Allen, J. S. and S. I. Cheng, "Numerical Solutions of the Compressible Navier-Stokes Equations for the Laminar Near Wake," Physics of Fluids, Vol. 13, January, 1972, pp. 37-52.

25. Roache, Patrick J. and Thomas J. Mueller, "Numerical Solutions of Laminar Separated Flows," AIAA Journal, Vol. 8, No. 3, March 1968, pp. 530-538.

26. Briley, W. R., H. McDonald, and H. J. Gibeling, "Solution of the Multidimensional Compressible Navier-Stokes Equations by a Generalized Implicit Method," United Technologies Research Center, East Hartford, Connecticut, Report R75-911363-15, January, 1976.

27. Douglas, J. and J. E. Gunn, "A General Formulation of Alternating Direction Methods," Numerische Math., Vol. 6, 1964, p. 428.

28. Isaacson, E. and H. B. Keller, Analysis of Numerical Methods, John Wiley and Sons, Inc., New York, New York, 1966, pp. 58-61.

29. Kronzon, Y., J. Rom, and A. Seginer, "Laminar Supersonic Flow over a Backstep - A Numerical Solution at Higher Reynolds Numbers," Proceedings of the 1976 Heat Transfer and Fluid Mechanics Institute, Stanford University Press, 1976, pp. 390-403.

30. Roache, P. J., Computational Fluid Dynamics, Hermosa Publishers, Alburquerque, New Mexico, 1972.

31. Yanenko, N. N., The Method of Fractional Steps, Translation edited by M. Holt, Springer-Verlog, New York, 1971.

32. Moretti, G., "A Pragmatical Analysis of Discretization Procedures for Initial- and Boundary-Value Problems in Gas Dynamics and Their Influence on Accuracy or Look Ma, No Wiggles!" Polytechnic Institute of New York, POLY-AE/AM Report No. 74-15, September 1974.

33. Kothari, A. P. and J. D. Anderson, Jr., "Navier Stokes Solutions for Chemical Laser Flows: Cold Flows," AIAA Journal, Vol. 14, No. 5, May 1976, pp. 702-703.

34. Allen, J. S. "Numerical Solutions of the Compressible Navier-Stokes Equations for the Laminar Near Wake in Supersonic Flow," Ph.D. Thesis, Princeton University, 1968.

35. Hama, Francis R., "Experimental Studies on the Lip Shock," AIAA Journal, Vol. 6, No. 2, February 1968, pp. 212-219.

36. Donaldson, I. S., "On the Separation of a Supersonic Flow at a Sharp Corner," AIAA Journal, Vol. 5, No. 6, June 1967, pp. 1086-1088.

VITA

Robert Landon Roach was born August 5, 1950 in West Palm Beach, Florida. He graduated from John I. Leonard High School, Lake Worth, Florida in 1968. He enrolled in Georgia Institute of Technology in the Fall of 1968 and graduated with High Honor in the School of Aerospace Engineering in 1973. He had studied under the Cooperative Education Plan and was employed at the Florida Research and Development Center of Pratt & Whitney Aircraft in West Palm Beach. His greatest honor came in June, 1971 when he married the former Gloria Ann Wirth of West Palm Beach. He received his Master of Science in Aerospace Engineering at Georgia Tech in 1974 and was commissioned as a 2nd lieutenant in the United States Air Force in January 1975.